A Study of Protostars with Spectral Modeling Based on the Two-Dimensional Radiative Transfer Calculations

Takeshi NAKAZATO

A dissertation submitted to the Doctoral Program
in Physics, the University of Tsukuba
in partial fulfillment of the requirements
for the degree of Doctor of Philosophy in Physics

January 2003

ABSTRACT

We constructed two-dimensional radiative equilibrium protostar model to infer the structure of the Class I objects, which are considered as protostellar candidate. In the present model, we assumed that the protostar consists of three components; a central star, a circumstellar disk, and an envelope. We computed the temperature distribution of the circumstellar material under the condition of the radiative equilibrium. We simulated Spectral Energy Distribution (SED) of Class I object. We first showed that the detailed treatment of radiation transfer is essential to the protostar. We next revealed the relation between the emergent SEDs and the physical structure of the protostar. Based on these results, we established the standard procedure to infer the physical property of the protostar from the emergent SED. Furthermore, we proposed two new indicators, $(\nu L_\nu)_{\rm max}$, which is the peak flux of the SED, and $f_{\rm L}$, which is the ratio of emergent luminosity $L_{\rm SED}$ to the peak flux. The former is useful to estimate the luminosity of the central star, and the latter is effective as an indicator of inclination angle of the system. Finally, we applied the procedure to two protostellar candidates, IRAS 04365+2535 (TMC1A), belonging to Class I, and VLA1623, a prototype of Class 0. We showed that these objects surely belong to the observed Classes. We also discussed the evolutionary state of these objects based on the spectral modeling of their SEDs. As a result, TMC1A is in the intermediate phase of the Class I stage of the final mass $\sim 0.3 M_\odot$, while VLA1623 is in the earlier phase of the Class 0 stage of the final stellar mass $\sim 0.5 M_\odot$.

Contents

Chapter 1

Introduction

1.1 Formation of Low Mass Pre-Main-Sequence Stars

Formation of a star, like the Sun, is worth investigating because its understanding leads to the appreciation of the origin of the solar system, Earth, and finally, the human being. The star is formed by the consequence of the collapse of a parent molecular cloud core due to its own gravity. Theoretically, protostellar evolution has been investigated by the hydrodynamical simulation of this collapse. Larson (1969) performed a spherically symmetric collapse simulation for an initially homogeneous gas cloud having the mass of $1M_{\odot}$. According to his calculation, the collapse can be separated into two collapse phases, namely, 'first collapse' and 'second collapse'. The cloud is initially optically thin to the thermal emission from dust particles and compressional heating is not efficient. Thus, cloud is isothermal and collapses freely since there is no pressure gradient which competes against the gravity. In this phase, evolution of density profile in the cloud is self-similarly, since the free-fall timescale, $t_{\mathrm{ff}} \propto \rho^{-1/2}$, becomes smaller as the radius becomes small, so that the inner region of the cloud collapses faster than the outer region of the cloud (Figure 1.1). As collapse proceeds, the cloud becomes optically thick and becomes adiabatic, no longer isothermal, because it cannot radiate away the energy arising due to the collapse. Thus, the pressure gradient becomes efficient to stop the infalling motion, and forms a hydrostatic core at the center. This core is called the 'first core' and the evolution at this phase is called the 'first collapse'.

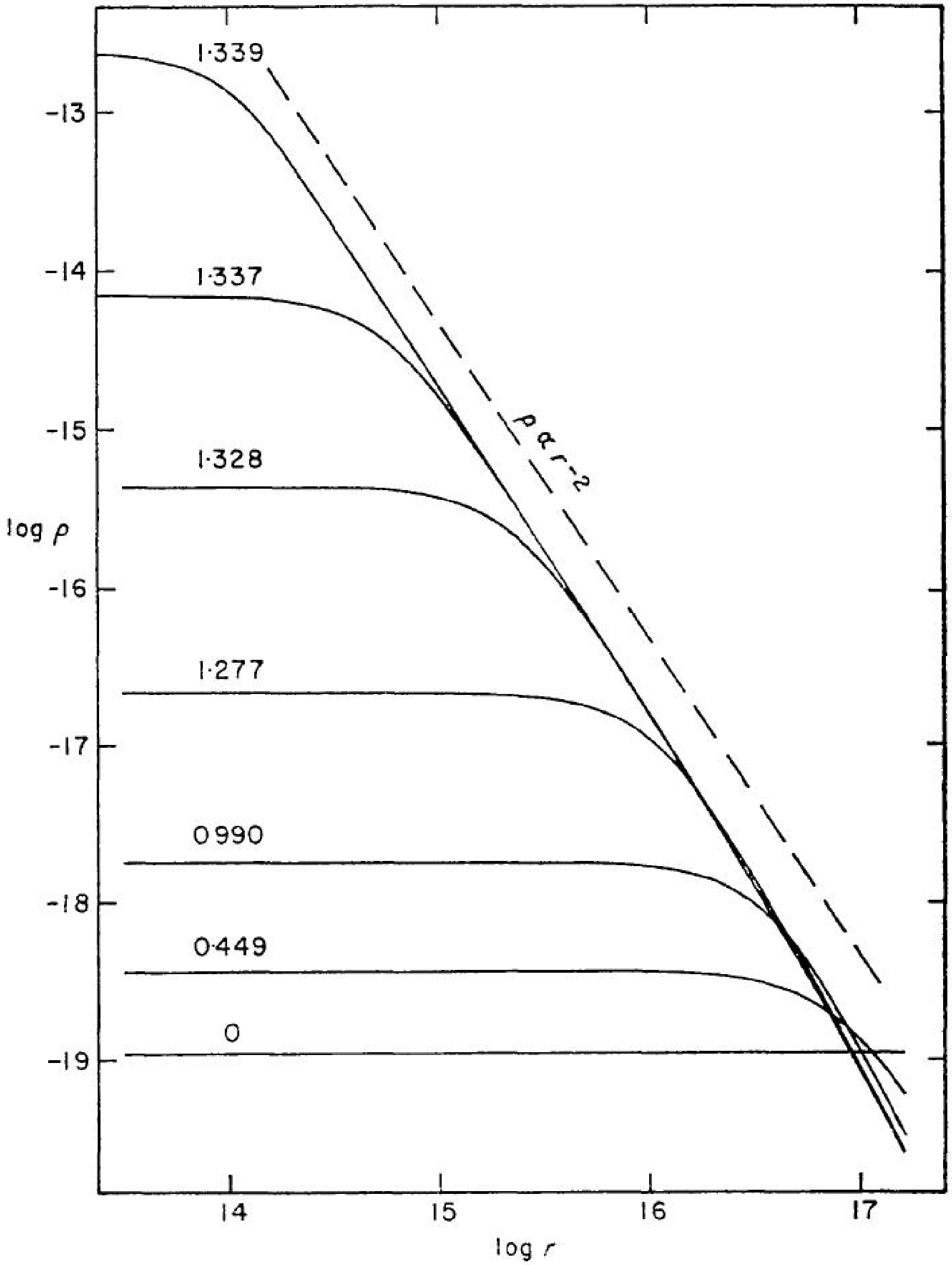

Figure 1.1: The evolution of the density profile in the collapsing cloud. The outer envelope approaches the r^{-2} profile, while the central region is flat. The number associated with each curve shows the time measured from the initial state ('0' represents the initial density profile). After Larson (1969). Units are in cgs.

As the core increases mass and decreases its radius, infalling velocity exceeds the sound speed and a shock is formed at the surface of the first core. The infalling materials are stopped at this shock and kinematic energy of these materials are thermalized here, and eventually, radiated away from the surface of the first core. The hydrogen is in molecular form in the first collapse phase, but when the temperature of the first core exceeds 2000K, molecular hydrogen is dissociated, and the first core begins to collapse again. This is because the energy released by the collapse is not efficiently converted to the thermal energy, i.e. the gas cannot produce enough pressure gradient to support the first core, since the dissociation of the molecular hydrogen consumes the energy. This collapse is called the 'second collapse'. When molecular hydrogen is almost dissociated, the gas becomes adiabatic again, and forms a hydrostatic core in the first core. This is the 'second core', which is a seed of the star (Figure 1.2).

Shu (1977) simulated the collapse of the singular isothermal sphere. He suggested that the density profile in the infalling envelope approaches to $\rho \propto r^{-1.5}$ rather than the profile $\rho \propto r^{-2}$ obtained by Larson (1969). This difference arises from the initial condition. Shu (1977) adopted the configuration nearly hydrostatic equilibrium as the initial condition, while Larson (1969) adopted the homogeneous cloud. Shu (1977) assumed an isothermal cloud although it is not realistic in the later phase of the collapse. On the contrary, Larson (1969) assumed that the temperature is almost isothermal as long as the cloud is optically thin, and adopted diffusion approximation for the calculation of energy transfer via the radiation when the cloud becomes optically thick. But this approximation is valid only in deep inside the core where the cloud is optically thick. The energy transport by radiation is very important since the temperature of the material is determined by the balance between the radiative cooling and the compressional heating, and the temperature of the material is very important for the evolution of the collapse (e.g. second collapse). Masunaga, Miyama, & Inutsuka (1998) simulated the first collapse for spherically symmetric cloud by carefully treating the radiative transfer using so-called Variable Eddington Factor (VEF) method, which accurately solves the radiation transfer. They also simulated the second collapse in a similar way (Masunaga & Inutsuka 2000a).

The above simulations assumed spherically symmetric geometry. But, in general,

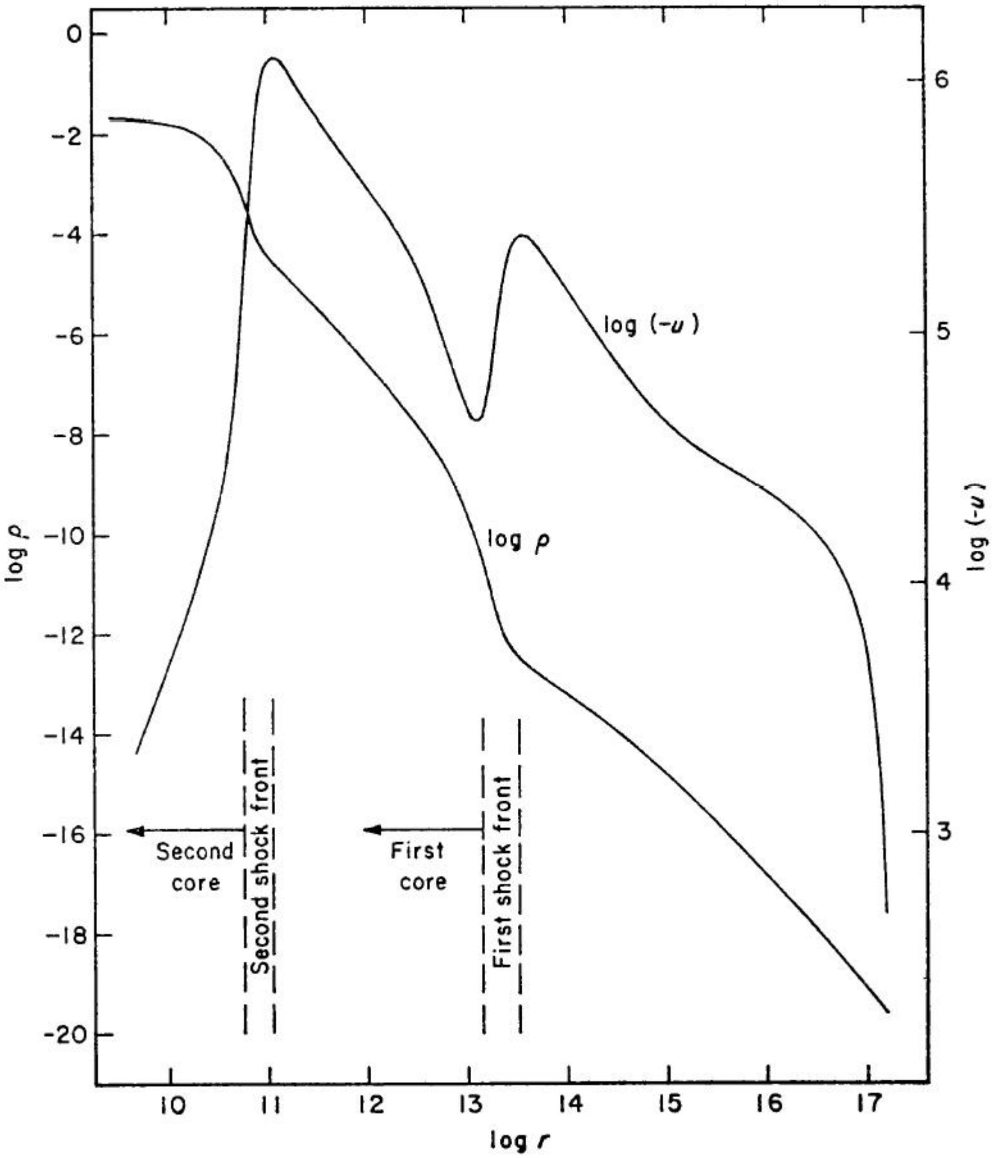

Figure 1.2: The formation of the second core. Two solid curves represent the density and the velocity profile, respectively. Two shocks at the surface of the first and the second cores emerge. The shock at the first core eventually disappears as the density becomes small. After Larson (1969). Units are in cgs.

infalling material has some amount of angular momentum, so the collapse process is not likely to be spherically symmetric. Terebey, Shu, & Cassen (1984) obtained an axisymmetric infalling envelope configuration by adding the slow rotation to the Shu's singular isothermal collapse model. The infalling materials cannot accrete directly to the central core because of its own angular momentum, so these materials form a circumstellar disk around the central core. Saigo, Matsumoto, & Hanawa (2000) performed the formation of the disk by the two-dimensional hydrodynamical simulation for the polytropic gas, which assumes the pressure to be proportional to the power of the density, $P = K\rho^{\gamma}$. The materials in the disk accrete slowly as decreasing their angular momentum due to the viscous angular momentum transfer (e.g. Lynden-Bell & Pringle 1974) and finally accrete to the central core. The angular momentum, remained by the accretion, is casted away through the bipolar outflow, which is formed by the magnetodynamical interaction in the disk (e.g. Kudoh, Matsumoto, & Shibata 1998).

Observationally, it is indicated that multiple stars are formed from a parent cloud core. To simulate this situation, three-dimensional calculation is needed. Boss & Myhill (1992) and their following series constructed a three-dimensional hydrodynamical code, and simulated the fragmentation of the cloud and the formation of multiple stars. Matsumoto & Hanawa (1999) also performed the three-dimensional hydrodynamical simulation, and investigated the formation of bar and disk structure, which leads to a binary system. These simulations assumed the polytropic relation or the approximated treatment for radiative transfer process. But accurate treatment of the radiative transfer becomes more important for such high resolution calculations since these simulations aim to reveal the detailed structure of the core and the disk, and this leads to the mixed situation of the optically thick and thin regions. Two- or three-dimensional hydrodynamical simulation with carefully treated radiative transfer process has not been constructed so far.

1.2 Observation of Low Mass Young Stellar Objects

There are many active star-forming regions in our Galaxy, such as the Taurus, the ρOphiuchus, etc. These are the best places to study the Young Stellar Objects (YSOs), which are in transition phase from the molecular cloud core to the stars, since, in these regions, there are many YSOs in various evolutionary phases, and we can obtain the knowledge of the star formation by investigating not only the individual objects but also the statistical properties of these objects. Main-Sequence stars are observed at the optical wavelength, and many YSOs can also be observed at optical, because the central star becomes visible by the dissipation of the envelope. On the contrary, relatively younger YSOs are observed mainly as infrared sources, since the Pre-Main-Sequence (PMS) stars are still surrounded by the circumstellar matter which will accrete into the central object and includes dust grains heated to the temperature $10-100$K by the radiation of the central object (the blackbody radiation of this temperature peaks at the mid- to far-infrared wavelength). Thus, young protostellar candidates were discovered by the *Infrared Astronomical Satellite* (IRAS) which found the numerous infrared point sources in the nearby molecular clouds (e.g. Beichman et al. 1986; Kenyon et al. 1990). These YSOs are observed by the sub-millimeter and radio continuum emission (Pravdo et al. 1985; Zavagno et al. 1997). They are often associated with the molecular outflow, observed by the emission lines of CO and H_2, etc (e.g. Eiroa et al. 1994; Hoddapp & Ladd 1995; Bontemps et al. 1996b; Sandell et al. 1999; see also Figure 1.3). Driving source of the outflow is considered to be the central region of the YSO (e.g. Tomisaka 1998). On the other hand, there are some outflows, which do not have identified driving object in the infrared sources. These outflows are considered to associate with the YSOs heavily embedded in their envelope, which are not detected even at the infrared. Indeed, a survey around the outflows using the sub-millimeter and radio continuum emission discovered new protostellar candidates (e.g. Snell & Bally 1986; Bachiller, André, & Cabrit 1991a; Anglada et al. 1992; Gómez et al. 1994; Chini et al. 1997a; André, Motte & Bacmann 1999). Molecular line studies are also important since the observation provides the density and velocity structure of the circumstellar matter (e.g. Walker et al. 1986; Walker et al. 1994; Ward-Thompson et al. 1996; Gregersen et al. 1997; Mardones et al. 1997; Ohashi et al. 1997; Terebey & Padgett 1997). To investigate the motion of the circumstellar matter, observation of maser spots, using the interferometer such as the Very Long Baseline Array (VLBA) provides the highest angular resolution, reaching $\sim$ AU (Astronomical Unit $= 1.5 \times 10^{13}$cm) resolution for nearby molecular cloud (Furuya et al. 1999; Imai, Iwata, & Miyoshi 1999; Furuya et al. 2000). Near-infrared imaging also provides the density structure of YSOs (Kenyon et al. 1993; Padgett et al. 1999). Furthermore, X-ray from the YSOs is also detected (Koyama et al. 1996; Tsuboi et al. 2001), and its intensity is rather strong for the youngest phase of YSOs, which has colder SEDs, than the later phase (Tsujimoto et al. 2002). As a result, YSOs are interesting observational targets for all wavelength ranges.

1.2.1 Observational Classification

The PMS stars are classified into four categories, named Class 0, I, II, and III, by the shape of their Spectral Energy Distributions (SEDs). Lada & Wilking (1984) divided the observed SEDs into three spectral types. Adams, Lada, & Shu (1987a) quantified that classification by the spectral index

$$n = \frac{d\log(\nu F_\nu)}{d\log\nu} = -\frac{d\log(\lambda F_\lambda)}{d\log\lambda}, \tag{1.1}$$

in the mid-infrared and near-infrared ranges (corresponding to the frequency range from $10^{13.5}$Hz to $10^{14.5}$Hz). A source with spectral index $n < 0$ is classified to a Class I object, a source with $0 < n < 1.5$ is classified to a Class II, and $n > 1.5$ is classified to a Class III. Further, André, Ward-Thompson, & Barsony (1993) introduced a new category, Class 0, with following definition,

$$\frac{L_{\rm bol}}{L_{1.3}} \leq 2 \times 10^4, \tag{1.2}$$

where $L_{\rm bol}$ is a bolometric luminosity of the object and $L_{1.3}$ is the luminosity at a wavelength 1.3mm. André et al. (1993) suggested that this definition corresponds to

$$\frac{L_{\rm submm}}{L_{\rm bol}} \geq 5 \times 10^{-3}, \tag{1.3}$$

where $L_{\rm submm}$ is the luminosity radiated by a source longward of 350μm. The sources classified into Class 0 are almost invisible in the mid- and near-infrared wavelength, so they are not categorized to any former three Classes. Typical shapes of SEDs of each Class are schematically shown in Figure 1.4. The SEDs categorized into Class II and the Class III have the peak at the optical to the near-infrared wavelengths, and these appear

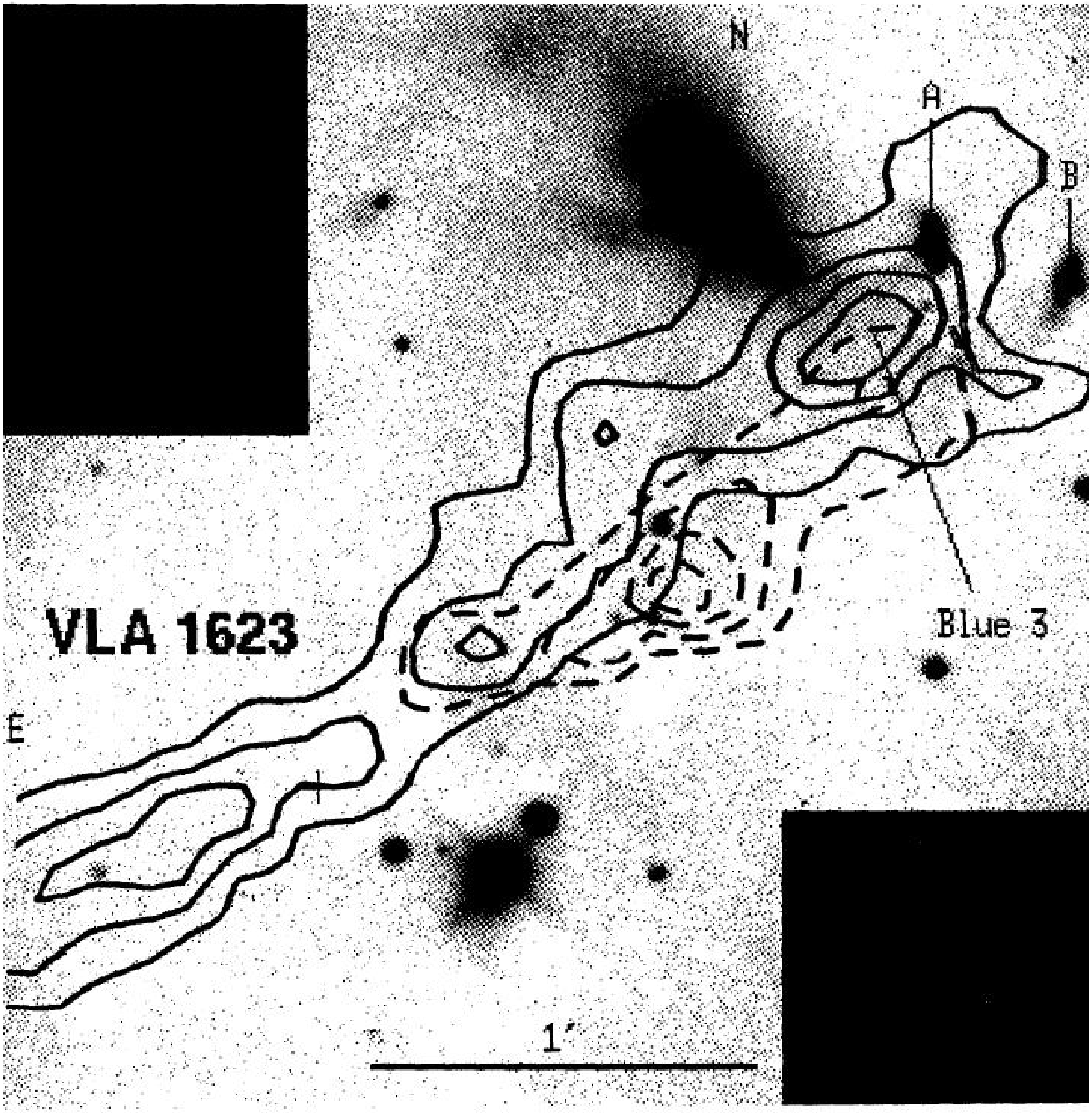

Figure 1.3: Molecular outflow associated with the Class 0 object VLA1623. Contours display CO line intensity map of the blueshifted lobe (solid curve) and the redshifted lobe (dashed curve). Grayscale shows the image of the H_2 line emission. (Davis & Eislöffel 1995)

to be a superposition of a stellar blackbody and excess emission in infrared wavelength. On the other hand, the SEDs of the Classes 0 and I have a peak from far-infrared to sub-millimeter wavelength range. These emissions appear to be originated from some cold emitters.

Evolutionary Sequence

These Classes are interpreted as an evolutionary sequence of the PMS star (Adams et al. 1987a). A Class I object is regarded as a protostar which consists of a star and a disk system, but it is still obscured by an optically thick infalling envelope. The emergent SED of this phase is constructed by a superposition of the emission from the dust grains heated to $10-100$K by the radiation from the central object (Adams & Shu 1986). This description is well consistent with the observed SEDs. The mapping observation around these objects, using sub-millimeter continuum emissions or molecular line emissions, shows the existence of an extended structure which seems to correspond to an envelope (e.g. Loren et al. 1983; Ladd et al. 1991a,b; Zinnecker et al. 1992; Chandler & Richer 2000; Hogerheijde & Sandell 2000; Motte & André 2001; Saito et al. 2001). A Class 0 object is also a protostar, but it seems to be heavily embedded compared with the Class I object, because its SED peaks at longer wavelength than the Class I. According to André et al. (1993), physical distinction of these two Classes is the ratio of the mass of the central object to the circumstellar mass $M_*/M_{\rm env}$. The Class 0 corresponds to the main accretion phase, so that the ratio is less than unity, while the Class I is in a phase after the main accretion, so the mass of the central object is almost constant and the mass ratio $M_*/M_{\rm env}$ is larger than unity. On the other hand, the Class 0 object has been suspected to be an apparent effect, and the physical structure of the object is the same as that of the Class I. Several theoretical works showed that Class 0 SED can be reproduced by the Class I object by viewing it from the edge-on direction (e.g., Men'shchikov & Henning 1997). Jayawardhana, Hartmann, & Calvet (2001) suggested that the Class 0 SED can be reproduced by a Class I object which is deeply embedded in a parent molecular cloud and whose radiation is extincted by a foreground diffuse cloud. But, there are several Class 0 sources having small inclination angle (Greaves et al. 1997; Wolf-Chase et al. 1998). Furthermore, Bontemps et al. (1996a) showed

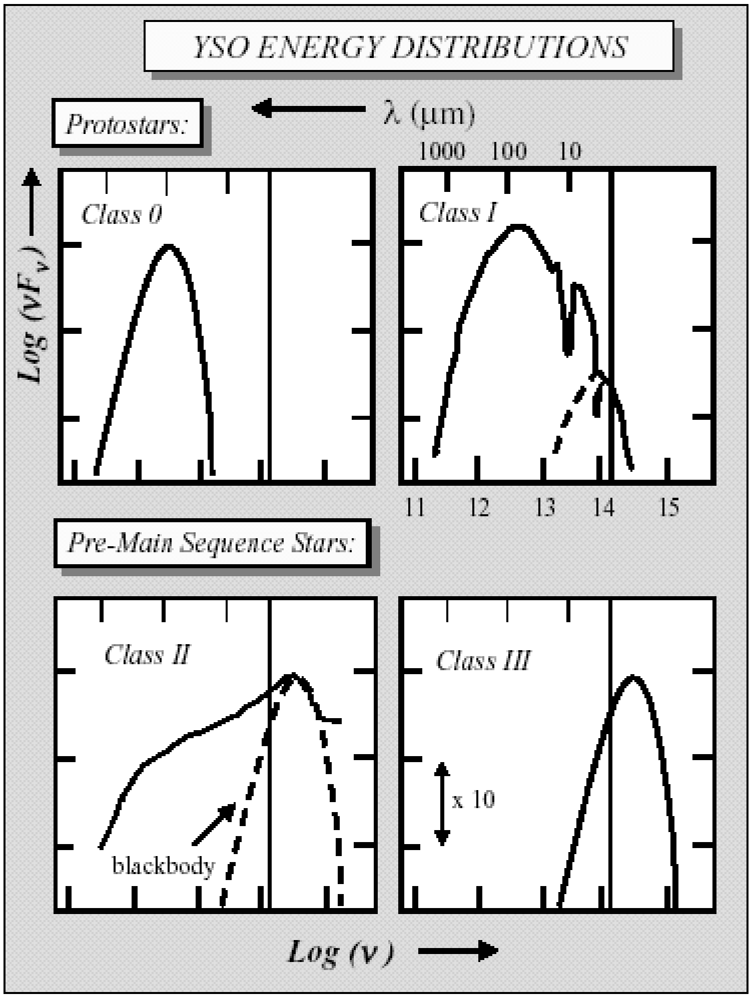

Figure 1.4: A schematic view of typical shapes of SEDs for each Class of the pre-main-sequence objects. Classes 0 and I are corresponding to a protostar phase, while Classes II and III are corresponding to a T Tauri star, which is more evolved object than the protostar. (Lada 1999)

that the outflow activity of Class 0 objects is systematically higher than that of Class I objects. Thus, the Class 0 category is established as the fourth category of the PMS phase, although the physical structure of Class 0 object is still unknown. Classes II and III objects correspond to T Tauri stars which consist of the central star and the circumstellar disk. This structure is interpreted as a following phase of the Class I objects that its envelope is already dissipated by accreting into the central region or blowing away due to the outflow. From the Hα emission line, Class II corresponds to 'classical' T Tauri star, and Class III corresponds to 'weak-lined' T Tauri star, which has weaker emission than the 'classical' T Tauri stars. Lynden-Bell & Pringle (1974) first showed that the excess emission from the T Tauri stars are originated from the circumstellar disk. The disk structure is also suggested by the imaging observation of T Tauri star at near-infrared wavelength. At this wavelength, the disk is optically thick so it is seen as a 'dark lane' in the image (Padgett et al. 1999). The Class II objects have a relatively massive disk, while Class III objects have a low mass disk or do not have a disk, since the excess of the infrared emission is smaller for Class III than Class II. This difference is also interpreted as an evolutionary sequence similar to the relation between the Class I and Class II. Namely, the Class III phase is the following phase of the Class II. The circumstellar disk in the Class III object has almost disappeared by the accretion to the central object or the formation of the planetary system. In the Class II objects, there are some peculiar objects whose SED is nearly flat in the infrared wavelength (Figure 1.5). These objects are called Flat-Spectrum T Tauri Stars (FTTSs). If the infrared excess emission of these objects originates from the circumstellar disk, temperature distribution of the disk should have the form $T(r) \propto r^{-1/2}$ (Adams, Lada, & Shu 1988). On the contrary, theoretical works predict $T(r) \propto r^{-3/4}$ in either case of the disk heated by the viscous heating (Lynden-Bell & Pringle 1974) or the geometrically flat disk heated by the radiation from the central star (Adams & Shu 1986). Thus, any mechanism that heats up the outer region of the disk is needed to reproduce the SED of the FTTSs. Kikuchi, Nakamoto, & Ogochi (2002) showed from the two-dimensional model carefully treating the detailed radiation transfer that the temperature distribution that produces the flat SED is realized by considering the scattering and reprocessing of the stellar radiation by the halo, which is the component of $\sim$ 100AU scale surrounding the star-disk system. According to them, FTTS is the transition object from the Class I to Class II phase.

Age Estimation

Evolution of a Pre-Main-Sequence star is discussed using the Hertzsprung-Russell (H-R) diagram (Figure 1.6), which is the plot of the effective temperature of the star $T_{\rm eff}$ against the bolometric luminosity of the star $L_{\rm bol}$. Evolutional track of a PMS star on the H-R diagram is predicted by theoretical simulations (Hayashi 1961; Palla & Stahler 1993). The age of an observed T Tauri star (Classes II and III) is estimated from the place on the H-R diagram using with the theoretical prediction. Ages of observed T Tauri stars $\tau_{\rm TTS}$ are almost $\sim 10^6$yr from the above estimation (Cohen & Kuhi 1979, Kenyon & Hartmann 1990). But, for protostar (Classes I and 0), the direct estimation of the age is very difficult because of the invisibility of their central star. However, we can estimate the age of these objects from a statistical argument. If we assume that the star is formed with a constant formation rate, the ratio of the number of objects in each evolutional phase should be equivalent to the ratio of the lifetime for each phase. In the Taurus-Auriga star forming region, the ratio of the number of T Tauri stars and the protostars is from $5:1$ to $10:1$, then the age of the protostars is estimated at $\tau_{\rm protostar} \sim 10^5$yr when we assume $\tau_{\rm TTS} \sim 10^6$yr (Kenyon et al. 1990). With the above assumption, we can also estimate the ages of the Class 0 objects from the ratio of the number of Class I and Class 0 objects, which is estimated to be $\sim 10^4$yr (André, Ward-Thompson, & Barsony 2000, and references therein). On the contrary, Visser, Richer, & Chandler (2002) estimated the age of Class 0 objects comparable to Class I objects ($\sim 10^5$yr) at the ρ Ophiuchus star forming region.

Evolution on the H-R Diagram

Although the central star is invisible, the effective temperature of Class 0 and I objects can be given by the temperature at the photosphere where the optical depth from the surface of the envelope is $\sim 2/3$. This photosphere is in the envelope at Class I or Class 0 phase and its temperature is different from the optically visible case. However, this definition agrees with the $T_{\rm eff}$ defined for the optically visible case, since the photosphere

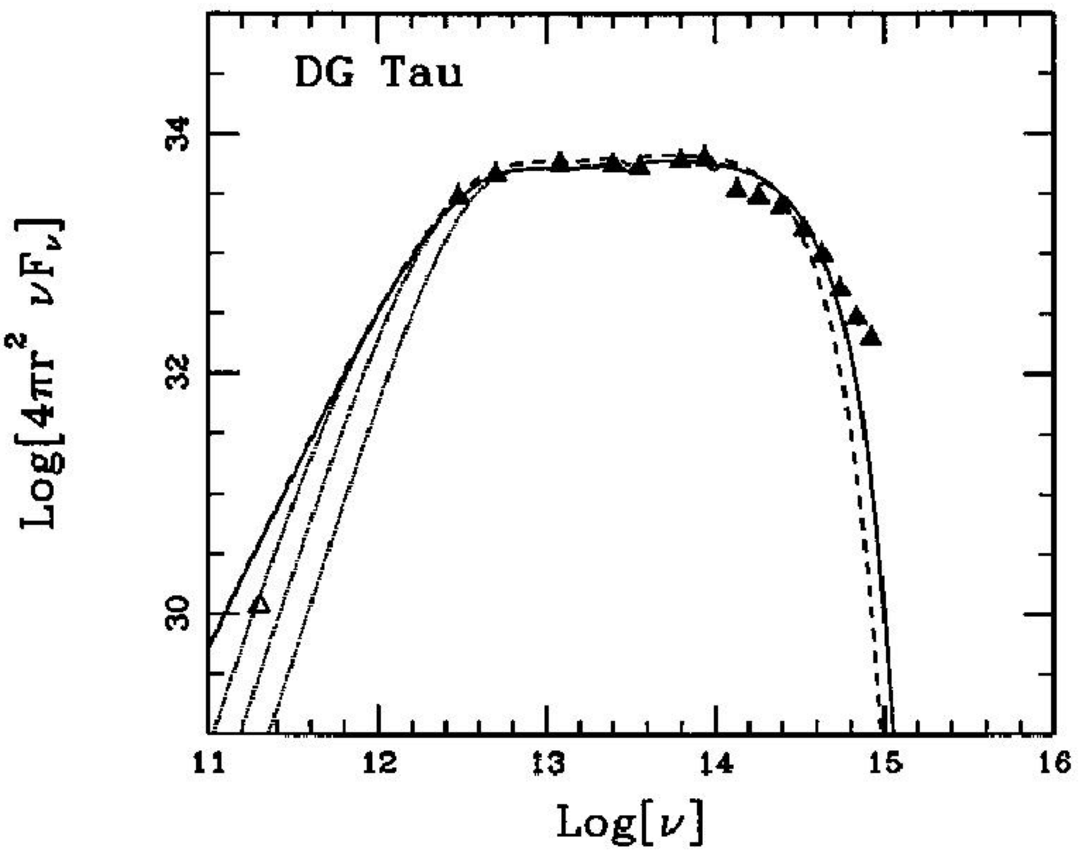

Figure 1.5: The observed SED for a flat-spectrum T Tauri star (FTTS) DG Tau. SED is almost flat from $10^{12.5}$Hz to $10^{14.5}$Hz. This implies the temperature distribution in the disk is inversely proportional to the square root of the distance from the center. (Adams, Lada, & Shu 1988)

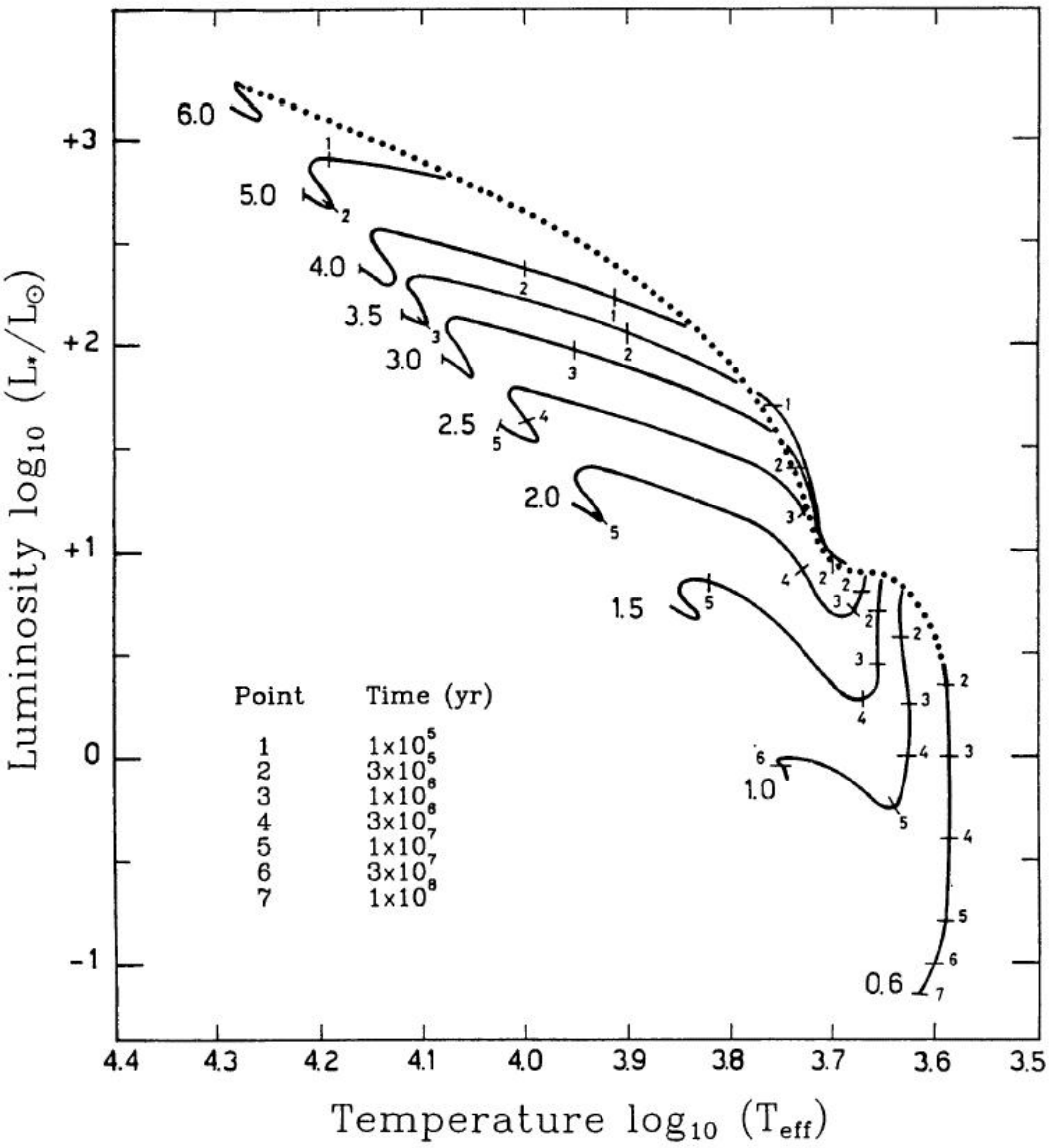

Figure 1.6: Evolutionary tracks on the Hertzsprung-Russell diagram for low and intermediate mass pre-main-sequence stars. Each curve shows the evolutionary track of star with different mass (the mass in the unit of solar mass is shown at the left edge of each curve). The dotted curve shows the birth line of the star which corresponds to the time when the central star becomes visible. (Palla & Stahler 1993)

moves to the surface of the central star when the envelope completely dissipates. We can follow the evolutionary track of the embedded sources (Classes 0 and I) using this temperature (Appenzeller & Tscharnuter 1975; Kippenhahn & Weigert 1990; Figure 1.7). Clearly, the evolutionary track is located on the right hand side of the main-sequence, since the effective temperature evolves from low to high. The luminosity of the pre-main-sequence star often exceeds the luminosity of the main-sequence star with the same mass. This is because the energy source of the luminosity is different between the pre-main-sequence and main-sequence phase. In Figure 1.7, evolutionary track is nearly vertical for initial ($0 \sim 10^4$yr) and final phases (10^5yr $\sim$), and nearly flat for intermediate phase ($10^4 \sim 10^5$yr). The initial phase is the main accretion phase, so the central mass is increasing with time and luminosity is also increasing. On the contrary, the temperature does not change significantly in this phase. Thus, the evolutionary track is nearly vertical. The intermediate phase corresponds to the dissipation phase of the envelope. The temperature of the photosphere is increasing with time since the photosphere moves inward according as the envelope dissipates. The luminosity is almost constant because the circumstellar matter has almost accreted onto the central star, so the central mass is almost constant. Thus, the evolutionary track is almost flat. The final phase roughly corresponds to the Figure 1.6. In this phase, main energy source of the luminosity is the gravitational energy released by the quasi-static contraction of the central star.

Observationally, it is useful to define the bolometric temperature instead of the effective temperature. The bolometric temperature $T_{\rm bol}$ is defined by the black body temperature having the same flux weighted mean frequency as the observed SED,

$$T_{\rm bol} \equiv \frac{\zeta(4)}{4\zeta(5)} \frac{h\bar{\nu}}{k} = 1.25 \times 10^{-11} \bar{\nu} \text{ K Hz}^{-1}, \tag{1.4}$$

where $\zeta(n)$ is Riemann zeta function of argument n, h is Planck constant, k is Boltzmann constant, and $\bar{\nu}$ is the flux weighted mean frequency for observed SED given by,

$$\bar{\nu} = \frac{\displaystyle\int_0^\infty \nu F_\nu d\nu}{\displaystyle\int_0^\infty F_\nu d\nu}, \tag{1.5}$$

(Myers & Ladd 1993; Chen et al. 1995; Myers et al. 1998). This definition also agrees with the effective temperature for optically visible case when both the envelope and

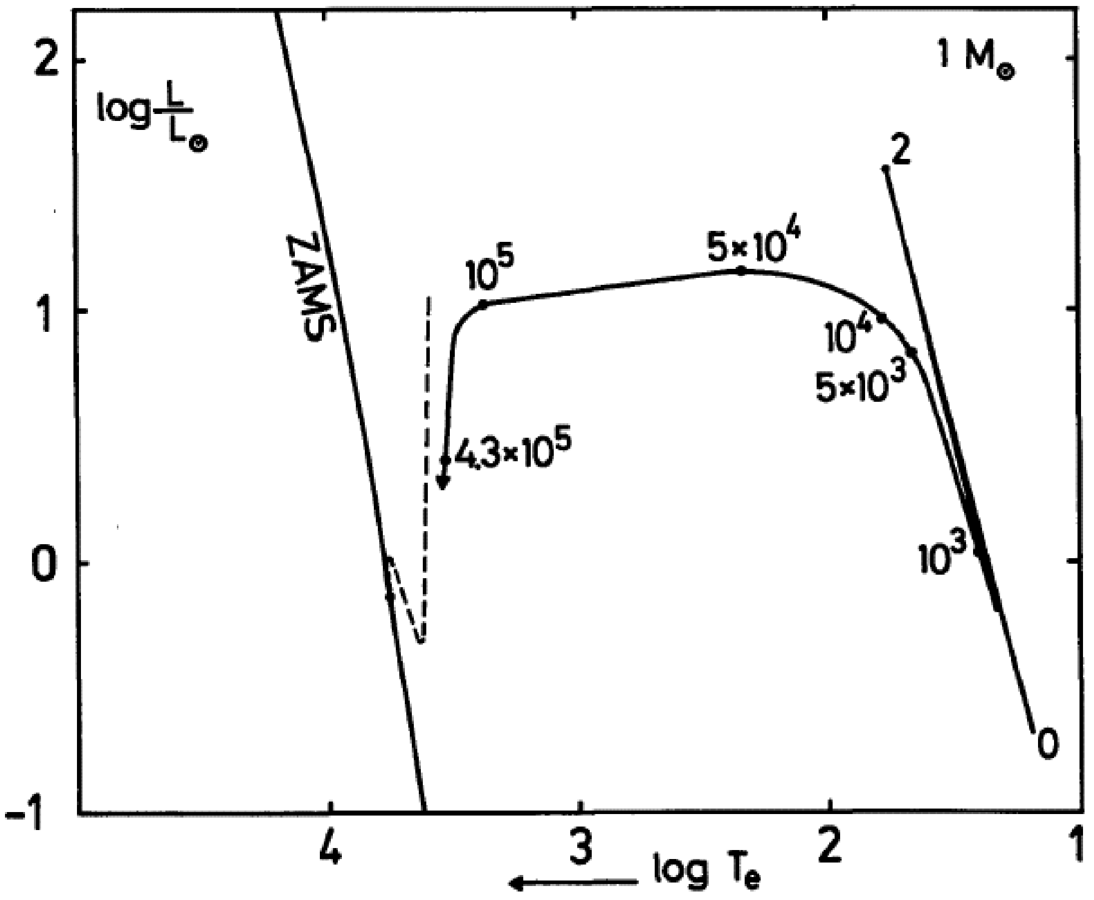

Figure 1.7: The evolutionary track of the protostar phase with the mass $1M_\odot$. The number associated with the curve is the age in units of year. The line marked 'ZAMS' represents the Zero-Age-Main-Sequence, which shows the position when nuclear burning begins, for each stellar mass. The dashed curve shows the evolutionary track for the pre-main-sequence star of $1M_\odot$. (Appenzeller & Tscharnuter 1975)

the disk disappear. The bolometric temperature $T_{\rm bol}$ clearly separates YSOs on the Bolometric Luminosity-Temperature (BLT) diagram from the Class 0 to the Class III phases (Chen et al. 1995; Figure 1.8). Note that since the bolometric temperature $T_{\rm bol}$ is equivalent to the effective temperature $T_{\rm eff}$ when the source radiates the single-temperature blackbody radiation, the position of a zero-age-main-sequence star becomes same both in the H-R diagram and the BLT diagram. In the BLT diagram, $T_{\rm bol}$ increases from protostars (60K to 500K) to classical T Tauri stars (1000K to 3000K) and finally to weak-line T Tauri stars (2000K to 5000K).

1.3 Modeling of Spectral Energy Distribution

Physical properties of YSOs inferred from the observation have an important effect to the theoretical study, since the observed property is a certain constraint for the theoretical results. Thus, the estimation of the physical property from the observational results should be carefully done.

The SED is one of the simplest and most useful observation for YSOs because SED is a spatially integrated observed flux distribution in the frequency space. So its observation does not need the high spatial resolution, that is demanded by the mapping observation. Also the SED does not need the frequency resolution like a spectroscopy. For these simple observations, however, especially for SED, the detailed model is needed to infer the physical property of the target objects, since SED loses the spatial information by integrating the observed flux. For observation of SED, spectral modeling is useful to infer the properties of the source: when the SED is observed, we first assume the model for the source and try to fit the observed feature of the SED by changing the physical parameters of the model, and finally, we can infer the physical property of the source from the model that reproduces the observed SED best. In this spectral modeling, an accuracy of the model is important, especially the determination of the temperature distribution is the most essential factor of the model because the SED consists of a superposition of the blackbody radiation from materials with various temperatures. In the low-mass star case, temperature distribution in the circumstellar matter is mainly determined by the balance between the heating by the radiation from the central star

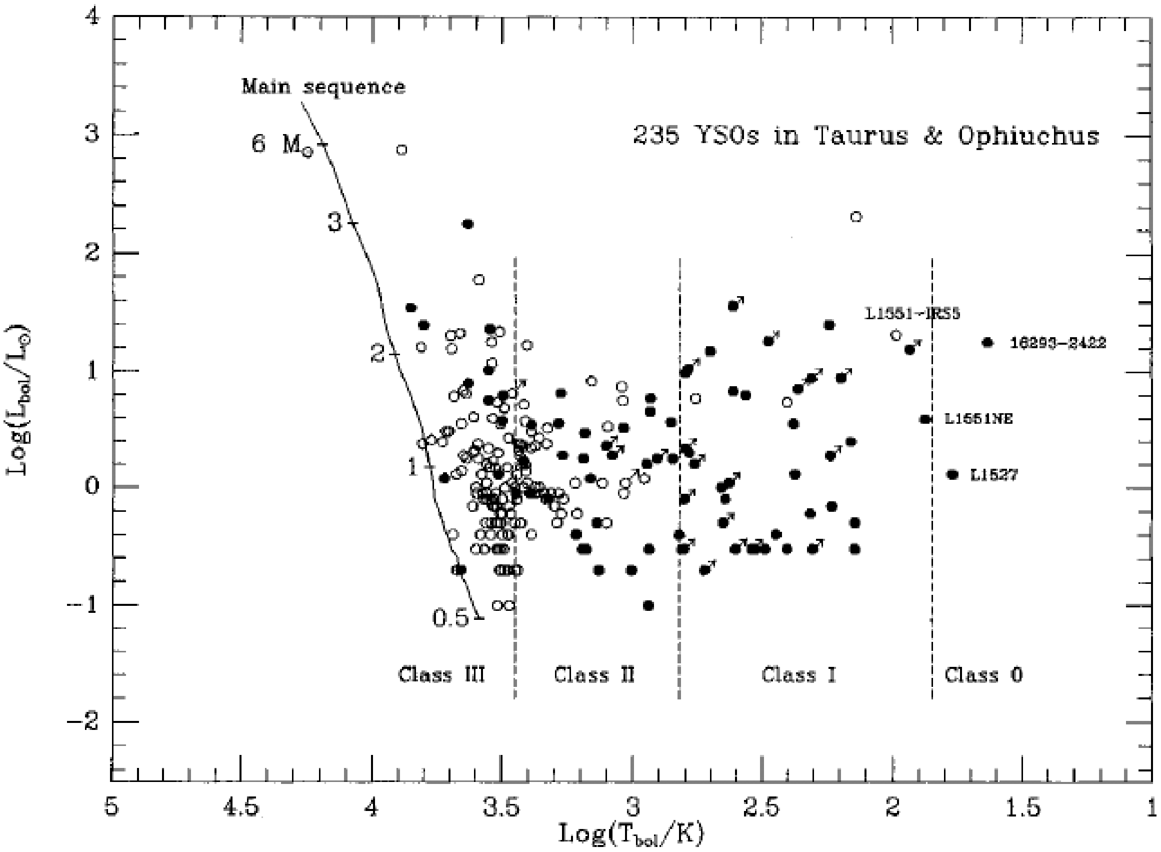

Figure 1.8: The Bolometric Luminosity-Temperature (BLT) diagram for the pre-main-sequence stars. Solid line shows the zero-age-main-sequence for $0.4 - 6M_\odot$. Vertical dashed lines are the boundaries of each Class. Circles represent the observed objects with a known spectral type (open circle) and without a known spectral type (filled circle). (Chen et al. 1995)

and the cooling by the thermal radiation from the matter itself. Thus, a radiative equilibrium calculation becomes essential to construct the detailed model for spectral modeling. On the other hand, spectral modeling is done using the very rough model observationally, such as the model assuming the isothermal, or the model which even regards the temperature distribution as the parameter of the model. These models have a possibility to misread the structure of the object.

For Class II and Class III sources, the detailed model is constructed since SEDs of these objects clearly consist of the blackbody radiation with various temperature. Thus, various two-dimensional models of star-disk system have been proposed (e.g. Chiang & Goldreich 1997; D'Alessio et al. 1998; Chiang & Goldreich 1999). On the other hand, detailed model for the Class I objects is quite few, especially the model for Class 0 objects does not exist because their SED is well fitted by the single-temperature blackbody. Under these situations, the careful treatment of the radiation field is still important. Kenyon, Calvet, & Hartmann (1993) performed the spectral modeling for many Class I objects with a two-dimensional radiative transfer model. But their treatment of the radiative transfer is essentially one-dimensional, so the resultant temperature distribution is not consistent with the radiation field of the central star. Men'shchikov & Henning (1997) constructed a two-dimensional radiative equilibrium model and applied it to the Class I object L1551 IRS5. Their calculations adopted so-called Variable Eddington Factor (VEF) method, which can treat the radiation transfer accurately. Kikuchi et al. (2002) performed the reproduction of the emergent SED of the FTTSs by using the detailed model which is carefully treating two-dimensional radiative transfer. Their calculation corresponds to the multi-frequency version of the ZEUS-2D code (Stone, Mihalas, & Norman 1992), which is also using the VEF method to solve the radiative transfer.

1.4 The Goal of This Work

We apply the code used by Kikuchi et al. (2002) to the Class I objects, and construct a two-dimensional protostar model. The principal aim of this work is following three points: first aim of this work is to clarify the importance of the two-dimensional radiative transfer. We show it by comparing the results obtained by the approximate- and full-treatment of the radiative transfer, and comparing the results of spectral fitting with the previous works. Second aim is to establish the general procedure for spectral modeling. This is implicitly suggested by the previous work, but it is important to establish it explicitly because the procedure is effective even when one does not have the detailed numerical model for protostar. Final aim of this work is the application of the procedure to the real object and the estimation of the physical property and evolutionary state of the object that can restrict the theory of the star formation.

In chapter 2, we describe assumptions and the physical parameters of our protostar model. Our model adopts the condition of radiative equilibrium to determine the temperature distribution in the circumstellar matter. The basic equations and numerical method to solve the radiative equilibrium are described in chapter 3. To carry out the spectral modeling, we have to investigate the effects on the emergent SED of each physical parameter of the model. We perform it in chapter 4. From these results, we further establish the procedure to infer the structure of the protostar from the emergent SED, and also establish the method to infer some parameters by introducing the observables which reflect the value of each parameter. These are also given in chapter 4. Based on the results of chapter 4, we try to apply our procedure to the real observation and infer the physical property for two protostars. These results will be described in chapter 5. In chapter 5, we also discuss the evolutionary state implied by the spectral modeling of the objects. Finally, we will conclude in chapter 6.

Chapter 2

Protostar Model

2.1 Overall Structure

As discussed in chapter 1, protostar candidates are not spherically symmetric because they surely have a circumstellar disk, which is progenitor of planetary system, and associate with a bipolar outflow, which probably blows away some part of circumstellar matter. These structures are not spherically symmetric. Thus, to simulate SEDs which have enough accuracy to compare with the observational results quantitatively, it seems unsuitable to use a spherical protostar model. At least, a two-dimensional model, which can represent the disk and the bipolar outflow structure, is needed.

We construct a two-dimensional axisymmetric protostar model. We assume that a protostar consists of three components; a central star, a circumstellar disk, and an envelope. The central star is a hydrostatic object, formed by the collapse of parent molecular cloud core. The circumstellar disk is formed around the central star because infalling materials generally have angular momentum, more or less, so that they cannot accrete directly to the central star. The envelope is surrounding the star-disk system. This is a remnant of the parent molecular cloud core, and finally is dissipated by infalling to the central region or blowing away due to the outflow. Schematic view of our protostar model is shown in Figure 2.1. Details of these components will be explained in the following sections. In our model, density distribution in the circumstellar region is very anisotropic. Thus, the inclination angle i, which is an angle of the direction of the line of sight measured from the symmetric axis, is very important when one tries to infer the structure of the protostar. If we observe a protostar, which has an aspherical structure, from different inclination angle, apparent structure would be very different from each inclination angle. Our model sets the density distribution in the circumstellar disk and the envelope and property of the central star by using some physical parameters that characterize these structure. Thermal structure of the disk and the envelope is calculated from the condition of radiative equilibrium under the radiation field of the central star. In this model, any other heating sources except for the radiation from the central star are ignored, because they are negligible in the region of interest. Detailed procedure to determine the thermal structure of circumstellar region will be described in chapter 3.

2.2 Central Star

The central star is a hydrostatic object, but is not in the main-sequence phase, so the nuclear burning is not an effective energy source. The main energy source is the gravitational energy of infalling material. Infalling material is thermarized at the surface of the central star, and gravitational energy is converted to radiation. Thus, the luminosity of the central star in the protostar phase is equal to the accretion luminosity $L_{\rm acc}$,

$$L_* = L_{\rm acc} = \frac{GM_*\dot{M}}{R_*}, \tag{2.1}$$

where G is the gravitational constant, $\dot{M}$ is mass accretion rate, L_*, M_*, and R_* are luminosity, mass, and radius of the central star, respectively. We assume that the central star is a spherically symmetric energy source and emits the blackbody radiation at temperature T_*. Under the above assumption, the luminosity L_* also can be written as follows:

$$L_* = 4\pi R_*^2 \sigma T_*^4, \tag{2.2}$$

where σ is Stefan-Boltzmann constant. In our model, physical parameters related to the central star are L_*, T_*, and M_*. R_* is not given explicitly, but is evaluated from equation (2.2) and above parameters. We set $T_* = 4000$K and fix for all simulations since the protostar system is optically thick and almost all the radiation of the central star is reprocessed. Thus, the emergent SED is not effected by T_* as long as T_* does not

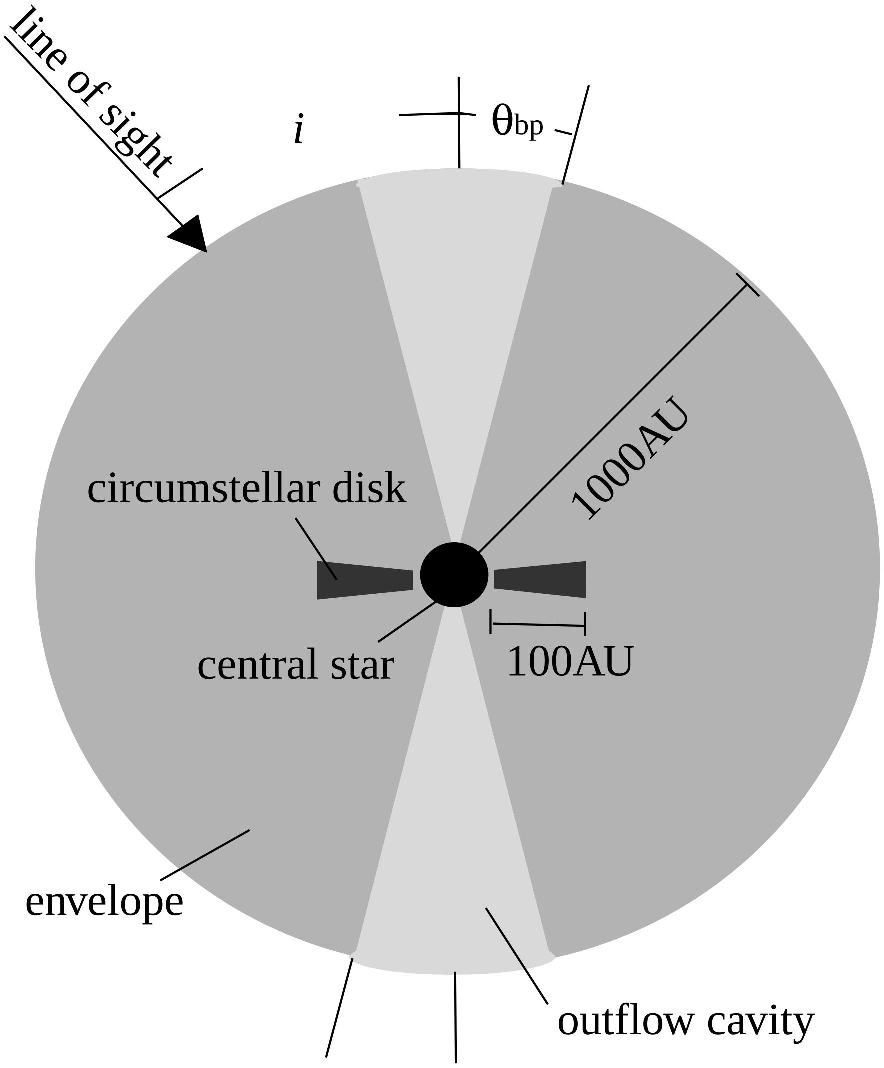

Figure 2.1: Schematic view of our protostar model. This figure shows the section of axisymmetric protostar model. Symmetric axis corresponds to the vertical solid line.

change many orders of magnitude. We also set $M_* = 0.5 M_\odot$ and fix, since this value only affects the vertical structure of the disk. Thus, M_* also does not influence the emergent SEDs. Unfortunately, this fact means that T_* and M_* cannot be determined by the spectral modeling with the present model.

2.3 Circumstellar Disk

We situate the circumstellar disk in the model though a disk is not directly observed in Class I phase to date. But in a Class II phase, which is considered to be a following phase of the Class I phase, circumstellar disk is seen as a 'dark lane' in the near-infrared continuum emission map (e.g. Padgett et al. 1999). Thus, it seems that the disk is formed in the Class I phase. The inner and outer radii of the disk are assumed to be 0.1 AU and 100 AU, respectively. The unit AU is called the astronomical unit and 1 AU $= 1.5 \times 10^{13}$ cm. We also assume that the surface density distribution in the disk $\Sigma(r)$ is given by,

$$\Sigma(r) = \Sigma_1 \left(\frac{r}{1\ \mathrm{AU}} \right)^{-p}, \tag{2.3}$$

where r is the equatorial radius, Σ_1 is the surface density at 1 AU, and p is power law index. We adopt $p = 1.5$, because it is a standard value of the minimum mass solar nebula model (Hayashi, Nakazawa, & Nakagawa 1985). To determine the vertical structure in the disk, we solve the hydrostatic equilibrium between the gravity of the central star and thermal pressure in the disk,

$$-\frac{G M_* \rho_{\mathrm{disk}}(r,z)}{R^2} \cdot \frac{z}{R} = \frac{\partial}{\partial z} \frac{\rho_{\mathrm{disk}}(r,z) k T(r,z)}{\mu m_{\mathrm{H}}}, \tag{2.4}$$

where z is vertical height, $\rho_{\mathrm{disk}}(r,z)$ and $T(r,z)$ are mass density and temperature at a position (r,z), respectively, $R = (r^2 + z^2)^{1/2}$ is distance from the center, μ is mean molecular weight, and $m_{\mathrm{H}} = 1.67 \times 10^{-27}$ g is the mass of atomic hydrogen. For the interstellar matter, μ is evaluated as 2.34, so we adopt this value. Equation (2.4) is a differential equation for ρ_{disk} and it can easily be solved for ρ_{disk},

$$\rho_{\mathrm{disk}}(r,z) = \rho_{\mathrm{disk}}(r,0) \frac{T(r,0)}{T(r,z)} \exp\left[-\int_0^z \frac{\mu m_{\mathrm{H}} G M_*}{k T(r,z)} \frac{z}{R^3} dz \right]. \tag{2.5}$$

The temperature $T(r,z)$ and $T(r,0)$ are given by the radiative equilibrium calculation which will be described in chapter 3. The equatorial density $\rho(r,0)$ is a normalizing factor of the vertical structure, and it is determined from the condition that surface density at r is given by the equation (2.3),

$$\Sigma(r) = \int_{-\infty}^{\infty} \rho_{\rm disk}(r,z) dz. \tag{2.6}$$

Note that disk extends to $z \to \pm\infty$ if we apply equation (2.5) directly to the model. But in practice, we consider not only the disk but also the envelope as a more extended component. Thus, in our model, vertical height of the disk is limited by a height where $\rho_{\rm disk}(r,z)$, given by the equation (2.5), is overwhelmed by the envelope density $\rho_{\rm env}(r,z)$, which will be given in the next section.

In this model, a physical parameter related to the circumstellar disk is Σ_1. Total mass of the disk $M_{\rm disk}$ is obtained from the integral of equation (2.3),

$$M_{\rm disk} = \int_{0.1\,{\rm AU}}^{100\,{\rm AU}} 2\pi r \Sigma(r) dr = \Sigma_1 \int_{0.1\,{\rm AU}}^{100\,{\rm AU}} \left(\frac{r}{1\ {\rm AU}}\right)^{-p} 2\pi r dr, \tag{2.7}$$

which is proportional to the parameter Σ_1.

In practice, the temperature varies during the calculation since we employ an iterative method to solve the radiative equilibrium state. Thus, $\rho_{\rm disk}$ also changes during the calculation, so we update $\rho_{\rm disk}$ according to the temperature change.

2.4 Envelope

We assume the outer radius of the envelope is 1000 AU. This value is slightly small compared to the observation. According to Motte & André (2001), envelope outer radius is estimated to be 4200AU, because this value roughly corresponds to the head of the expansion wave in the inside-out collapse model (Shu 1977), which probably corresponds to the envelope edge, evaluated by a typical age of the Class I object ($\sim 10^5$ yr) and typical sound speed in the cloud (0.2 km s^{-1}, assumed to be $T = 10$ K). In fact, their imaging observation using dust continuum emission at wavelength 1.3 mm revealed that diffuse extended component of this size really exists. Above assumption of our model corresponds to neglecting the outer part of the envelope, but its influence to the whole shape of the SED is small. We assume that the density distribution of the envelope is following a power law, but at $R < 1$ AU, we artificially saturate the density to avoid the divergence of the density at the center,

$$\rho_{\rm env}(R) = \begin{cases} \rho_1 \left(\dfrac{R}{1 \text{ AU}}\right)^{-q} & \text{if } R > 1 \text{ AU}, \\ \rho_1 (1.75 - 0.75 R^2) & \text{if } R < 1 \text{ AU}, \end{cases} \tag{2.8}$$

where ρ_1 is the density at 1 AU and q is index of the power. We assume $q = 1.5$ because theoretical model of the infalling envelope by Shu (1977) predicted this value. The index q has become possible to be measured directly from the intensity profile of the radio or sub-millimeter continuum emission in the outer region of the envelope. Motte & Andeé's survey showed $q \sim 1.5 - 2$ in the region from 1000 AU $< R <$ 5000 AU to 10000 AU $< R <$ 50000 AU for YSOs in Taurus star forming region. Hogerheijde & Sandell (2000) also estimated $q \sim 1 - 2$ for YSOs in Taurus. Thus, this value seems appropriate both from theoretical and observational viewpoint.

Observationally, Class I objects are associated with bipolar molecular outflow. This outflow is considered to originate from the central star-disk system and to be ejected as a result of the magnetohydrodynamical process (Uchida & Shibata 1985; Tomisaka 1998). Outflow blows away some part of the envelope and this forms the bipolar cavity in the envelope. Although the density in the cavity is not known well because the observation of these region is difficult, the existence of the reflection nebula associating with the Class I objects may show that there is a region whose density is thinner than that of the other envelope region. We assume that the cavity has conical shape with half-opening angle $\theta_{\rm bp}$ centered on the symmetric axis and the density in the cavity is 0.01 times the density given by the equation (2.8). Thus, density distribution in the envelope including bipolar cavity is expressed by,

$$\rho_{\rm env}(r, z) = \begin{cases} \rho_{\rm env}(R) & \text{if } \theta > \theta_{\rm bp}, \\ 0.01 \rho_{\rm env}(R) & \text{if } \theta < \theta_{\rm bp}, \end{cases} \tag{2.9}$$

where $\theta = \arctan(r/z)$ is the angle measured from the symmetric axis.

With above assumptions, physical parameters related to the envelope are ρ_1 and $\theta_{\rm bp}$. Total mass of the envelope $M_{\rm env}$ is evaluated from the integral of equation (2.9),

$$M_{\rm env} \sim \int_{\rm V} \rho_{\rm env}(r, z) dV \tag{2.10}$$

$$\sim \quad 2\pi \int_0^{1000\ \mathrm{AU}} \rho_{\mathrm{env}}(R) dR \left(0.01 \int_0^{\theta_{\mathrm{bp}}} \sin\theta d\theta + \int_{\theta_{\mathrm{bp}}}^{2\pi} \sin\theta d\theta \right). \qquad (2.11)$$

From equations (2.8) and (2.11), we can see that the total mass M_{env} is proportional to ρ_1.

2.5 Opacity Model

To determine the temperature distribution in the circumstellar region from the radiative equilibrium, we have to assume an opacity of the circumstellar matter. In a frequency range considered here, it is dust particles that mainly contributes to optical property of the circumstellar matter. We adopt the results of Miyake & Nakagawa (1993) who calculated frequency dependent absorption coefficient per unit mass (opacity) $\kappa_\nu^{\mathrm{abs}}$ and scattering coefficient $\kappa_\nu^{\mathrm{sca}}$ for circumstellar dust particles. They assumed that dust particles have spherical shape with radius a and composed of silicate and water ice. They also assumed that the dust-to-gas mass ratio is 0.01, which is a standard value for the interstellar medium. They calculated $\kappa_\nu^{\mathrm{abs}}$ and $\kappa_\nu^{\mathrm{sca}}$ for a single size dust particle case and a case in which dust particles have a size distribution $n(a)$, which is proportional to $a^{-3.5}$, from minimum size a_{min} to maximum size a_{max}. We adopt that the dust grain have a single size with radius $a = 1\mu$m. Note that the size averaged opacity $\bar{\kappa}_\nu$, defined by

$$\bar{\kappa}_\nu = \frac{\displaystyle\int_{a_{\mathrm{min}}}^{a_{\mathrm{max}}} \kappa_\nu a^3 n(a) da}{\displaystyle\int_{a_{\mathrm{min}}}^{a_{\mathrm{max}}} a^3 n(a) da}, \qquad (2.12)$$

is mainly determined from the maximum size a_{max}, and is not strongly dependent on the minimum size a_{min} when $n(a) \propto a^{-3.5}$. We take in the effect of evaporation of the dust particles by lowering the density when temperature of the dust reaches at evaporation temperature T_{evap}. We also assume the temperature T_{evap} for silicate and water ice to be 1000K and 100K, respectively. The frequency dependence of $\kappa_\nu^{\mathrm{abs}}$ and $\kappa_\nu^{\mathrm{sca}}$ are shown in Figure 2.2.

The absorption coefficient χ_ν^{abs} and scattering coefficient χ_ν^{abs} for each point can be calculated from $\kappa_\nu^{\mathrm{abs}}$ and $\kappa_\nu^{\mathrm{sca}}$,

$$\chi_\nu^{\mathrm{abs}}(r,z) \quad = \quad \rho(r,z)\kappa_\nu^{\mathrm{abs}} \qquad (2.13)$$

$$\chi_\nu^{\rm sca}(r,z) \;=\; \rho(r,z)\kappa_\nu^{\rm sca}. \tag{2.14}$$

2.6 Temperature Distribution

2.6.1 Radiative Equilibrium

We assume that temperature distributions in the circumstellar disk and the envelope are determined by the radiative equilibrium condition,

$$\int_0^\infty \oint \chi_\nu^{\rm abs} B_\nu d\Omega d\nu = \int_0^\infty \oint \chi_\nu^{\rm abs} I_\nu d\Omega d\nu, \tag{2.15}$$

where B_ν is Planck function and I_ν is specific intensity. We assume that dust particles have spherical shape so that $\chi_\nu^{\rm abs}$ and $\chi_\nu^{\rm sca}$ are isotropic. Thus, equation (2.15) is written by,

$$\int_0^\infty \chi_\nu^{\rm abs} B_\nu d\nu = \int_0^\infty \chi_\nu^{\rm abs} J_\nu d\nu, \tag{2.16}$$

where J_ν is mean intensity defined by,

$$J_\nu = \frac{1}{4\pi}\oint I_\nu d\Omega. \tag{2.17}$$

The radiative equilibrium condition represents that the energy emitted from each dust particle (left hand side of equation (2.16)) is equal to the energy absorbed by the dust particle (right hand side of equation (2.16)). Thus, if there is any other process to heat up the dust particles, such as viscous heating, chemical heating, etc., temperature distribution given by the radiative equilibrium is not correct. But these effects are negligible in region considered here. For example, Kikuchi, Nakamoto, & Ogochi (2002) showed that viscous heating is negligible except for the central high temperature region.

As a result, the condition of the radiative equilibrium seems to be valid for the protostar model.

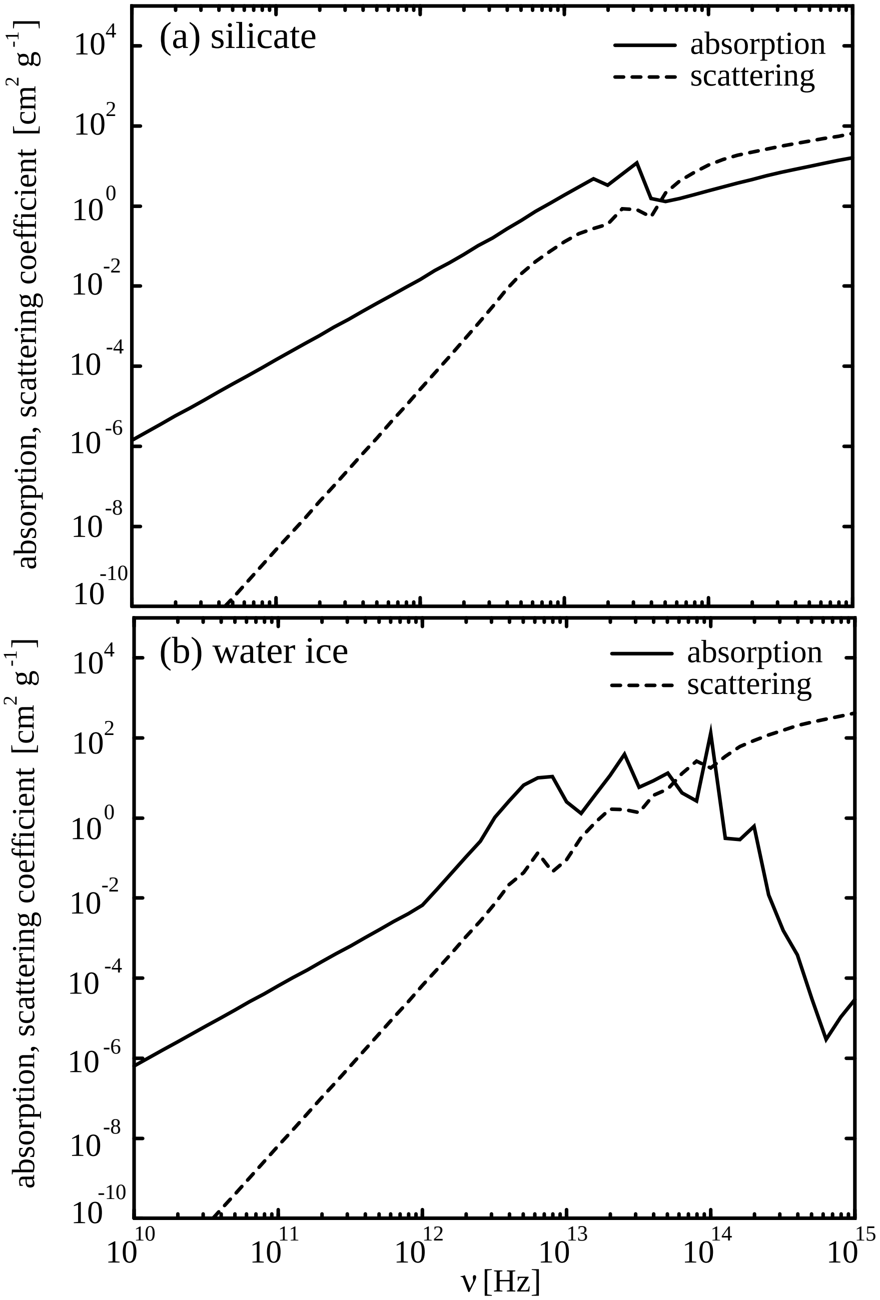

Figure 2.2: The frequency dependence of absorption and scattering coefficients per unit mass for silicate (upper panel) and water ice (lower panel). These data are obtained by assuming that dust particles are spherical and have a radius 1μm. The data are taken from Miyake & Nakagawa (1993).

Chapter 3

Calculation of Radiative Equilibrium

In this chapter, we describe the detailed procedure to obtain the radiative equilibrium temperature distribution. Our calculation method is based on the so-called Variable Eddington Factor method (VEF method; Stone, Mihalas, & Norman 1992), but there are some modifications from the original method. Here, we will describe the essential idea of VEF method first, and details of calculation will be presented next.

3.1 Basic Idea of Variable Eddington Factor Method

The VEF method is introduced by Stone et al. (1992) as a hydrodynamical code including a self-consistent treatment of radiation transfer. The VEF method is one of the methods to solve the radiation moment equations coupled with the hydrodynamical equation. In general, moment equations cannot be closed themselves since nth moment equations always include $(n+1)$th moment. Thus, a certain closure relation is needed to solve the moment equations. In the VEF method, variable Eddington factor $\mathbf{f}$, which is the ratio of the second angular moment of the specific intensity $\mathbf{P}$ to the zeroth moment of the specific intensity E,

$$\mathbf{f} = \frac{\mathbf{P}}{E} = \frac{\oint \mathbf{nn} I d\Omega}{\oint I d\Omega}, \tag{3.1}$$

is introduced as a closure relation. We can obtain the time development of the radiation field by solving moment equations and the closure relation (3.1). Indeed, $\mathbf{f}$ is a tensor having 3×3 components and cannot be determined without knowing radiation field represented by the specific intensity I. Thus, to determine the variable Eddington factor and to solve the moment equations, we must solve the radiation transfer equation to get the specific intensity I for whole spatial points and whole direction at each point. We consider frequency dependence of variable Eddington factor (denoted by the suffix ν; $\mathbf{f}_\nu$), while Stone et al. used the "gray" (frequency independent) radiation field. Thus, the specific intensity is also frequency-dependent and denoted by I_ν.

3.1.1 Radiation Transfer Equation

The frequency-dependent radiation transfer equation is written by

$$\frac{1}{c}\frac{\partial I_\nu}{\partial t} + (\mathbf{n}\cdot\nabla)I_\nu = -\chi_\nu^{\mathrm{ext}}\cdot(I_\nu - S_\nu), \tag{3.2}$$

where c is the speed of light, I_ν is specific intensity, $\chi_\nu^{\mathrm{ext}} = \chi_\nu^{\mathrm{abs}} + \chi_\nu^{\mathrm{sca}}$ is extinction coefficient (see section 2.5), and S_ν is source function. In general, source function is defined by the ratio of emission coefficient to the absorption coefficient. The source function S_ν is written in the form,

$$S_\nu = \frac{1}{\chi_\nu^{\mathrm{ext}}}\left(\chi_\nu^{\mathrm{abs}} B_\nu + \chi_\nu^{\mathrm{sca}} \oint \phi_\nu(\mathbf{n},\mathbf{n}') I_\nu(\mathbf{n}') d\Omega'\right), \tag{3.3}$$

where $\phi_\nu(\mathbf{n},\mathbf{n}')$ is the scattering phase function. If we assume that scattering is isotropic, i.e. $\phi_\nu = 1/4\pi$, then the source function (3.3) is simply given by,

$$S_\nu = \frac{1}{\chi_\nu^{\mathrm{ext}}}(\chi_\nu^{\mathrm{abs}} B_\nu + \chi_\nu^{\mathrm{sca}} J_\nu). \tag{3.4}$$

3.1.2 Monochromatic Moment Equations

The zeroth and first monochromatic radiation moment equation derived from the equation (3.2) and isotropic source function (3.4) are

$$\frac{\partial E_\nu}{\partial t} + \nabla\cdot\mathbf{F}_\nu = 4\pi\chi_\nu^{\mathrm{abs}} B_\nu - c\chi_\nu^{\mathrm{abs}} E_\nu, \tag{3.5}$$

$$\frac{1}{c}\frac{\partial \mathbf{F}_\nu}{\partial t} + c\nabla \cdot \mathbf{P}_\nu = -\chi_\nu^{\mathrm{abs}}\mathbf{F}_\nu, \tag{3.6}$$

where E_ν is the zeroth angular moment of I_ν and corresponds to radiation energy density,

$$E_\nu = \frac{1}{c}\oint I_\nu d\Omega = \frac{4\pi}{c}J_\nu, \tag{3.7}$$

$\mathbf{F}_\nu$ is the first angular moment of I_ν and corresponds to radiation flux density,

$$\mathbf{F}_\nu = \oint \mathbf{n} I_\nu d\Omega, \tag{3.8}$$

and $\mathbf{P}_\nu$ is the second angular moment of I_ν and corresponds to radiation stress tensor,

$$\mathbf{P}_\nu = \frac{1}{c}\oint \mathbf{n}\mathbf{n} I_\nu d\Omega. \tag{3.9}$$

3.1.3 Frequency-Integrated Moment Equations

In practice, we solve frequency-integrated moment equations, which are derived from frequency integration of the equations (3.5) and (3.6),

$$\frac{\partial E}{\partial t} + \nabla \cdot \mathbf{F} = 4\pi\chi_P^{\mathrm{abs}}B - c\chi_E^{\mathrm{abs}}E, \tag{3.10}$$

$$\frac{1}{c}\frac{\partial \mathbf{F}}{\partial t} + c\nabla \cdot \mathbf{P} = -\chi_F\mathbf{F}, \tag{3.11}$$

where B, E, $\mathbf{F}$, and $\mathbf{P}$ are the frequency integration of B_ν, E_ν, $\mathbf{F}_\nu$, and $\mathbf{P}_\nu$, respectively. The opacity χ_P^{abs}, χ_E^{abs}, and χ_F are Planck mean, energy mean, and flux mean opacities, respectively, defined by,

$$\chi_P^{\mathrm{abs}} = \frac{\int_0^\infty \chi_\nu^{\mathrm{abs}} B_\nu d\nu}{\int_0^\infty B_\nu d\nu}, \tag{3.12}$$

$$\chi_E^{\mathrm{abs}} = \frac{\int_0^\infty \chi_\nu^{\mathrm{abs}} E_\nu d\nu}{\int_0^\infty E_\nu d\nu}, \tag{3.13}$$

and,

$$\chi_F = \frac{\int_0^\infty \chi_\nu^{\mathrm{abs}} \mathbf{F}_\nu d\nu}{\int_0^\infty \mathbf{F}_\nu d\nu}. \tag{3.14}$$

The second moment $\mathbf{P}$ is rewritten with the zeroth moment E and the variable Eddington factor $\mathbf{f} = \int_0^\infty \mathbf{f}_\nu d\nu$, as

$$\mathbf{P} = \mathbf{f}E. \tag{3.15}$$

In principle, the set of moment equations (3.5) and (3.6) are closed by the equation (3.15). The values of $\mathbf{f}$, χ_P^{abs}, χ_E^{abs}, and χ_F are calculated from radiation field represented by the specific intensity I_ν.

3.2 Division of Radiation Field

We assume that the radiation field I_ν is divided into two components. One is a direct component from the central star I_ν^* and the other is a diffuse component I_ν^{diff}, i.e.

$$I_\nu = I_\nu^* + I_\nu^{\text{diff}}. \tag{3.16}$$

We can calculate the contribution of the direct component I_ν^* by using the optical depth from the center $\tau_\nu = \int_0^R \chi_\nu^{\text{ext}} dR$,

$$I_\nu^* = \frac{L_\nu^*}{4\pi R^2} \exp(-\tau_\nu)\delta(\mathbf{n} - \mathbf{n}^*), \tag{3.17}$$

where delta function indicates that the direct component I_ν^* is non-zero only when the direction $\mathbf{n}$ is in the direction from the center to the spatial point being considered. We can obtain the radiation field by solving the moment equations of diffuse component since we can evaluate the direct component from equation (3.17). The frequency-integrated moment equations for the diffuse component are written in the form,

$$\frac{\partial E}{\partial t} + \nabla \cdot \mathbf{F} = 4\pi\chi_P^{\text{abs}} B - c\chi_E^{\text{abs}} E + 4\pi \int_0^\infty \chi_\nu^{\text{sca}} J_\nu^* d\nu, \tag{3.18}$$

$$\frac{1}{c}\frac{\partial \mathbf{F}}{\partial t} + c\nabla \cdot \mathbf{P} = -\chi_F \mathbf{F}, \tag{3.19}$$

where asterisk shows the quantity of direct component and we omitted the index "diff" in the diffuse component.

3.3 Coupling with Energy Equation

To obtain the temperature of the dust grains, we must couple the energy equation of the gas/dust grains with the moment equations mentioned in section 3.1 and 3.2. Since we neglected any other heating source except for the radiation, the internal energy of the gas per unit volume e is determined by the balance between the absorption and the emission of the radiation. Thus,

$$\frac{\partial e}{\partial t} = -4\pi \chi_P^{\rm abs} B + c\chi_E^{\rm abs} E + 4\pi \int_0^\infty \chi_\nu^{\rm abs} J_\nu^* d\nu. \tag{3.20}$$

The moment equations of diffuse component coupled with the energy equation are as follows,

$$\frac{\partial (e+E)}{\partial t} + \nabla \cdot \mathbf{F} = 4\pi \int_0^\infty (\chi_\nu^{\rm abs} + \chi_\nu^{\rm sca}) J_\nu^* d\nu, \tag{3.21}$$

$$\frac{1}{c}\frac{\partial \mathbf{F}}{\partial t} + c\nabla \cdot \mathbf{P} = -\chi_F \mathbf{F}. \tag{3.22}$$

We solve the equations (3.20), (3.21), and (3.22) using the variable Eddington factor of the diffuse component (3.15) and mean opacities (3.12), (3.13), and (3.14) and follow the time evolution of radiation field until the radiative equilibrium is achieved. The temperature T is calculated from e, as

$$T = \frac{(\gamma - 1)\mu m_{\rm H} e}{\rho k}, \tag{3.23}$$

where γ is adiabatic exponent.

3.4 Numerical Method

We discretize the above equations in the time, space, direction, and frequency to solve these equations numerically. We divide the 1000 AU × 1000 AU region into 50 × 50 non-uniform spatial grids for $r \times z$ and 100 × 50 grids for direction $\theta \times \phi$ and divided frequency from 10^{10} Hz to 10^{15} Hz into 51 grids.

3.4.1 Moment Equation Solver

In this section, we describe numerical method to solve the moment equations, provided the variable Eddington factor is given.

Spatial Grid and Definition of Variables

We solve moment equations using the two dimensional (r, z) coordinates. We put up the non-uniform rectangular spatial grid, which has finer grid interval near the center, because central structure is important to evaluate the temperature distribution in the envelope. We assume that the z-axis is the axis of the symmetry, and r-axis is normal to the z-axis and corresponds to the equatorial plane.

According to moment equations, radiation energy density is determined by the divergence of radiation flux density. Similarly, radiation flux density is determined by the divergence of radiation stress tensor. Thus, we define the variables E, B, e, χ_P, and χ_E at cell center. Since divergence of flux $\mathbf{F}$ is related to E, $\mathbf{F}$ must be defined at cell surface. Similarly, $\mathbf{P}$ has to be defined at cell center for diagonal element, and in cell corner for off-diagonal ones. These situations are illustrated in Figure 3.1.

Newton-Raphson Iteration

When the variables of nth time step (denoted by the suffix "n") is given, the $(n+1)$th variables are obtained by the following discretized equations,

$$\frac{(e^{\mathrm{n+1}} - e^{\mathrm{n}})}{\Delta t} = -4\pi\chi_P^{\mathrm{abs}} B^{\mathrm{n+1}} + c\chi_E^{\mathrm{abs}} E^{\mathrm{n+1}} + 4\pi \int_0^\infty \chi_\nu^{\mathrm{abs}} J_\nu^* d\nu, \tag{3.24}$$

$$\frac{(e^{\mathrm{n+1}} + E^{\mathrm{n+1}}) - (e^{\mathrm{n}} + E^{\mathrm{n}})}{\Delta t} + (\nabla \cdot \mathbf{F})^{\mathrm{n+1}} = 4\pi \int_0^\infty (\chi_\nu^{\mathrm{abs}} + \chi_\nu^{\mathrm{sca}}) J_\nu^* d\nu, \tag{3.25}$$

$$\frac{\mathbf{F}^{\mathrm{n+1}} - \mathbf{F}^{\mathrm{n}}}{c\Delta t} + c(\nabla \cdot \mathbf{f} E)^{\mathrm{n+1}} = \chi_F \mathbf{F}^{\mathrm{n+1}}, \tag{3.26}$$

where Δt is time interval between nth and $(n+1)$th time steps. We used the closure relation (3.15).

The discretized equations (3.24), (3.25), and (3.26) are nonlinear with respect to the variables e and E because χ and B depend on these variables. Thus, we need to linearize these equations to obtain a solution numerically. We solved the equations using the Newton-Raphson Iteration (NRI) method. Here, we now consider a problem where certain i coupled non-linear equations for j variables are given, which are written as

$$\boldsymbol{f}(\boldsymbol{x}) = 0. \tag{3.27}$$

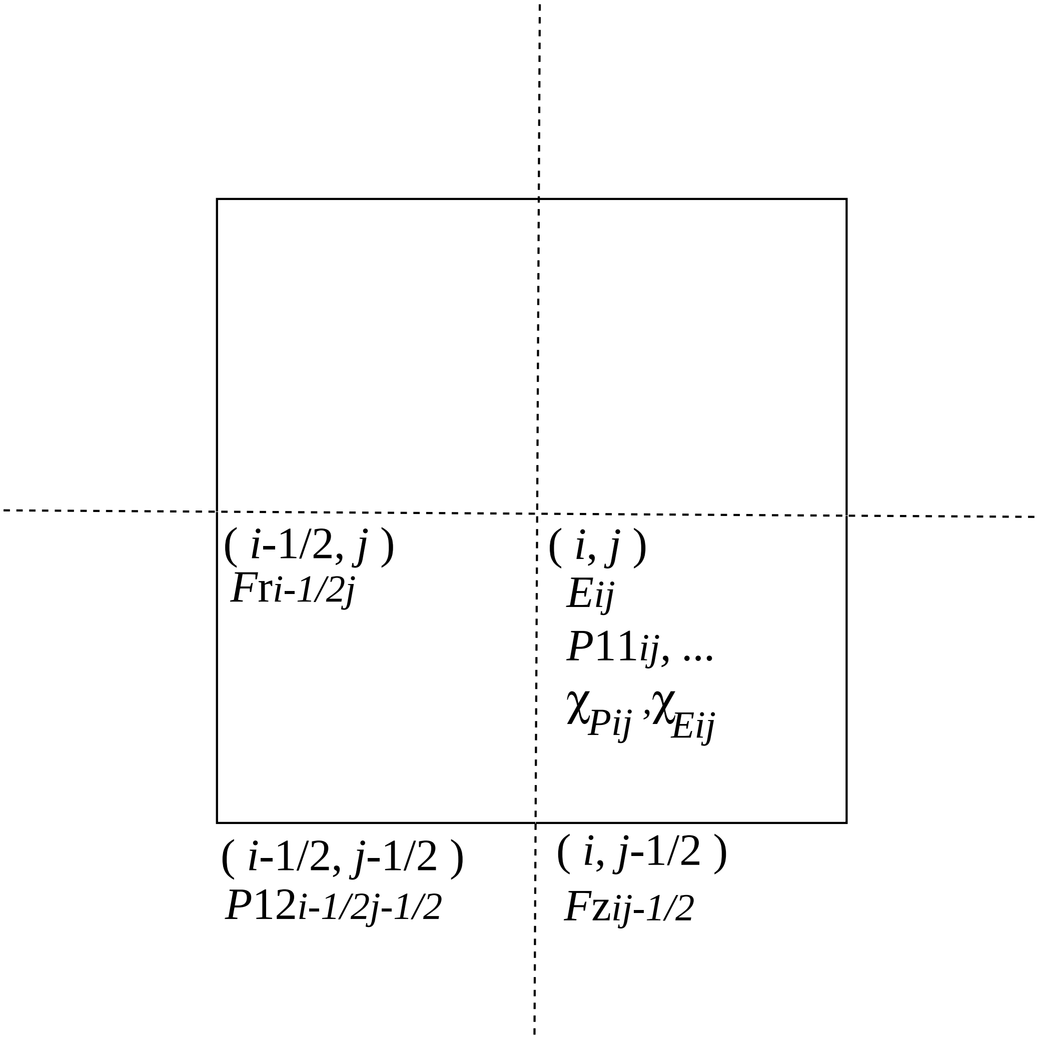

Figure 3.1: Schematic view of variables. Solid line shows the surface of cell (i, j), while dashed line shows the main grid whose cross points show the cell center. Radiation energy density E, mean opacities, and diagonal element of radiation stress tensor $\mathbf{P}$ are defined at cell center. On the other hand, radiation flux density $\mathbf{F}$ is defined on cell surface and off-diagonal elements of $\mathbf{P}$ is defined in cell corner where solid line crosses.

(Equation (3.27) is a symbolic form. Indeed, $\boldsymbol{f}$ represents a set of equations $f_1(\boldsymbol{x}) = 0, f_2(\boldsymbol{x}) = 0, ..., f_i(\boldsymbol{x}) = 0$, and $\boldsymbol{x}$ represents a set of variables $x_1, x_2, ..., x_j$.) In the NRI method, we choose an initial guess $\boldsymbol{x}^{\mathrm{k}}$ of the solution first and then solve the equation

$$\mathbf{J}(\delta\boldsymbol{x}^{\mathrm{k}}) = -\boldsymbol{f}(\boldsymbol{x}^{\mathrm{k}}), \tag{3.28}$$

where $\mathbf{J}(\delta\boldsymbol{x}^{\mathrm{k}})$ is the Jacobian of $\boldsymbol{f}(\boldsymbol{x})$. The correction term $\delta\boldsymbol{x}^{\mathrm{k}}$ is computed from equation (3.28) and the solution is updated from the initial guess to,

$$\boldsymbol{x}^{\mathrm{k+1}} = \boldsymbol{x}^{\mathrm{k}} + \delta\boldsymbol{x}^{\mathrm{k}}, \tag{3.29}$$

and this procedure is iterated until the solution is converged, i.e. $\delta\boldsymbol{x}^{\mathrm{k}}$ becomes less than a certain small convergence criterion. Note that equation (3.28) is always linear even if the original equation (3.27) is nonlinear. Thus, NRI method is useful to solve nonlinear equation numerically.

We divide the numerical procedure into two steps to solve the moment equations. We solve only energy equation by NRI method first and update the gas internal energy e (i.e. temperature T) for each time step. Next we solve the moment equation to update the radiation energy density E by using the already updated gas internal energy e. On the contrary, Stone et al. update e and E simultaneously. Our method has an advantage over the numerical method of Stone et al. in the economy of the total amount of computation.

Newton-Raphson Iteration for Energy Equation

We first solve the energy equation (3.24) to update the gas internal energy e. The equation corresponding to (3.27) is now given by

$$\frac{e - e^{\mathrm{old}}}{\Delta t} + 4\pi\chi_P^{\mathrm{abs}} B^{\mathrm{n+1}} - c\chi_E^{\mathrm{abs}} E^{\mathrm{n}} - 4\pi \int_0^\infty \chi_\nu^{\mathrm{abs}} J_\nu^* d\nu = 0, \tag{3.30}$$

where we rewrite $e^{\mathrm{n+1}} \to e$ and $e^{\mathrm{n}} \to e^{\mathrm{old}}$ to avoid a confusion of an index for the time step of main calculation loop and an index for the iterative cycle of NRI method. Note that we use the radiation energy density E at nth time step on the left hand side of equation (3.30), while equation (3.24) uses the value of E at $(n+1)$th time step. This is justified because we compute the equilibrium state of the radiation field and difference of the variables in nth and $(n+1)$th time steps is very small near the equilibrium state. We omitted the suffix (i, j) showing the spatial grid point (i and j correspond to r-direction and z-direction, respectively) for simplicity because, in this case, equation (3.30) is written only by the variables at one grid point and independent of the variables at other grid points. This means that the Jacobian matrix is purely diagonal so that equation for iterative cycle is easily obtained. The equation to update from e^{k} to $e^{\mathrm{k+1}}$ is written as

$$e^{\mathrm{k+1}} = e^{\mathrm{k}} \cdot \frac{\dfrac{e^{\mathrm{old}}}{\Delta t} + 12\chi_P^{\mathrm{abs}} B^{\mathrm{n+1}} + c\chi_E^{\mathrm{abs}} E^{\mathrm{n}} + 4\pi \displaystyle\int_0^\infty \chi_\nu^{\mathrm{abs}} J_\nu^* d\nu}{\dfrac{e^{\mathrm{k}}}{\Delta t} + 16\chi_P^{\mathrm{abs}} B^{\mathrm{n+1}}}. \tag{3.31}$$

Newton-Raphson Iteration for Moment Equations

The equation corresponding to (3.27) is given by

$$\frac{(e_{i,j} + E_{i,j}) - (e_{i,j}^{\mathrm{old}} + E_{i,j}^{\mathrm{old}})}{\Delta t} + (\nabla \cdot \mathbf{F})_{i,j} - 4\pi \left[\int_0^\infty \chi_\nu^{\mathrm{ext}} J_\nu^* d\nu \right]_{i,j} = 0, \tag{3.32}$$

where $\chi_\nu^{\mathrm{ext}} = \chi_\nu^{\mathrm{abs}} + \chi_\nu^{\mathrm{sca}}$, and we rewrite $e^{\mathrm{n+1}} \rightarrow e$, $E^{\mathrm{n+1}} \rightarrow E$, $e^{\mathrm{n}} \rightarrow e^{\mathrm{old}}$, and $E^{\mathrm{n}} \rightarrow E^{\mathrm{old}}$ from the same reason of equation (3.30). We also omitted the suffix (n+1) of flux density $\mathbf{F}$ for simplicity. The second term on the left hand side of equation (3.32) is the divergence of flux density $\mathbf{F}$. This is evaluated as

$$(\nabla \cdot \mathbf{F})_{i,j} = (\mathbf{F}_{\mathrm{r}})_{i-1/2,j} - (\mathbf{F}_{\mathrm{r}})_{i+1/2,j} + (\mathbf{F}_{\mathrm{z}})_{i,j-1/2} - (\mathbf{F}_{\mathrm{z}})_{i,j+1/2}. \tag{3.33}$$

Jacobian matrix elements are obtained by the derivative of equation (3.32). Each value on the right hand side of equation (3.33) is calculated by equation (3.26). From equation (3.26), flux density for each grid surface is determined by the energy density at six grid points surrounding the surface, since equation (3.26) has the form that flux density is determined by the divergence of radiation stress tensor expressed by (variable Eddington factor) × (energy density). For example, $(\mathbf{F}_{\mathrm{r}})_{i+1/2,j}$ depends on the energy density at grid points $(i, j-1)$, $(i+1, j-1)$, (i, j), $(i+1, j)$, $(i, j+1)$, and $(i+1, j+1)$. As a result, the energy density at grid point (i, j) is depending on itself and that of surrounding eight grid points. Thus, Jacobian matrix computed by equation (3.32) is not diagonal and the problem to update the energy density E results in the inversion of the Jacobian matrix.

$$\begin{pmatrix} E^{\mathrm{k}+1}_{1,1} \\ E^{\mathrm{k}+1}_{2,1} \\ \vdots \\ E^{\mathrm{k}+1}_{N,1} \\ E^{\mathrm{k}+1}_{1,2} \\ E^{\mathrm{k}+1}_{2,2} \\ \vdots \\ E^{\mathrm{k}+1}_{N,N} \end{pmatrix} = \begin{pmatrix} E^{\mathrm{k}}_{1,1} \\ E^{\mathrm{k}}_{2,1} \\ \vdots \\ E^{\mathrm{k}}_{N,1} \\ E^{\mathrm{k}}_{1,2} \\ E^{\mathrm{k}}_{2,2} \\ \vdots \\ E^{\mathrm{k}}_{N,N} \end{pmatrix} - J^{-1} \cdot \begin{pmatrix} f^{\mathrm{k}}_{1,1} \\ f^{\mathrm{k}}_{2,1} \\ \vdots \\ f^{\mathrm{k}}_{N,1} \\ f^{\mathrm{k}}_{1,2} \\ f^{\mathrm{k}}_{2,2} \\ \vdots \\ f^{\mathrm{k}}_{N,N} \end{pmatrix}, \tag{3.34}$$

where J^{-1} is the inverted Jacobian matrix, and f is the left hand side of equation(3.32). The Jacobian in this case is a (number of spatial grid) × (number of spatial grid) square matrix. On the contrary, Stone et al. regard e and E as the variable of NRI method for each grid point. Thus, Jacobian of Stone et al. has 4 times larger size compared with our method.

3.4.2 Radiation Transfer Equation Solver

In this section, we describe numerical method to obtain the variable Eddington factor under a certain stationary state. The variable Eddington factor $\mathbf{f}_\nu$ is the ratio of second to zeroth moment of specific intensity I_ν. Thus it is computed easily from equation (3.1) if we know the specific intensity for all direction at each grid point. The specific intensity is obtained by radiation transfer equation (3.2) for stationary state, i.e. $\partial I_\nu/\partial t = 0$. But integration of radiation transfer equation is difficult since it includes the source function S, which depends on the temperature T (emission term), determined from interaction between gas and radiation field, and specific intensity of all grid points (scattering term). If we know the source function at all grid points, we can compute I_ν from radiative transfer equation. That is to say, the problem to obtain the specific intensity is equal with the problem to get the source function. We solved equation (3.2) to obtain the source function by using the Accelerated Lambda Iteration (ALI) method, described below.

Spatial Grid for Radiation Transfer Equation Solver

Since the specific intensity I depends on the direction of the ray, we need to solve the radiation transfer equation in a three-dimensional space. Thus, we must expand the temperature and radiation variables computed by moment equations in two-dimensional coordinates. But it is easy because we assume axial symmetry around the z-axis. We set new spatial coordinates (x, z) for transfer equation solver, illustrated in Figure 3.2. We set θ and ϕ, which represent a direction of the ray, at each grid point, as shown in Figure 3.3.

Accelerated Lambda Iteration

The radiative transfer equation for stationary state is written in the form

$$\frac{\partial I}{\partial s} = -\chi^{\mathrm{ext}}(I - S), \tag{3.35}$$

where we omit the subscript "ν" for simplicity, and we use $\nabla \cdot I = \partial I/\partial s$, where the line element ds is measured along the ray. The isotropic source function is

$$S = \frac{\chi^{\mathrm{abs}}B + \chi^{\mathrm{sca}}J}{\chi^{\mathrm{ext}}} = (1 - \omega)B + \omega J, \tag{3.36}$$

where ω is single scattering albedo. We discretize the variables I to I_i and S to S_i and define them at the grid center. The subscript "i" is in a symbolic form, includes the information of the grid point. The specific intensity I can be obtained by the integral of equation (3.35) along the ray. Here, we introduce Λ-operator, $\Lambda = (\lambda_{i,j})$, which is written by

$$I_i = \sum_{j(\mathrm{upwind})} \lambda_{i,j} S_j + I_j^{\mathrm{b}}, \tag{3.37}$$

where summation is performed for upwind from boundary to each point and I^{b} is the contribution from the boundary. Since S_j is isotropic, we can write for mean intensity J,

$$J_i = \sum_{j(\mathrm{upwind})} \lambda_{i,j} S_j + J_j^{\mathrm{b}}. \tag{3.38}$$

We rewrite equation (3.38) in a symbolic form,

$$J = \Lambda(S) + J^{\mathrm{b}}, \tag{3.39}$$

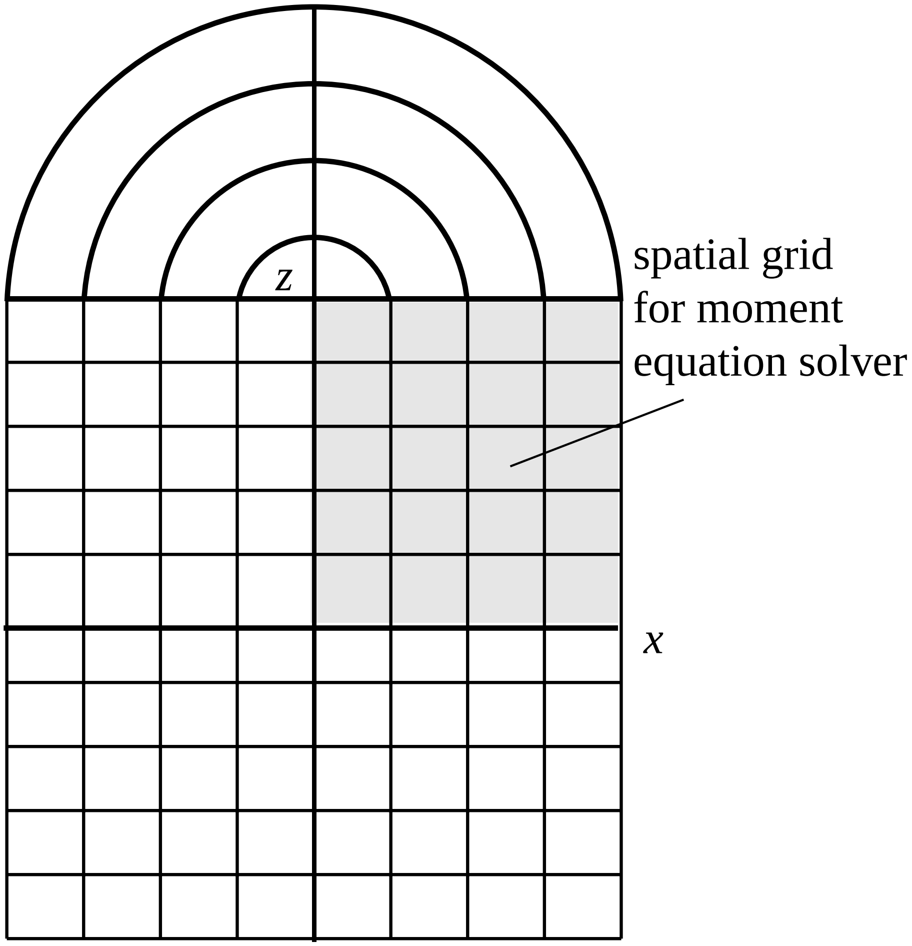

Figure 3.2: Schematic view of the grid for radiation transfer equation solver. The axis of symmetry is set to be the z-axis. We also assume that upper and lower regions are symmetric with respect to $x-y$-plane.

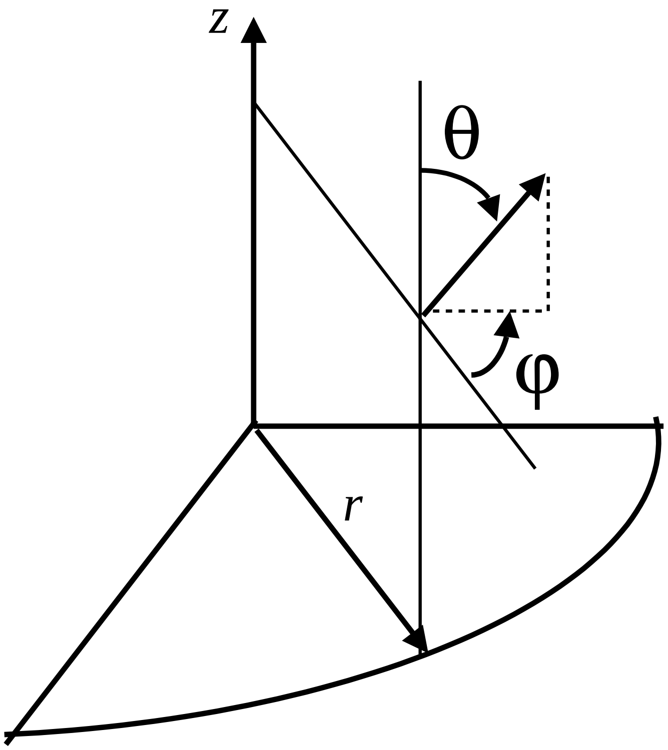

Figure 3.3: Schematic view of definition of θ and ϕ representing the direction of ray.

for simplicity. From equations (3.36) and (3.39), we can obtain a following formula

$$(1-\omega\Lambda)S=(1-\omega)B+\omega J^{\mathrm{b}}, \tag{3.40}$$

since the Λ-operator is a linear operator. The Λ-operator is a square matrix with dimension (number of grids) × (number of grids). Thus, the problem to solve the equation (3.40) with respect to S results in the inversion of matrix $(1-\omega\Lambda)$. Direct inversion of the matrix $(1-\omega\Lambda)$ is difficult, so we solve it using an iteration method.

We used the Accelerated Lambda Iteration (ALI) method to solve the equation (3.40). In the normal lambda iteration, when we know nth value of mean intensity and source function J^{n} and S^{n}, we update the variables to next step by the equation

$$\begin{cases} S^{\mathrm{n+1}}=(1-\omega)B+\omega J^{\mathrm{n}} \\ J^{\mathrm{n+1}}=\Lambda(S^{\mathrm{n+1}})+J^{\mathrm{b}}, \end{cases} \tag{3.41}$$

which are corresponding to equations (3.36) and (3.39). This iteration is slow to converge when the system is optically thick. Protostar is a mixed system of the optically thick and thin regions. Thus, direct application of equation (3.41) is unsuitable. We improve the iterative cycle to ALI form as follows:

$$\begin{cases} S^{\mathrm{n+1}}=\dfrac{(1-\omega)B+\omega(J^{\mathrm{n}}-\Lambda_{\mathrm{d}}S^{\mathrm{n}})}{1-\omega\Lambda_{\mathrm{d}}} \\ J^{\mathrm{n+1}}=\Lambda(S^{\mathrm{n+1}})+J^{\mathrm{b}}, \end{cases} \tag{3.42}$$

where $\Lambda_{\mathrm{d}}=\Lambda-\Delta\Lambda$ is modified Λ-operator, having the diagonal elements of the Λ-operator, $\Lambda_{\mathrm{d}}=(\lambda_{i,i})$.

This form is obtained as follows. When we update from S^{n} to $S^{\mathrm{n+1}}$, we use $\tilde{J}^{\mathrm{n+1}}$, which is defined by

$$\tilde{J}^{\mathrm{n+1}}=J^{\mathrm{n}}+\Lambda_{\mathrm{d}}(S^{\mathrm{n+1}}-S^{\mathrm{n}}), \tag{3.43}$$

instead of J^{n}. $\tilde{J}^{\mathrm{n+1}}$ is obtained by the second equation of (3.41) by substituting

$$\begin{cases} \Lambda=\Lambda_{\mathrm{d}}+\Delta\Lambda \\ S^{\mathrm{n+1}}=S^{\mathrm{n}}+\Delta S^{\mathrm{n}}, \end{cases} \tag{3.44}$$

and neglecting the term $\Delta\Lambda(\Delta S^{\mathrm{n}})$. The matrix $\Delta\Lambda$ is the residual matrix picking the off-diagonal elements out from the matrix Λ, and ΔS^{n} is correction term to update from the nth to the $(n+1)$th iterative cycle. Thus, $\tilde{J}^{\mathrm{n}+1}$ is the value that is updated from nth to $(n+1)$th iterative cycle only using a contribution of the source function at the same spatial point.

We update J^{n} and S^{n} until the difference from the previous step becomes less than the convergence criterion.

Once we obtain the source function with ALI, we can calculate the specific intensity I_ν with the radiative transfer equation. Further, one can calculate the variable Eddington factor $\mathbf{f}_\nu$ from I_ν. The integration of radiative transfer equation to obtain the intensity I_ν in all direction at each grid takes huge calculations and needs large amount of time. But we can reduce some amount of calculations by using axial symmetry and Impact Parameter Method which will be described below.

Impact Parameter Method

When we solve the radiative transfer equation, the azimuthal angle ϕ can be converted to an impact parameter b by making use of the axial symmetry (Figure 3.4). In Figure 3.4, filled circles belonging to the same spherical shell are equivalent with each other because of the axial symmetry around z-axis. Thus, once we compute the specific intensity I_ν for angle ϕ at a certain grid point included in a certain shell, we can use this value to the other grid point in that shell. That is, solving the radiation transfer equation for various values of ϕ at a certain grid point is equivalent to solving that for various impact parameters.

3.4.3 SED Calculation

We can calculate SED by solving the radiative transfer equation (3.2) for any inclination angle i if we know the source function in the radiative equilibrium state for all direction at all grid points. The emergent SED is obtained from the surface integral of the flux over the apparent size of the model

$$\boldsymbol{F}_\nu^{\mathrm{total}} = \int_S \boldsymbol{F}_\nu dS. \tag{3.45}$$

But it is conventionally used the value νL_ν, rather than $\boldsymbol{F}_\nu$ itself, which is defined by

$$\nu L_\nu = 4\pi D^2 \nu |\boldsymbol{F}_\nu^{\mathrm{total}}|, \tag{3.46}$$

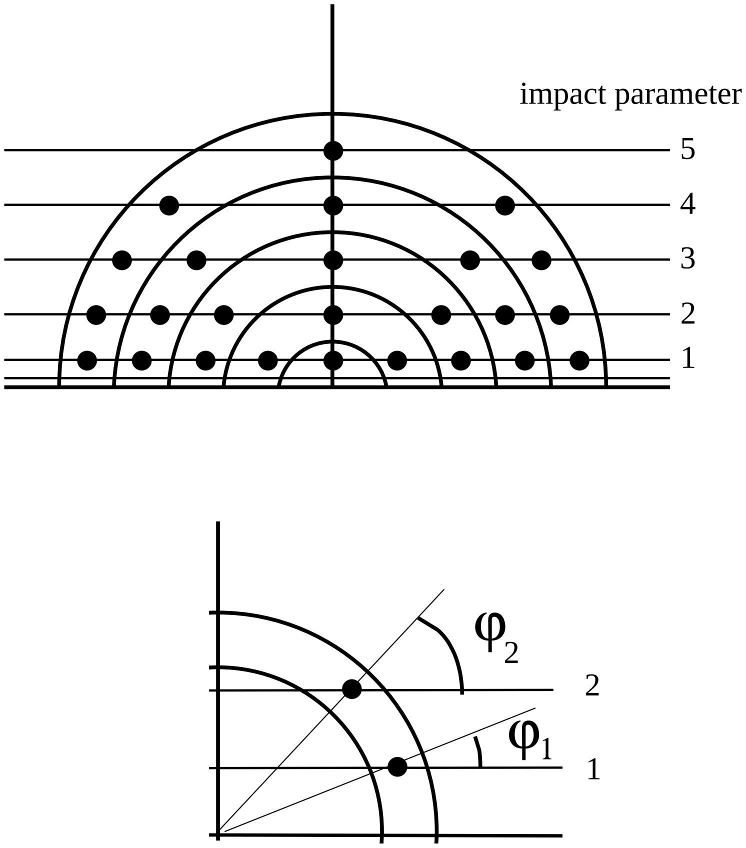

Figure 3.4: Schematic view of the impact parameter method. Upper panel displays the protostar system viewed from the symmetric axis (z-axis). Filled circles in the figure show grid points for radiation transfer equation solver. Filled circles in the same spherical shell are equivalent with each other due to the axial symmetry. We assume that the ray propagates along the line classified by the impact parameter from left to right. Lines having different impact parameter cross with a shell by different angles ϕ (lower panel). Thus, the calculations for the shell with rays having different impact parameters are equivalent with calculations of the ray with different angles ϕ at one point.

where D is the distance from the observer to the object, and $L_\nu = 4\pi D^2 |\boldsymbol{F}_\nu^{\rm total}|$ is the total luminosity emitted in a certain frequency range. This value is useful when we estimate the emergent luminosity from SED since the area of the SED in the $\log\nu - \nu L_\nu$ plane becomes the emergent luminosity, then we only integrate the SED to estimate the emergent luminosity.

Note that νL_ν is not a true luminosity of a central star because protostar system is not a spherically symmetric system while equation (3.46) assumes that the system is spherically symmetric. Thus we have to determine the true luminosity from the other property of the SED.

Chapter 4

Relation between Emergent SED and the Structure of a Protostar

In this chapter, we describe our main results based on the two-dimensional protostar model. We first describe about the emergent SED. Further, we have compared the semi-two dimensional calculation, which is equivalent to that carried out by the Kenyon et al. (1993), with our calculation. We also discuss about the results. Next, we describe the results with respect to the effects of some primal physical parameters on the emergent SED. At final section of this chapter, we discuss the method how to infer these parameters from the emergent SEDs based on the dependence of physical parameters.

4.1 Emergent Spectral Energy Distribution

Emergent SEDs calculated from our model are shown in Figure 4.1. It is clearly seen from Figure 4.1 that the emergent SED is strongly dependent on the inclination angle. It is also seen that the emergent SED has characteristic feature which peaks at $\nu_{\rm peak} \sim 10^{12.5}$Hz. This feature is completely different from the spectrum of the central star. This is because that we considered the frequency-dependent opacity model, and thus protostar system is both optically thick and thin for the frequency we observed. From Figure 2.2, opacity κ_ν has larger value for the high frequency radiation, while smaller for the low frequency. Thus, the disk and the envelope is optically thick for the frequency range

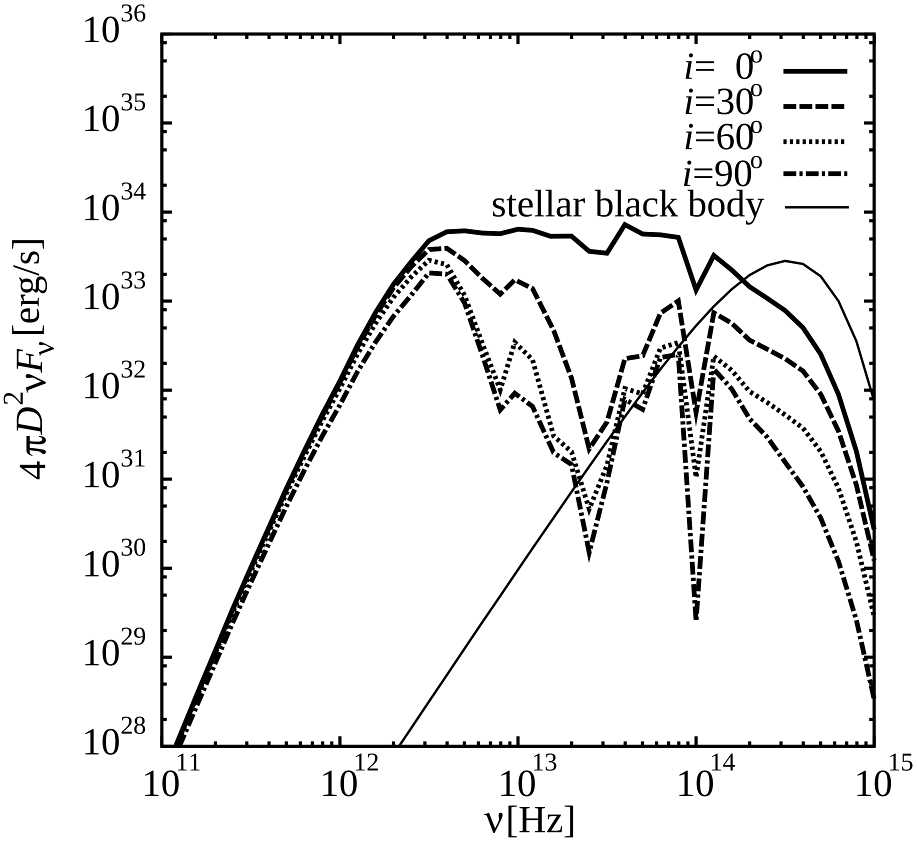

Figure 4.1: Emergent spectral energy distribution (SED) with the present protostar model. Adopted parameters are $L_* = 1L_\odot$, $\rho_1 = 10^{-13}$ g cm^{-3}, $\Sigma_1 = 2000$ g cm^{-2}, and $\theta_{\rm bp} = 25°$. Four thick curves represent SEDs with the inclination $i = 0°$ (solid curve), 30° (dashed curve), 60° (dotted curve), and 90°(dot-dashed curve), respectively. Thin solid curve represents spectrum of the central star, which assumed black body at temperature $T_* = 4000$K. It is seen that the SED changes with the inclination i, even though the protostar structure does not change. The emergent luminosity $L_{\rm SED}$ also changes with the inclination.

that almost energy from the central star is emitted, and emergent SED is dominated by the reprocessed component that is thermal emission from the dust particles, heated by the absorption of the radiation from the central star. The asymmetry of the SED is also based on the fact that the circumstellar components are optically thick, and these have asymmetric structure. Absorbed radiation is used to heat up the dust particles and re-emitted at lower frequency range. This re-emitted radiation is isotropic because the system is optically thin for this radiation, while scattered radiation is anisotropic reflecting the anisotropy of density distribution. Thus, flux in lower frequency range, dominated by the thermal radiation of the dust, is almost independent of the inclination, while flux in higher frequency is strongly dependent on.

But, the re-emitted radiation becomes optically thick if the temperature of the radiation become high, or envelope is very dense. In this case, SED is not isotropic even if the re-emitted radiation is dominated by the total flux. That is, re-emitted radiation is, more precisely, isotropic as long as the system is optically thin for the frequency corresponding to the black body temperature. Thus, the border frequency between the isotropic and the anisotropic feature of emergent SED is corresponding to the frequency that the optical depth of the system is roughly ~ 1.

Because of the dominance of the reprocessing component, we can infer the circumstellar structure from the emergent SED. On the other hand, it is difficult to investigate the physical property of the embedded central star from SED.

4.2 Comparison with the Semi- and Full-Two Dimensional Calculations

Kenyon et al. (1993) calculated SED to fit various observational results from two-dimensional density distribution and spherically symmetric temperature distribution. This spherical temperature is obtained from the one-dimensional radiative transfer calculation under the spherically averaged density distribution of original two-dimensional one. This method is relatively simple because radiative transfer calculation become easy compared with the two-dimensional. On the other hand, temperature distribution obtained from the above procedure is not consistent with the original density distribution.

Thus, we examined whether this procedure is applicable to the protostar or not based on our model and calculation (Nakazato, Nakamoto, & Umemura 2003).

We follow the procedure carried out by Kenyon et al. First, we determined the spherically averaged density distribution

$$\bar{\rho}(R) = \frac{1}{4\pi} \oint \rho(R) d\Omega. \tag{4.1}$$

We next calculated the temperature distribution and radiation field consistently under this spherically symmetric density distribution. (Note that we used two-dimensional calculation here, although all the variables are written by the distance from the center R. Thus, our procedure is not precisely same to Kenyon et al.) Then finally, we calculated SED from two-dimensional density distribution and spherically symmetric results for temperature and radiation field, and compared with calculation using two-dimensional density distribution.

Figure 4.2 shows temperature distributions of semi- and full-two dimensional calculation, where 'semi-' means the procedure similar to Kenyon et al., while 'full-' is our original calculation. Parameters adopted here are as follows: $L_* = 1L_\odot$, $\rho_1 = 10^{-13}$ g cm^{-3}, $\Sigma_1 = 2000$ g cm^{-2}, and $\theta_{\rm bp} = 25°$. In the above situation, spherically averaged density in the envelope is

$$\bar{\rho}_{\rm env} \sim \rho_{\rm env} \int_{25°}^{90°} \sin\theta d\theta \sim 0.91 \rho_{\rm env}. \tag{4.2}$$

From Figure 4.2, we showed that there are at least three differences between two temperature distributions; (1) temperature in the disk of the semi-two dimensional temperature is approximately 20% higher than the full-two dimensional one, (2) the shaded region, which is behind the disk with respect to the central star, has also approximately 40% higher temperature in the semi-two dimensional calculation than the full-two dimensional one, and (3) temperature in the outflow cavity computed from the semi-two dimensional calculation is, in contrast, several times 10 % lower than the full-two dimensional one. The first and third differences can be understood from the difference between the density, because the disk has higher density than the averaged density while the cavity has lower density. The second is not caused by the difference of density since, from equation (4.2), averaged density in this region is not so different from original one. This causes the existence of the disk, which efficiently absorbs the radiation from the central star. The radiation is only heating source of the dust particles so that shaded region loses the energy source to heat up the dust particles due to the efficient absorption of the disk.

Emergent SEDs from the two temperature distributions, shown in Figure 4.2, are illustrated in Figure 4.3. The SEDs are clearly different from semi- and full-two dimensional case in whole frequency range. Clearly from the radiative transfer equation (3.2), emergent flux depends on the source function of all grid points, which is determined from temperature of the dust T and mean intensity J_ν. In the lower frequency range $\nu < \nu_{\text{peak}} \sim 10^{12.5}$Hz, emergent flux in the semi-two dimensional case is larger than the full-two dimensional case. This is because that the semi-two dimensional temperature in the envelope and the disk is higher than the full-two dimensional case and flux in this frequency range is dominated by the thermal emission of the dust. On the other hand, in the higher frequency range $\nu > \nu_{\text{peak}}$, flux is very small in the semi-two dimensional case. In this frequency range, flux is dominated by the scattering light from the central star, evaluated by $\chi_\nu^{\text{sca}} J_\nu$. Thus, it seems to cause that J_ν in the semi-two dimensional case is underestimated particularly in the cavity region, which has low density and thus scattering light is seen through this area.

4.3 Effects of Each Parameter on Emergent SED

The effect of each parameter on the SED is very important, because, in practice, we must infer the physical value from the observed SED by using this dependence. Each parameter affects the SED with the characteristic frequency range according to the property of the parameter. But the characteristic frequency for these parameters are often duplicate each other, as shown in this section. Thus, to infer the accurate physical property from the SED, we must investigate the property of the SED against the parameters of the model in detail. In this section, we describe the results of the effect on the emergent SED of some primal parameters in our model.

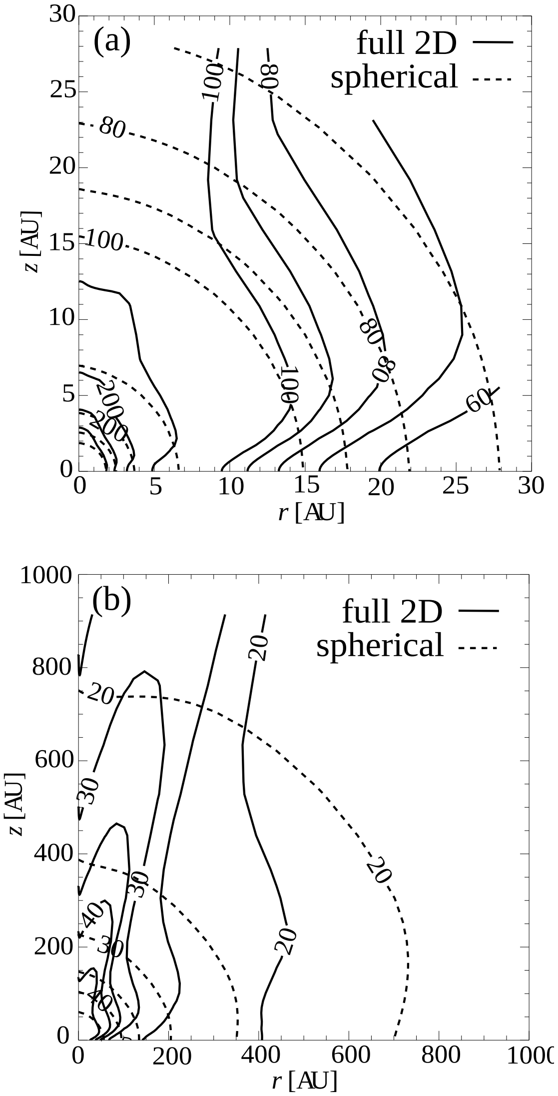

Figure 4.2: Temperature distributions obtained by the full two-dimensional radiative equilibrium calculation (solid curve) and the spherically averaged two-dimensional calculation (dotted curve) in regions (a) 30 AU × 30 AU and (b) 1000 AU × 1000 AU. Adopted parameters are $L_* = 1.0 L_\odot$, $\rho_1 = 10^{-13}$ g cm^{-3}, $\Sigma_1 = 2000$ g cm^{-2}, and $\theta_{\rm bp} = 25°$. In the spherically averaged calculation, density distribution is spherically averaged first, and then, the radiative equilibrium is solved with the two-dimensional spherically symmetric radiative transfer calculation. This figure is taken from Nakazato et al. (2003)

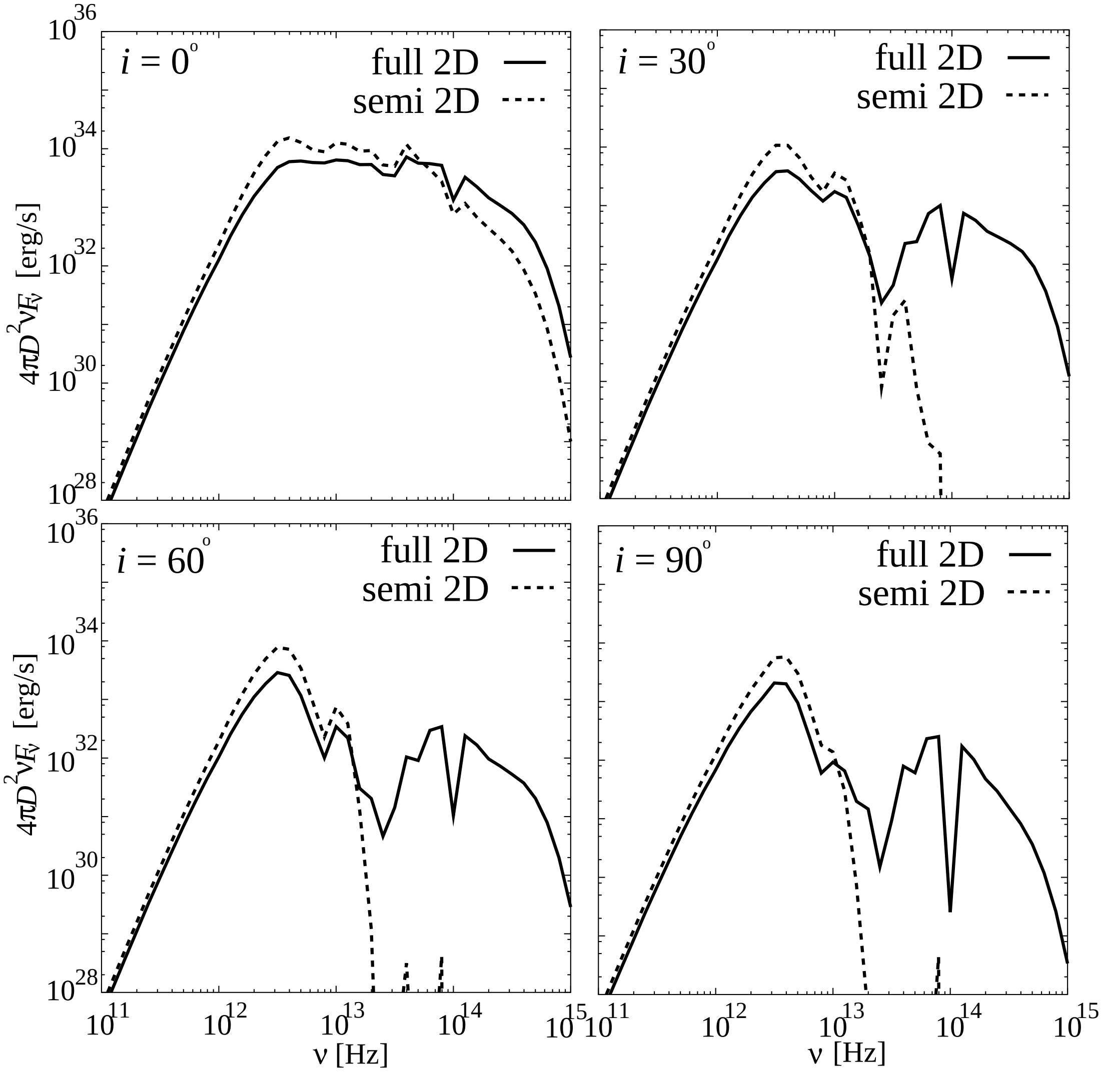

Figure 4.3: Spectral energy distributions based on temperature distributions obtained by two different methods shown in Fig. 3.23 for different inclination angles. SEDs from the non-spherical temperature distribution (obtained by the full two-dimensional radiative equilibrium calculation) are shown by solid curves, and those from the spherical temperature are shown by dotted curves. This figure is taken from Nakazato et al. (2003).

4.3.1 Luminosity of the Central Star L_*

The emergent SEDs with luminosities of the central star L_* from $0.1L_\odot$ to $10L_\odot$ are shown in Figure 4.4. Adopted parameters are $\rho_1 = 10^{-13}$ g cm^{-3}, $\Sigma_1 = 2000$ g cm^{-2}, and $\theta_{\rm bp} = 20°$, respectively. Luminosity of the central star is only energy source in our model. Thus, changes in L_* are directly reflected to the emergent luminosity $L_{\rm SED}$ calculated by

$$L_{\rm SED} = 4\pi D^2 \int_0^\infty \nu F_\nu d\log\nu. \tag{4.3}$$

Note that $L_{\rm SED}$ depends on the inclination i and is not equal to the luminosity of the central star L_* reflecting the asymmetry of the system. For example, in the case of $L_* = 1L_\odot$, emergent luminosities calculated from the SED are 5.7, 1.3, 0.83, and $0.56L_\odot$ for the inclination angle $i = 0°$, 30°, 60°, and 90°, respectively. Clearly, it is not correct that the emergent luminosity $L_{\rm SED}$ is regarded as the luminosity of the central star L_*. It is necessary to establish a method to determine the luminosity of the central star L_*.

We can also see from Figure 4.4 that a peak flux of the emergent SED $4\pi D^2(\nu F_\nu)_{\rm max} = (\nu L_\nu)_{\rm max}$ (near the frequency $\nu \sim 10^{12.5}$Hz) seems to be roughly proportional to the luminosity of the central star L_* for each inclination. Further, from Figure 4.1, an effect of the inclination i to the peak flux seems to be weak. Thus, there is possibility to determine the luminosity of the central star L_* from the emergent luminosity $L_{\rm SED}$ or the peak flux $(\nu L_\nu)_{\rm max}$.

4.3.2 Surface Density of the Disk Σ_1

Emergent SEDs when the surface density of the disk at 1AU changes from 200 g cm^{-2} to 20000 g cm^{-2} are illustrated in Figure 4.5. From equation (2.7), disk mass is proportional to Σ_1 so that we may regard Σ_1 as the indicator of the disk mass. $\Sigma_1 = 2000$ g cm^{-2} corresponds to the mass $M_{\rm disk} = 0.03M_\odot$. From Figure 4.5, an increase of Σ_1 (i.e. disk mass) leads to an increase of the flux in the range $\nu < \nu_{\rm peak}$ while the flux in the range $\nu > \nu_{\rm peak}$ seems to be independent of Σ_1. The behavior of lower frequency range causes that the flux at $\nu < \nu_{\rm peak}$ is dominated by the thermal radiation of the dust particles, and in this frequency range, the system is optically thin. Thus, the emergent

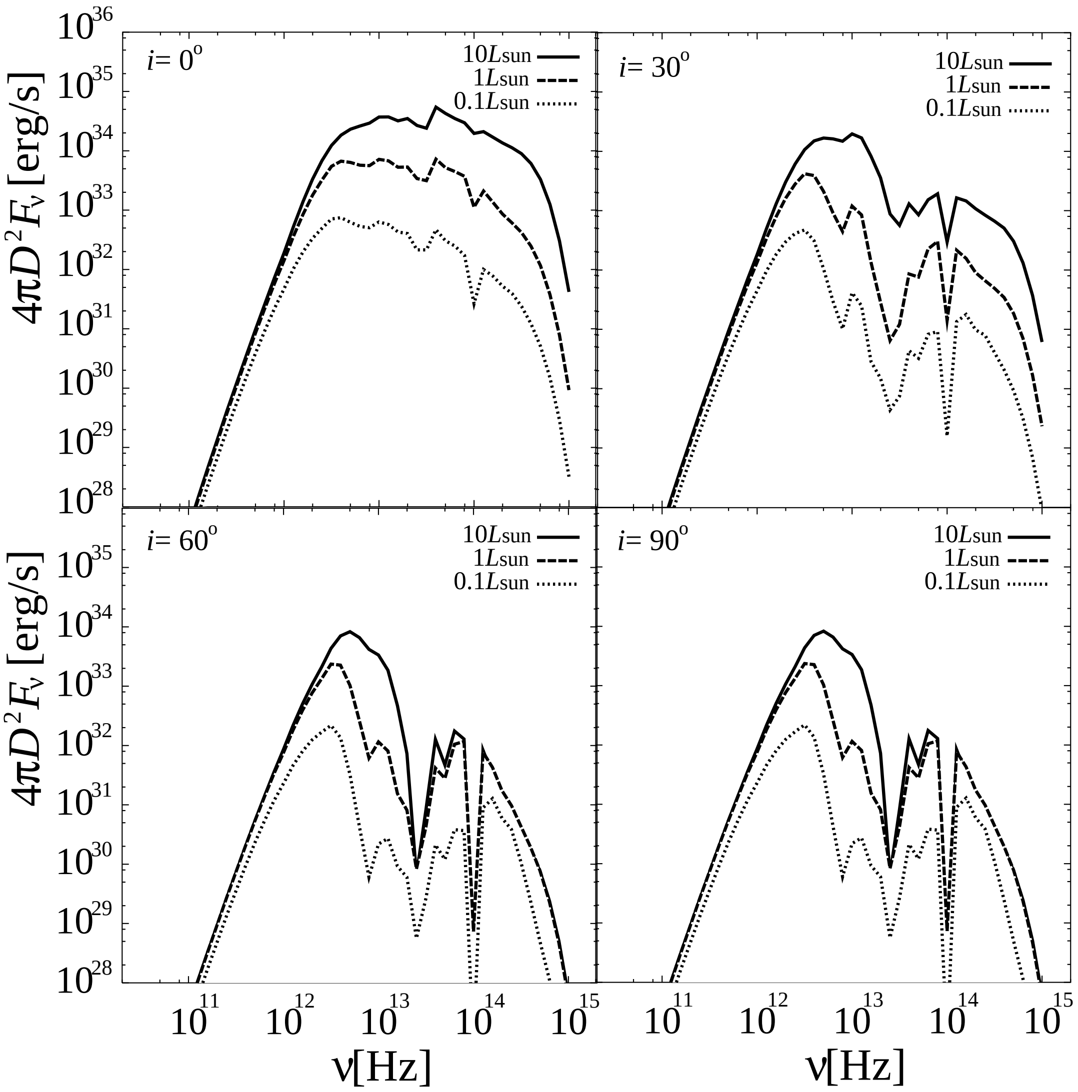

Figure 4.4: The dependence of the emergent SED against the luminosity of the central star L_*. Four panels show the results for the different inclination angle $i = 0°$ (top left), 30° (top right), 60° (bottom left), and 90° (bottom right). Three curves of each panel correspond to the results of the $10L_\odot$ (solid curve), $1L_\odot$ (dashed curve), and $L_* = 0.1L_\odot$ (dotted curve), respectively. Adopted parameters are $\rho_1 = 10^{-13}$ g cm^{-3}, $\Sigma_1 = 2000$ g cm^{-2}, and $\theta_{\rm bp} = 20°$.

flux is determined by the summation of the emission from whole spatial points,

$$\boldsymbol{F}_\nu \propto \int_V \kappa_\nu \rho(\boldsymbol{r}) B_\nu(T(\boldsymbol{r})) dV, \tag{4.4}$$

which is roughly proportional to the circumstellar mass $M_{\rm tot} = M_{\rm disk} + M_{\rm env}$.

On the other hand, at higher frequency range, contribution of thermal emission of the dust to the flux is negligible because, as seen in Figure 4.2, temperature of the dust is less than 100K except for the very near the center (black body radiation at 100K peaks at the frequency 10^{13}Hz) and system is optically thick in these frequency. Dominant component of this frequency range is thus scattered light originated from the central region since only possible source of these high energy radiation is central region or central star. In our model, disk is small compared with the envelope in the geometrical contribution to the scattering, although disk is geometrically thick by considering the hydrostatic vertical structure. Thus, disk structure does not affect the flux in the higher frequency range. As a result, possible candidate to estimate an information about the disk seems to be the flux at $\nu < \nu_{\rm peak}$.

4.3.3 Density of the Envelope ρ_1

The density at the 1AU in the envelope is also regarded as the indicator of the mass of envelope, similarly to Σ_1. $\rho_1 = 10^{-13}$ g cm^{-3} corresponds to the mass $M_{\rm env} = 0.03 M_\odot$. From Figure 4.6, the behavior in the lower frequency range of the emergent SEDs is almost same in the case of Σ_1, i.e. increase of ρ_1 leads to the increase of the flux of this frequency range. This is because that ρ_1 is also related to the circumstellar mass $M_{\rm tot}$. On the other hand, the envelope has a contribution to the scattering because it surrounds the central star-disk system, and optically thick to the higher frequency range. Thus, ρ_1 strongly affects the flux in the range $\nu < \nu_{\rm peak}$. When the envelope mass increases, a fraction absorbed by the dust particles is increasing and absorbed radiations are re-emitted at lower frequency. Hence, flux at higher frequency range decreases with increasing the envelope mass, in contrast to the lower frequency case.

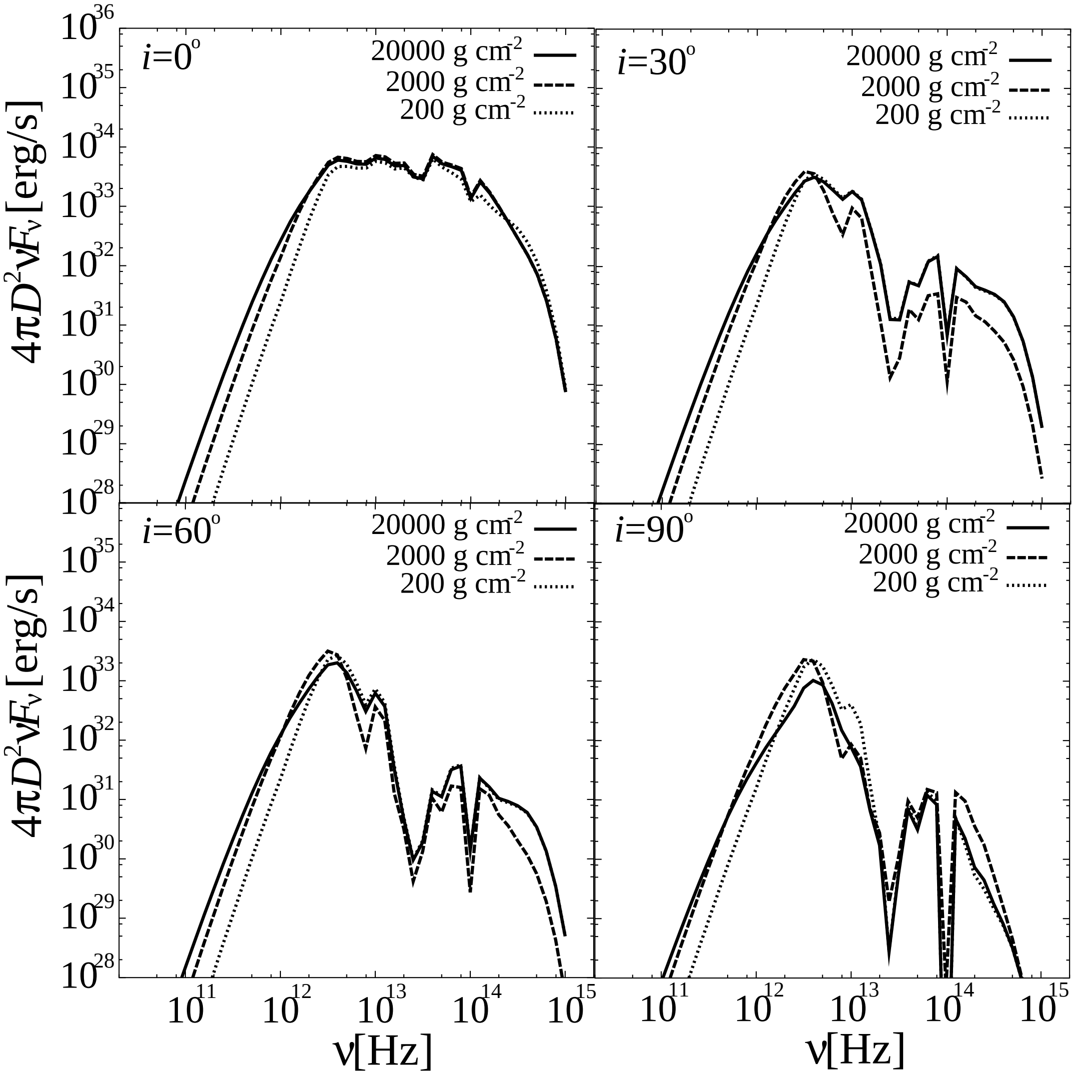

Figure 4.5: The dependence of the emergent SED against the surface density of the disk. Four panels show the results for the different inclination angle $i = 0°$ (top left), $30°$ (top right), $60°$ (bottom left), and $90°$ (bottom right). Three curves of each panel correspond to the results of the $\Sigma_1 = 20000$ g cm^{-2} (solid curve), $\Sigma_1 = 2000$ g cm^{-2} (dashed curve), and $\Sigma_1 = 200$ g cm^{-2} (dotted curve), respectively. Adopted parameters are $L_* = 1L_\odot$, $\rho_1 = 10^{-13}$ g cm^{-3}, and $\theta_{\rm bp} = 20°$.

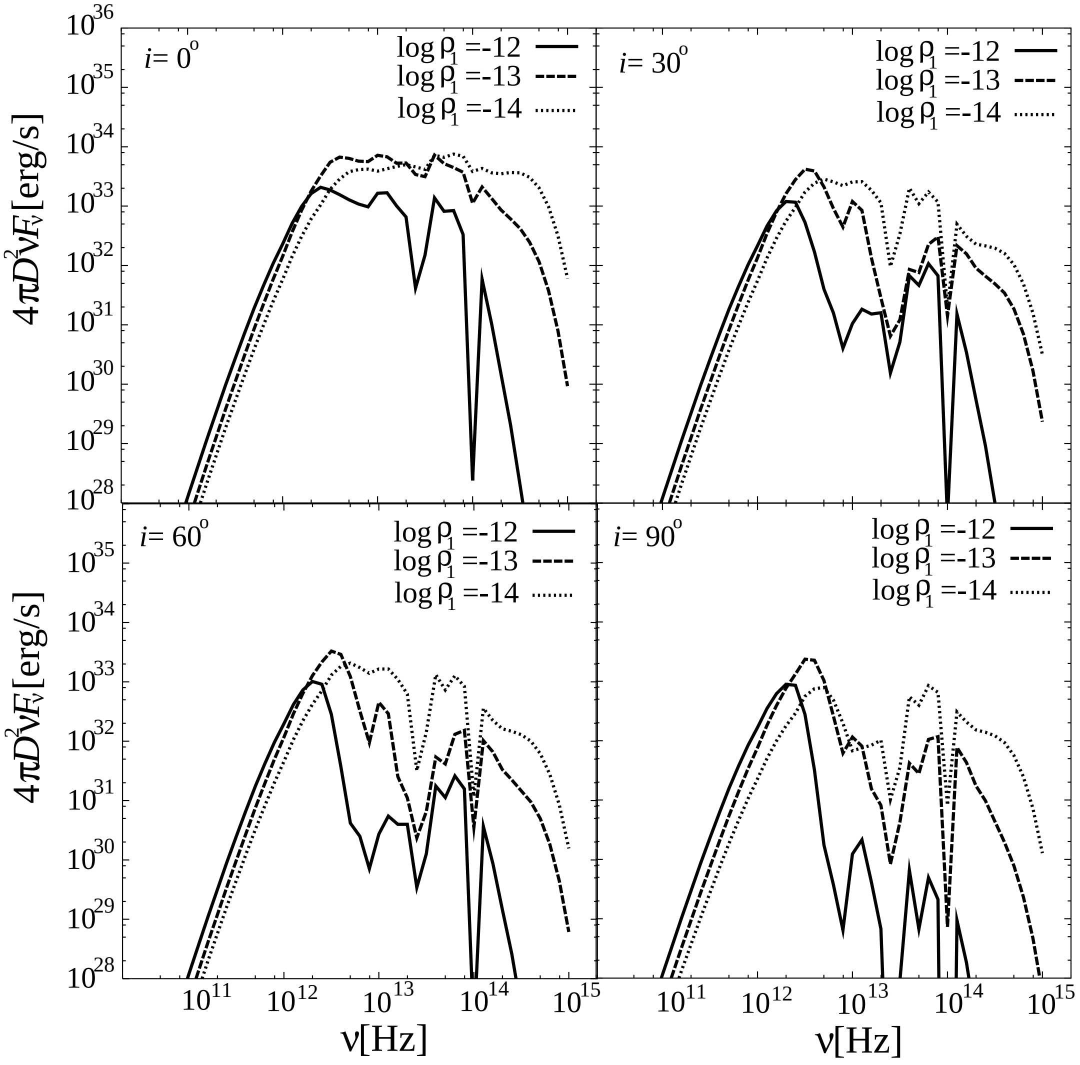

Figure 4.6: The dependence of the emergent SED against the density of the envelope. Four panels show the results for the different inclination angle $i = 0°$ (top left), $30°$ (top right), $60°$ (bottom left), and $90°$ (bottom right). Three curves of each panel correspond to the results of the $\rho_1 = 10^{-12}$ g cm^{-3} (solid curve), $\rho_1 = 10^{-13}$ g cm^{-3} (dashed curve), and $\rho_1 = 10^{-14}$ g cm^{-3} (dotted curve), respectively. Adopted parameters are $L_* = 1L_\odot$, $\Sigma_1 = 2000$ g cm^{-2}, and $\theta_{\rm bp} = 20°$.

4.3.4 Opening Angle of the Cavity $\theta_{\rm bp}$

The effect of an opening angle of outflow cavity is shown in Figure 4.7. Clearly, $\theta_{\rm bp}$ is an important parameter since degree of asymmetry of the circumstellar environment strongly depends on this parameter in our model. As shown in Figure 4.7, emergent SEDs are strongly dependent on the opening angle. If $\theta_{\rm bp}$ is large, scattered radiation is easy to escape through envelope, thus flux at higher frequency range is not reduced by the absorption of the dust in the envelope. This situation is same even if the inclination i is nearly edge-on. The radiation from the central region escapes to the cavity and is scattered into the edge-on direction at the 'wall' of the envelope, which is an edge of the cavity. The scattered radiation reaches to the observer although it passes through the optically thick envelope. This is because that the radiation only grazes the outer edge of the envelope. The envelope is totally optically thick (e.g. from center to the observer), but it cannot have efficient absorption in this case.

There are some characteristic properties in this case, not appeared in other parameter. First, emerging SED shows Class II like or 'flat-spectrum' feature if $\theta_{\rm bp}$ is large and $i < \theta_{\rm bp}$. Second, emergent SED shows double-peaked (at $\sim 10^{12.5}$Hz and $\sim 10^{14}$Hz) if $\theta_{\rm bp}$ is large and $i > \theta_{\rm bp}$. In either way, it seems that emergent SED is not classified to the Class I category when $\theta_{\rm bp}$ is large (e.g. $\theta_{\rm bp} > 40^\circ$). On the other hand, SED for $\theta_{\rm bp} = 0^\circ$ is also unsuitable for Class I objects, because many Class I SEDs have a flux in near-infrared range (around the frequency 10^{14}Hz). SEDs for $\theta_{\rm bp} = 0^\circ$ are rather classified to Class 0 qualitatively. But, it is unsuitable from the observational inspection, because Class 0 object has more powerful outflow than the Class I objects (Bontemps et al. 1996a; Andé et al. 2000; Visser et al. 2002), thus the cavity also exists in the Class 0 phase if cavity causes the outflow. Thus, we can make a constraint to the value of $\theta_{\rm bp}$ by the fact that the emergent SED must be classified to Class I object.

From Figure 4.7, it seems to restrict that $\theta_{\rm bp}$ is $10^\circ < \theta_{\rm bp} < 40^\circ$ to reproduce the Class I SED.

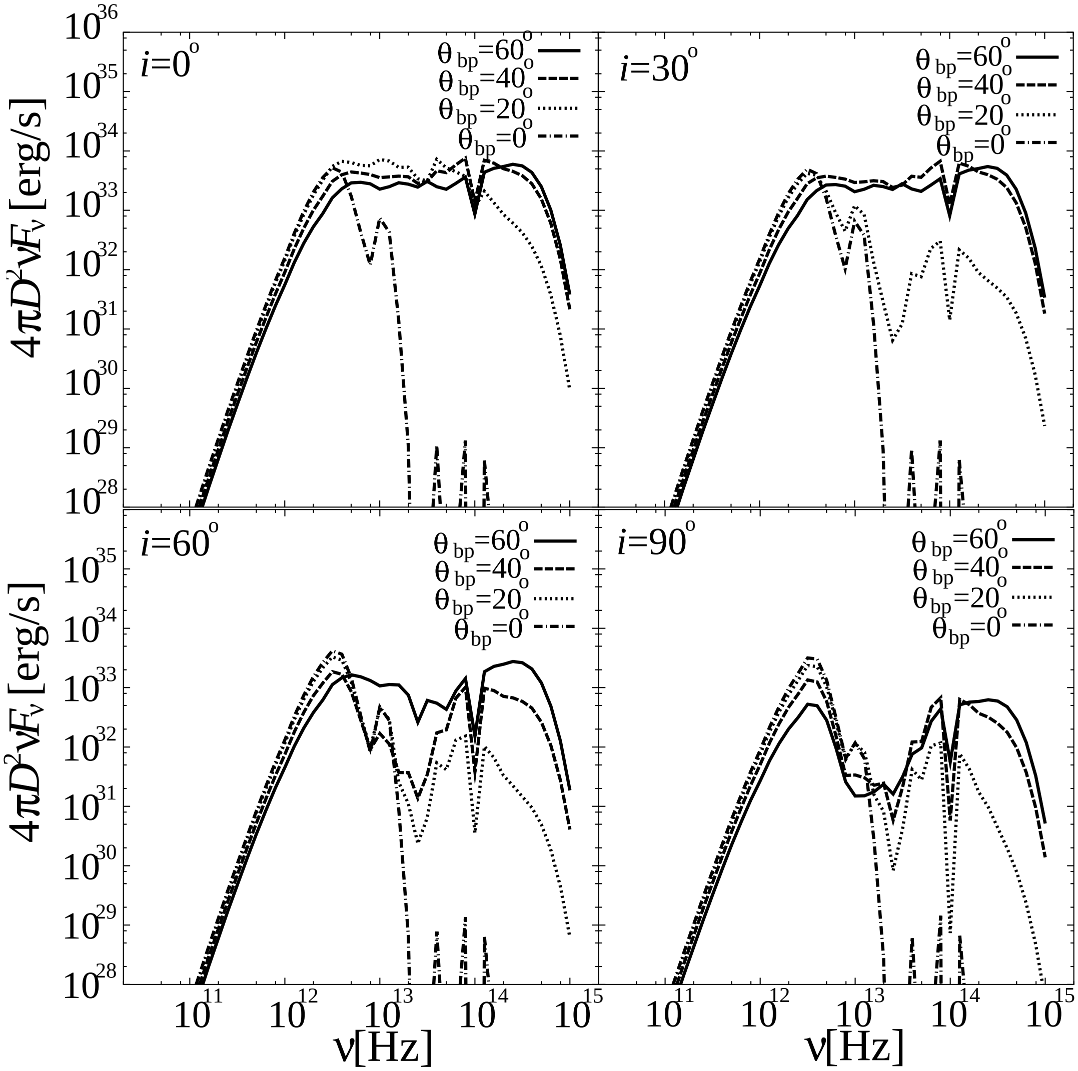

Figure 4.7: The dependence of the emergent SED against the opening angle of outflow cavity. Four panels show the results for the different inclination angle $i = 0°$ (top left), 30° (top right), 60° (bottom left), and 90° (bottom right). Four curves of each panel correspond to the results of the $\theta_{\rm bp} = 60°$ (solid curve), $\theta_{\rm bp} = 40°$ (dashed curve), $\theta_{\rm bp} = 20°$ (dotted curve), and $\theta_{\rm bp} = 0°$ (dot-dashed curve), respectively. Adopted parameters are $L_* = 1L_\odot$, $\rho_1 = 10^{-13}$ g cm^{-3}, $\Sigma_1 = 2000$ g cm^{-2}, and $\theta_{\rm bp} = 20°$.

4.3.5 Inclination Angle of the System i

Clearly seen from Figures 4.4-4.7, inclination angle of the system i strongly affects the emergent SEDs. As pointed out in section 4.1, the frequency $\nu_{\rm peak}$, at which the emergent SED has a maximum flux, corresponds to the frequency that optical depth of the system is nearly 1, and it is optically thick for the radiation having $\nu > \nu_{\rm peak}$ while optically thin for $\nu < \nu_{\rm peak}$. If the system is optically thin, radiation from this system is isotropic because it can escape directly from the system, and we assumed all the emission and scattering contribution are isotropic in our model. On the other hand, if the system is optically thick, radiation cannot escape from the envelope without experiencing any amount of extinction (absorption or scattering).

Since we assumed asymmetric density distribution like a disk or a cavity, the number of times of extinction is dependent on the direction, i.e. radiation to the disk is extincted larger number of times than that to the cavity. The extinction causes the anisotropic distribution of the radiation from the system because extinction process forces to lose the radiation from a certain direction, and re-emission or scattering redistributes this radiation isotropically. As a result, radiation reached to the edge-on direction (direction to the disk) is less than the pole-on direction (direction to the cavity), if the system is optically thick. Thus, $\nu_{\rm perk}$ also corresponds to the boundary of the isotropic and anisotropic frequency regions in the emergent SED. This situation is seen from Figure 4.1.

4.4 Method to Infer the Parameters from SED

In this section, we try to establish the procedure to infer the physical property of the protostar from its SED based on the results of section 4.3. Here, we divide the SED to the three regions: region 1, frequency range $\nu < \nu_{\rm peak}$, region 2, frequency at $\nu_{\rm peak}$, and region 3, frequency range $\nu > \nu_{\rm peak}$. This division corresponds to the optical depth τ. The optical depth of the system is $\tau < 1$ for region 1, $\tau \sim 1$ for region 2, and $\tau > 1$ for region 3.

From section 4.3, we know the effects of physical parameters to these regions. First, the luminosity of the central star L_* affects all regions in the sense that flux increases with larger L_*. Next, the surface density of the disk Σ_1 (mass of the disk) affects only region 1 in the sense similar to L_*. In contrast, the density of the envelope ρ_1 (mass of the envelope) affects the regions 1 and 3, in the sense that flux increases for region 1 and decreases for region 3 with increasing ρ_1. The opening angle of cavity also affects regions 1 and 3 but the trend of the dependence is contrary to ρ_1. Finally, the inclination angle of the system i affects region 3 in the sense similar to ρ_1 in this region. We can see from above that the effects of each parameter to the emergent SED strongly degenerate each other. Thus, we need to establish the procedure to infer the physical property of the protostar, which can disentangle this degeneracy.

Parameter degeneration is very complicated. Thus, if one can restrict any parameter by any constraint, we adopt this value anyway to reduce the degree of degeneracy. At first, we set the opening angle of the cavity is in the range $10^\circ < \theta_{\rm bp} < 40^\circ$. The opening angle of cavity is observationally estimated from the molecular line study (e.g. CO). One can estimate the opening angle $\theta_{\rm bp}$ from the feature of the outflow lobe assuming it has a conical shape (Cabrit & Bertout 1986). Several works tried to estimate the opening angle $\theta_{\rm bp}$ of Class I objects according to this assumption (e.g. TMC1 and TMC1A, Chandler et al. 1996; L1448, Bachiller et al. 1995; B335, Hirano et al. 1988; Chandler & Sargent 1993; L1551 IRS5, André et al. 1990). From these results, our constraint for $\theta_{\rm bp}$ is roughly consistent with the observation. And if $\theta_{\rm bp}$ is inferred from the above observation, we may assume that value. But, we should note that the above estimation is not always consistent with our parameter $\theta_{\rm bp}$ since these observations measured larger scale structure than the scale considered here.

The density of the envelope ρ_1 and surface density of the disk Σ_1 have a same effect to the region 1, and ρ_1 affects the region 3 while Σ_1 does not. Thus, we can estimate total effect of these parameters from region 1, and separate effects of these parameters by the effect of region 3. But, to take the above estimation, we must determine the inclination angle i and the luminosity L_* since they also affect the regions 1 and 3. Thus, it seems to be appropriate to adopt the following procedure to solve the degeneracy:

1. Restrict the opening angle $\theta_{\rm bp}$ from the observation. Or set $10^\circ < \theta_{\rm bp} < 40^\circ$, which is given by our simulation.

2. Infer the inclination angle i.

3. Infer the luminosity of the central star L_*.
4. Infer the total effect of the density of the envelope ρ_1 and the surface density of the disk Σ_1.
5. Separate ρ_1 and Σ_1.

Here, we will discuss the method to estimate each parameter.

4.4.1 Inclination Indicator $f_{\rm L}$

The inclination angle i only affects the flux in the frequency range where the system becomes optically thick, i.e., region 3. Thus, the emergent luminosity $L_{\rm SED}$ changes with the inclination angle of the object, while the peak flux of the SED, $(\nu L_\nu)_{\rm max}$, is not influenced by the inclination. We noticed this property and defined $f_{\rm L}$, which is a ratio of $L_{\rm SED}$ to $(\nu L_\nu)_{\rm max}$,

$$f_{\rm L} = \frac{L_{\rm SED}}{(\nu L_\nu)_{\rm max}}. \tag{4.5}$$

We call this quantity $f_{\rm L}$ the inclination indicator because of the reason described below. The dependence of the indicator $f_{\rm L}$ against the inclination i is displayed in Figure 4.8. In Figure 4.8, we also showed the emergent luminosity $L_{\rm SED}$ and the peak flux of the SED $(\nu L_\nu)_{\rm max}$ as a function of the inclination angle i. Note that $f_{\rm L}$ consists of only the observables estimated from SED, so we can evaluate $f_{\rm L}$ when SED is given. We proposed that the observable $f_{\rm L}$ is good indicator of the inclination angle i (Nakazato et al. 2003).

As seen in Figure 4.8, the indicator $f_{\rm L}$ is strongly dependent on the inclination angle i in the range $\theta_{\rm bp} - 10° < i < \theta_{\rm bp} + 10°$. This is caused by a fact that the column density from the center to the observer dramatically changes across the angle $\theta_{\rm bp}$. In region 3, total amount of the emergent flux at a certain inclination angle is strongly dependent on the angular distribution of the optical depth τ, i.e. column density, since the system is optically thick in this frequency range, so the radiation tends to go into the direction which has smaller column density. According to the equation (2.9), the column density seen from the cavity is 100 times smaller than the column density seen from the envelope. Thus, the large amount of the radiation in region 3 escapes through

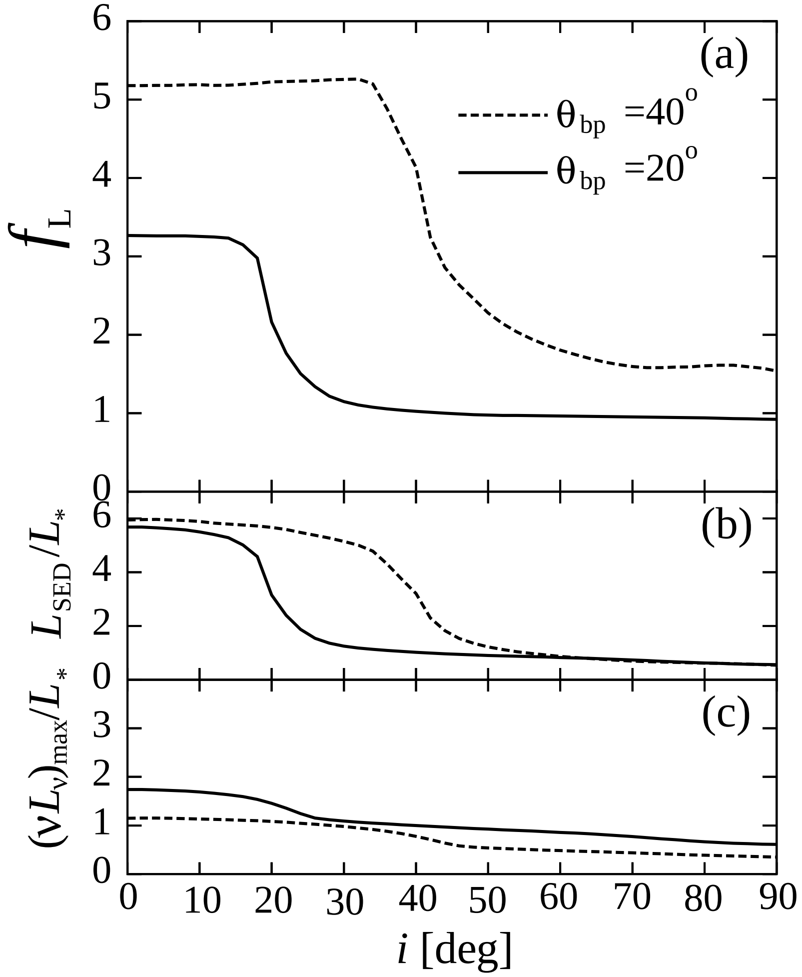

Figure 4.8: Three observables obtained directly from SED are plotted against the inclination. In each panel, two different curves correspond to SEDs with different opening angles in the outflow region, $\theta_{\rm bp} = 20^\circ$ (solid curve), and 40° (dotted curve), respectively: (a) the observable inclination indicator $f_{\rm L}$, which is the ratio of $L_{\rm SED}$ to $(\nu L_\nu)_{\rm max}$, (b) the emergent luminosity $L_{\rm SED}$, and (c) the peak flux $(\nu L_\nu)_{\rm max}$. It is seen that $f_{\rm L}$ changes abruptly around $i = \theta_{\rm bp}$. If $f_{\rm L}$ is obtained from the SED, the inclination i can be estimated for $i \geq \theta_{\rm bp}$ by using this figure. This figure is taken from Nakazato et al. (2003)

the cavity. As a result, f_{L} strongly depends on the inclination angle i around the angle of the cavity θ_{bp}. On the contrary, f_{L} is flat in the range $i \sim 0^\circ$ and $i \sim 90^\circ$. This is also caused by the angular distribution of the column density. In the range $i \sim 0^\circ$, column density is almost constant because of the density distribution of the cavity (cf. equation 2.9). It is also constant in the range $i \sim 90^\circ$ because of the existence of the circumstellar disk.

We would note that the maximum value of the f_{L} depends on the opening angle of the cavity θ_{bp}. Thus, in principle, we can restrict θ_{bp} by the value of the f_{L} in addition to the constraint from the shape of the SED. From Figure 4.8, when we evaluate f_{L} from the emergent SED, it has an error due to the influence of the other parameters. The error due to the θ_{bp}, estimated from the Figure 4.8 is roughly $\pm 10^\circ$. In section 4.3.4, we pointed out that the opening angle θ_{bp} can be estimated from the mapping of the outflow lobe using molecular line emission (e.g. CO). Thus, we can reduce this uncertainty when θ_{bp} of a target object is estimated from these observations.

We need to estimate the errors due to another parameters, i.e. L_*, ρ_1, and Σ_1. In Figures 4.9-4.11, we showed changes of f_{L} when these parameters are varied. We can see from these figures that the errors due to these parameters are small in the range $\theta_{\mathrm{bp}} - 10^\circ < i < \theta_{\mathrm{bp}} + 10^\circ$. The influences in the other inclination range are neglected because, in these region, an accuracy of the inclination angle estimation using f_{L} is not high enough.

Clearly seen from Figure 4.9, luminosity of the central star L_* does not affect the indicator f_{L} so strong, though it strongly affects the emergent SEDs (see Figure 4.4). This is because that f_{L} could be understood as an emergent luminosity normalized by the peak flux. The peak flux $(\nu L_\nu)_{\mathrm{max}}$ is roughly proportional to the luminosity of the central star L_*, although the effect of the inclination and opening angle are still remained (see section 4.4.2). We found from Figure 4.4 that the emergent SEDs seem to change the flux keeping the whole shape by varying L_*. Thus, we expect that the luminosity of the emergent SED has a similar value when we divide it by the appropriate normalizing factor, which is proportional to the luminosity of the central star. The observable f_{L} has just a form we expected, i.e., emergent luminosity normalized by the peak flux which is roughly proportional to the luminosity of the central star L_*. According to the above property, $f_{\rm L}$ does not depend strongly on the luminosity of the central star L_*.

The envelope density ρ_1 affects the observable $f_{\rm L}$ (see Figure 4.10), since ρ_1 is the important variable determining the optical depth of the system. The optical depth from the center to the observer, $\tau_{\rm c}$, is proportional to the parameter ρ_1 except for the contribution of the disk. Thus, small value of ρ_1 corresponds to the case when $\tau_{\rm c}$ is small (but larger than 1), while large ρ_1 corresponds to the case $\tau_{\rm c}$ is large. In region 3, ρ_1 has negative correlation with emergent flux, i.e., emergent flux decreases with increasing ρ_1. Thus, the emergent luminosity is decreasing with an increase of ρ_1, although in region 1 changes with ρ_1 have positive correlation. As pointed out in the case of luminosity, $f_{\rm L}$ can be regarded as a normalized emergent luminosity, so we expect that $f_{\rm L}$ has the dependence similar to the emergent luminosity. In spite of these influences of ρ_1, inclination angle estimated from $f_{\rm L}$ is not so affected in the range where $f_{\rm L}$ dramatically changes.

From Figure 4.11, the surface density of the disk Σ_1 does not affect $f_{\rm L}$ since the disk is geometrically small compared with the envelope.

As a result, errors due to the above three parameters are roughly estimated at $\pm 5^\circ$ in the inclination. Thus, total error in addition to the effect of the opening angle is estimated at $\pm 15^\circ$ if $\theta_{\rm bp}$ is unknown, i.e., we set $10^\circ < \theta_{\rm bp} < 40^\circ$, while it is estimated at $\pm 5^\circ$ if $\theta_{\rm bp}$ is known.

4.4.2 Luminosity Indicator $(\nu L_\nu)_{\rm max}$

We noticed that the emergent luminosity changes homologously with varying the luminosity of the central star L_*. Especially, the peak flux of the SED, $(\nu L_\nu)_{\rm max}$, seems to be proportional to L_* (see Figure 4.4). We expressed the dependence of the peak flux $(\nu L_\nu)_{\rm max}$ against each parameter by the power law based on Figures 4.4-4.7, and obtained the following fitting formula,

$$(\nu L_\nu)_{\rm max} \simeq 5.2\times 10^{33}[{\rm ergs^{-1}}] \left(\frac{L_*}{L_\odot}\right)^{0.97} \left(\frac{\rho_1}{10^{-13}[{\rm gcm^{-3}}]}\right)^{0.13} \left(\frac{\Sigma_1}{2000[{\rm gcm^{-2}}]}\right)^{-0.047} f(\theta_{\rm bp}, i), \tag{4.6}$$

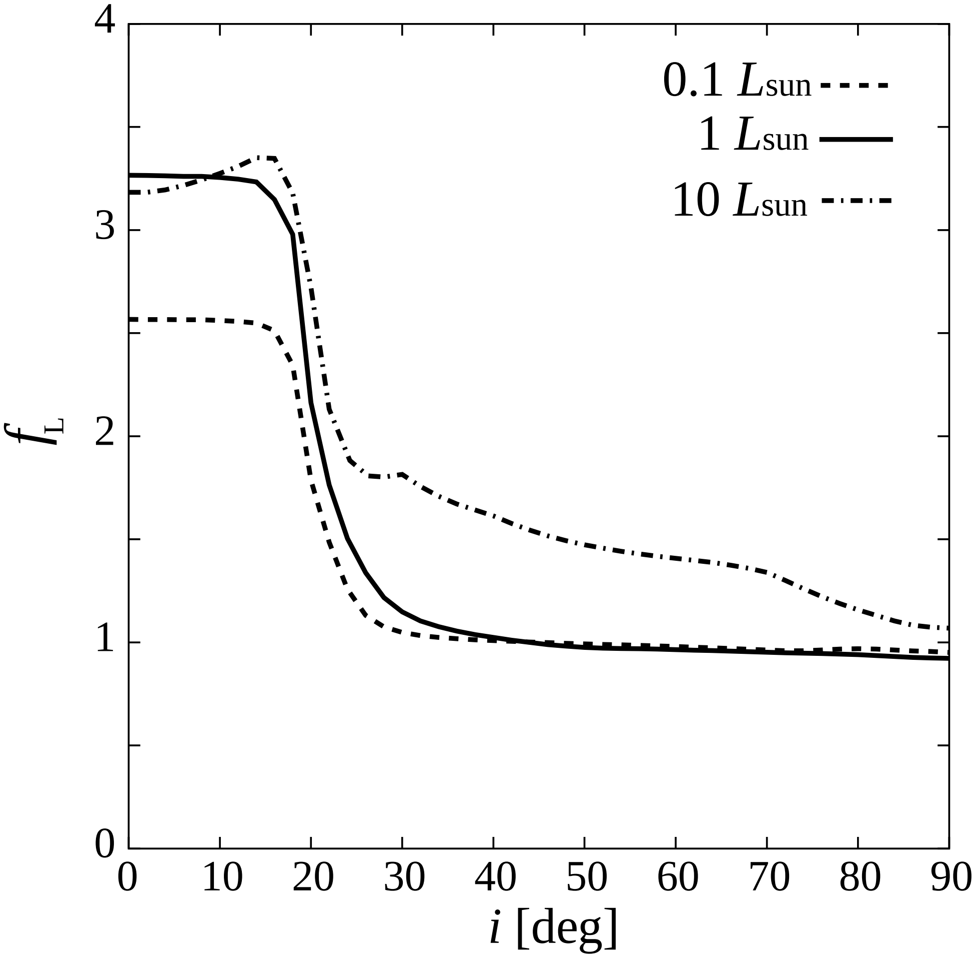

Figure 4.9: The inclination indicator, $f_{\rm L}$, vs the inclination, i, with three different luminosities. When the luminosity is low, $f_{\rm L}$ for the small inclination is reduced, while if the luminosity is high, $f_{\rm L}$ for large inclination is raised. Adopted parameters are $\rho_1 = 10^{-13}$ g cm^{-3}, $\Sigma_1 = 2000$ g cm^{-2}, and $\theta_{\rm bp} = 20°$.

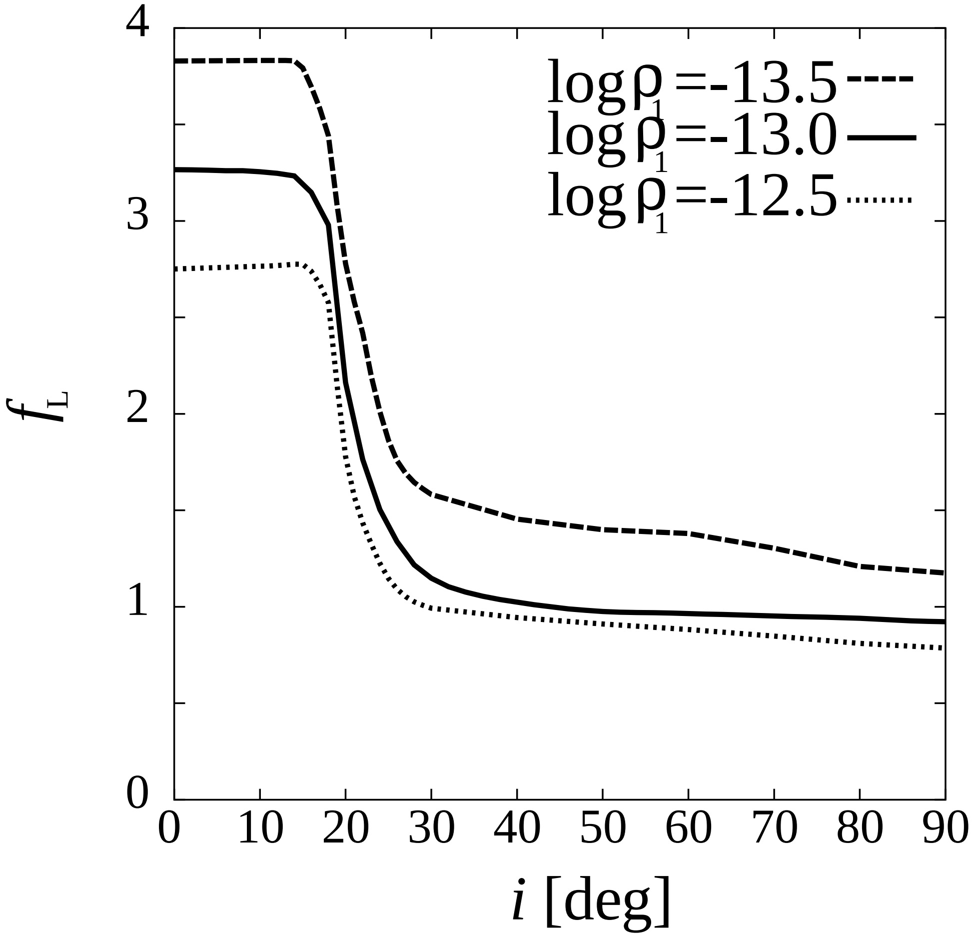

Figure 4.10: The inclination indicator, $f_{\rm L}$, vs the inclination, i, with three different envelope parameter ρ_1. The envelope does not affect the ratio $f_{\rm L}$ significantly. Adopted parameters are $L_* = 1L_\odot$, $\Sigma_1 = 2000$ g cm^{-2}, and $\theta_{\rm bp} = 20°$.

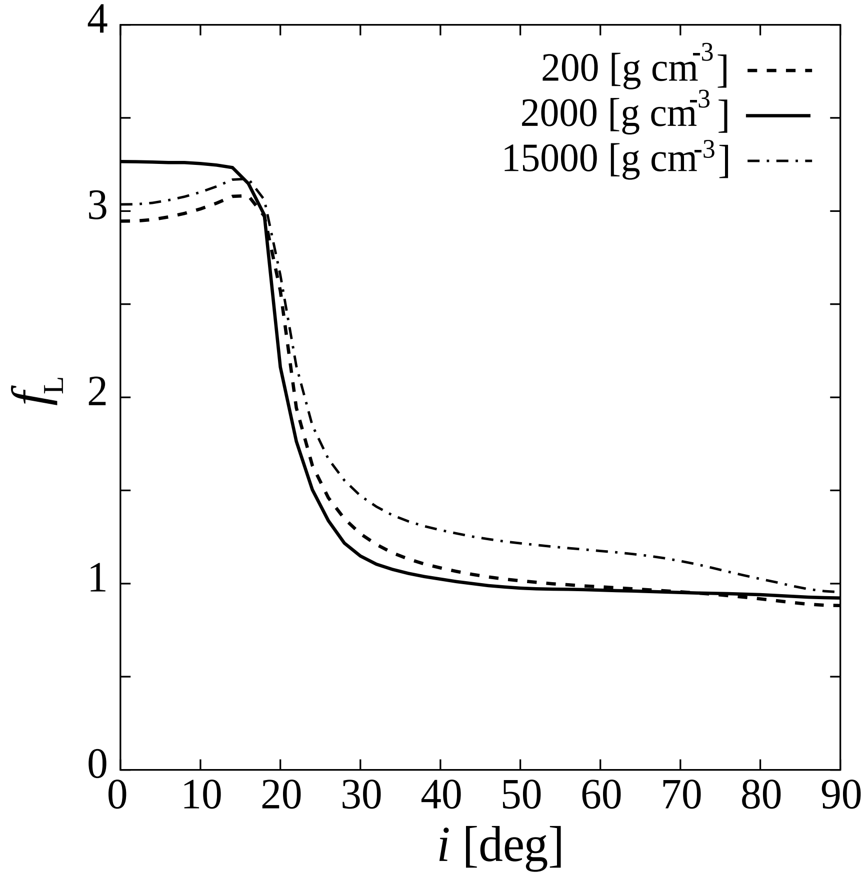

Figure 4.11: The inclination indicator, $f_{\rm L}$, vs the inclination, i, with three different disk parameter Σ_1. The disk does not affect the ratio $f_{\rm L}$ significantly. Adopted parameters are $L_* = 1L_\odot$, $\rho_1 = 10^{-13}$ g cm^{-3}, and $\theta_{\rm bp} = 20°$.

where $f(\theta_{\rm bp}, i)$ shows a contribution of the opening angle and inclination angle, and given by

$$f(\theta_{\rm bp}, i) = \begin{cases} \left(\dfrac{\cos i}{\cos 30^\circ}\right)^{2.0} \left(\dfrac{\cos \theta_{\rm bp}}{\cos 20^\circ}\right)^{0.28} & \text{if } i < \theta_{\rm bp}, \\ \left(\dfrac{\cos i}{\cos 30^\circ}\right)^{0.25} \left(\dfrac{\cos \theta_{\rm bp}}{\cos 20^\circ}\right)^{-0.15} & \text{if } i > \theta_{\rm bp}, \end{cases} \tag{4.7}$$

where $i > \theta_{\rm bp}$ is the case when we observed through the envelope, while $i < \theta_{\rm bp}$ is the case when we observed through the cavity. From equations (4.6) and (4.7), the peak flux is almost independent of the parameters ρ_1, Σ_1, and $\theta_{\rm bp}$. Further, when inclination angle i is larger than the opening angle $\theta_{\rm bp}$, peak flux is also independent of the opening angle. Thus, we neglected the influences of these parameters and obtained the simplified fitting formula,

$$(\nu L_\nu)_{\rm max} \simeq 5.2 \times 10^{33} [{\rm ergs}^{-1}] \left(\frac{L_*}{1 L_\odot}\right)^{0.97} f(i), \tag{4.8}$$

where $f(i)$ has the form

$$f(i) = \begin{cases} \left(\dfrac{\cos i}{\cos 30^\circ}\right)^{2.0} & \text{if } i < \theta_{\rm bp}, \\ 1 & \text{if } i > \theta_{\rm bp}. \end{cases} \tag{4.9}$$

We can obtain a formula to infer the luminosity of the central star L_* from the emergent SED by solving equation (4.8) with respect to L_*,

$$L_* \simeq 0.72 (\nu L_\nu)_{\rm max} f^{-1}(i), \tag{4.10}$$

where $f^{-1}(i)$ is an inverse of equation (4.9). We can infer the luminosity L_* from equation (4.10) because inclination angle i is known from the value of $f_{\rm L}$ and $\theta_{\rm bp}$ is also known or restricted within a certain range.

Note that equation (4.10) is an approximate formula since there is some approximations and assumptions to derive this formula. For example, we first assumed that the influences of the parameters are always written in the form of single power law, and we next neglected the effects of the parameters having small power law index. So far, the luminosity estimated from the equation (4.10) is the candidate of the true value of L_*.

The dependence of the $(\nu L_\nu)_{\rm max}$ in equation (4.10) is derived by the following simple discussion. Here, we assumed that the protostar is an isothermal system with temperature T, and it is optically thin for the radiation at the peak frequency. The former assumption is indeed unsuitable, but the later assumption is not so wrong because the peak frequency corresponds to where the optical depth from the center to the observer becomes roughly 1. We also assumed that opacity κ is independent of the frequency for simplicity. Under these assumptions, the luminosity of the central star L_* is written by

$$L_* = 4\pi R_{\mathrm{env}}^2 \kappa M_{\mathrm{tot}} \sigma T^4, \tag{4.11}$$

where R_{env} is the outer radius of the envelope and M_{tot} is the total mass of the disk and envelope. The peak flux is written in the form

$$(\nu L_\nu)_{\mathrm{max}} = 4\pi^2 R_{\mathrm{env}}^2 \kappa M_{\mathrm{tot}} \frac{2h\nu_{\mathrm{peak}}^4/c^2}{\exp(h\nu_{\mathrm{peak}}/kT) - 1}, \tag{4.12}$$

where ν_{peak} is the frequency where the Planck function has a maximum value in this temperature, and h is Planck constant. The peak frequency ν_{peak} is obtained by the Wien's displacement law,

$$\frac{\nu_{\mathrm{peak}}}{T} = 5.88 \times 10^{10}\ \mathrm{Hz\ K^{-1}}. \tag{4.13}$$

The denominator of the right hand side of the equation (4.12) is constant because of equation (4.13). From equations (4.11), (4.12), and (4.13), we obtain a relation between the luminosity of the central star and the peak flux,

$$L_* \propto (\nu L_\nu)_{\mathrm{max}}. \tag{4.14}$$

Thus, L_* is roughly proportional to the peak flux $(\nu L_\nu)_{\mathrm{max}}$.

4.4.3 Method to Infer the Masses of the Disk and the Envelope

We can then estimate the ρ_1 and Σ_1 from the SED because the effects of the other parameters are removed by estimating the inclination from f_{L} and the luminosity of the central star from $(\nu L_\nu)_{\mathrm{max}}$ and constraining θ_{bp} as described in previous sections. First, we can infer the total mass of the disk and the envelope from the flux in region 1, since, in this region, flux is dominated by the thermal radiation from the dust grains and system is optically thin against that radiation. Second, we can infer the mass ratio of the disk to the envelope from the flux in the region 3 because, in region 3, ρ_1 is the important parameter to determine the flux while Σ_1 does not affect the flux in this region. Thus, if we restrict the total mass M_{tot} from the flux in the region 1, we can vary the flux in the region 3 by changing the mass ratio of the disk to the envelope and adjust the simulated SED to the observed flux. Thus, we can infer the mass of the disk and envelope, i.e. Σ_1 and ρ_1, from the shape of region 1 and 3, in principle. But, it is still complicated because of the frequency dependence of the opacity (cf. Figure 2.2), so the fitting formula similar to the case for estimation of L_* cannot establish. But it is possible to infer ρ_1 and Σ_1 by comparing the observed SED with various simulated SEDs in the restriction of the other parameters.

Note that we can infer the value ρ_1 and Σ_1 even when the emergent SED has no spatial information about the target object since the flux is given by the equation (3.45). At first sight, it seems completely unknown whether the dust is located in the envelope or the disk. But, SED has spatial information of the optical depth of the system, which changes whether the dust belongs to the disk or the envelope. Hence, we can infer the spatial information about the dust from that property.

Chapter 5

Applications to Observations

In section 4.3, we established the method to infer the structure of the Class I objects from their SED. In this chapter, we apply this method to observations and infer the structure of the objects. We also discuss the evolutionary state of the objects based on the structure of the objects inferred from the spectral fitting. We pick out the Class I object IRAS 04365+2535 (hereafter, TMC1A) and the Class 0 object VLA 1623 as a sample. TMC1A is an infrared source discovered by the IRAS satellite. On the other hand, VLA1623 was not detected by the IRAS. It is detected first as a continuum radio source observed by the VLA. It has very cold SED which has a peak flux in a submillimeter range and is proposed as prototype of a Class 0 category by André et al. (1993).

5.1 IRAS04365+2535 (TMC1A)

TMC1A is a Class I object in L1534 cloud. Its circumstellar environment was examined by Motte & André (2001), who carried out a millimeter continuum mapping survey and investigated the circumstellar structure for many low mass protostars. According to their results, TMC1A has a circumstellar mass $M_{\rm tot} \sim 0.25 M_\odot$ inside a radius 4200AU. TMC1A is associated with the dense $\rm NH_3$ core (Benson & Myers 1989) and bipolar molecular outflow (Terebey et al. 1989). Chandler et al. (1996) observed it using the CO emission line mapping and estimated the half-opening angle $\theta_{\rm bp} = 15° - 21°$

and inclination angle $i = 40^\circ - 68^\circ$, assuming that it has a conical shape. They also estimated the dynamical timescale $t_{\rm dyn}$ of the bipolar outflow from its size and velocity, and obtained $t_{\rm dyn} = 840$yr for redshifted outflow lobe and $t_{\rm dyn} = 3700$yr for blueshifted lobe, which are both very young compared with the typical age of the Class I objects ($\sim 10^5$yr). Further, Tamura et al. (1991) suggested that TMC1A is associated with near-infrared nebulosity, which indicates the existence of a bipolar cavity. Kenyon et al. (1993) carried out the spectral modeling to this object and obtained that the luminosity of the central star $L_* = 2.23 L_\odot$, density at 1AU $\rho_1 = 10^{-13}$ g cm^{-13}, centrifugal radius $R_{\rm c} = 300$AU, which roughly corresponds to the radius of the disk, and inclination angle $i = 60^\circ$.

The emergent SED of TMC1A is shown in Figure 5.1. Flux data are taken from Chandler, Barsony, & Moore (1998) and Kenyon et al. (1993). We rewrite flux F_ν into $4\pi D^2 \nu F_\nu = \nu L_\nu$ assuming the distance to the object $D = 140$pc and construct SED. We first evaluate the emergent luminosity $L_{\rm SED}$ from Figure 5.1. We interpolated the data points with straight line in Figure 5.1 and extrapolated these lines to the frequency region which has no data points. We obtained the value $L_{\rm SED} = 2.8 L_\odot$ by the above procedure. This value is slightly higher than the value estimated by Myers et al. (1987), who estimated $L_{\rm SED} = 2.4 L_\odot$, and Kenyon & Hartmann (1995), $L_{\rm SED} = 2.2 L_\odot$, but almost consistent with these results. The peak flux of the SED is assumed to be the maximum of the observed data points, which is $(\nu L_\nu)_{\rm max} = 4.28 \times 10^{33}$ erg s^{-1} at frequency 5×10^{12}Hz. The inclination indicator $f_{\rm L}$ (see equation 4.5) is then 2.52. From Figure 4.8, this value indicates the inclination angle $i \sim 20^\circ$ when we set the opening angle $\theta_{\rm bp} = 20^\circ$. The peak flux of the SED indicates the luminosity of the central star $L_* \sim 0.8 L_\odot$ (equation 4.10). We fitted the SED of TMC1A based on the estimation using $f_{\rm L}$ and $(\nu L_\nu)_{\rm max}$, and finally obtained the best fitted SED (Figure 5.2). Adopted parameters are listed in table 5.1. Table 5.1 also lists the results by Kenyon et al. (1993) and Chandler et al. (1998).

Kenyon et al. used the semi-two dimensional protostar model to derive the physical property of Class I objects. They adopted a slowly rotating singular isothermal sphere model (Terebey et al. 1984), which is axially symmetric, to the envelope density distribution. Thus, emergent SEDs calculated by their model depend on the inclination

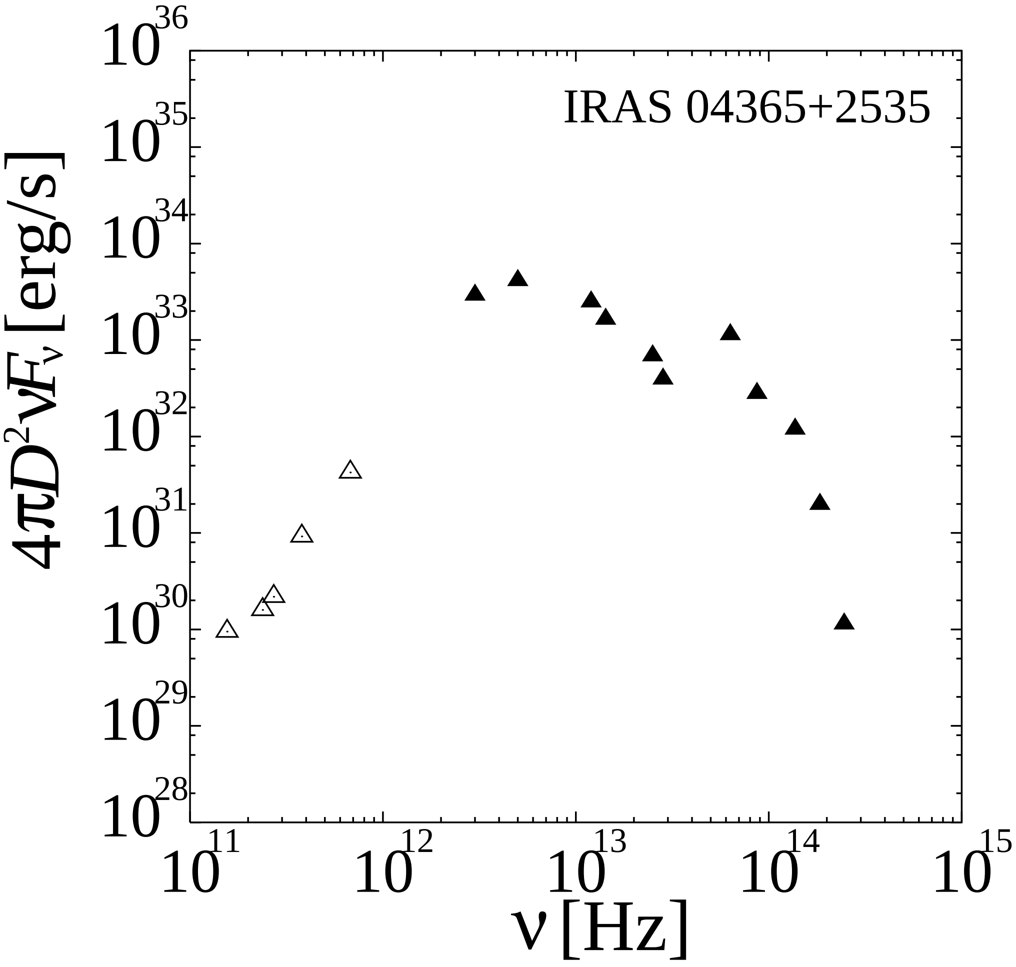

Figure 5.1: Emergent SED of a Class I object TMC1A (IRAS04365+2535). Plotted data were taken from Kenyon et al. (1993; filled square) and Chandler et al. (1998; open square), and assumed that a distance to the object D is 140pc.

Physical Properties of TMC1A Derived from SED

Ref.	L_* [$L_\odot$]	ρ_1 [g cm^{-3}]	$M_{\rm env}$ [$M_\odot$]	Σ_1 [g cm^{-2}]	$M_{\rm disk}$ [$M_\odot$]	$\theta_{\rm bp}$	i
This work	1.0	$10^{-12.5}$	0.13	10^4	0.1	20°	22°
KCH	2.24	10^{-13}	—	—	—	—	60°
CBM	1.90	—	0.027	—	—	—	—

Table 5.1: Best fitted parameters for TMC1A. The first row marked 'This work' is best fitted parameters of our protostar model. The second row marked 'KCH' shows the results of Kenyon et al. (1993), and the third row marked 'CBM' shows the results of Chandler et al. (1998).

angle. But they did not estimate a property of the disk because they did not explicitly include it in their model though they implicitly considered the disk through a centrifugal radius. They also did not estimate the opening angle $\theta_{\rm bp}$. On the other hand, Chandler et al. estimated the circumstellar mass from the SED in the range $\nu < 10^{13}$Hz (region 1), whose fluxes depend on the circumstellar mass. They derived the luminosity of the source from integration of the emergent SED. They also did not derive the structures of the disk and the cavity because their simple model did not include these components.

There are four remarkable differences between our results and other two works. First, the luminosity L_* derived by our model is small compared with the other. The luminosity estimated by Chandler et al. is corresponding to the emergent luminosity $L_{\rm SED}$ accurately. We showed that, for a Class I object, emergent luminosity is not equivalent to the central luminosity (see section 4.3.1), so their estimation is not valid. On the other hand, Kenyon et al. cannot reproduce the fluxes at these high frequency range, because they do not include the bipolar cavity. The cavity in the envelope needs to reproduce the fluxes in the range corresponding to the near-infrared wavelength ($\sim 10^{14}$Hz). As indicated by the existence of the near-infrared nebulosity, it is certain that there is a cavity in the envelope. Thus, the luminosity derived by Kenyon et al. seems to be incorrect. We showed from the spectral fitting that we can reproduce the relatively large emergent luminosity ($\sim 2.8 L_\odot$) using the small central luminosity ($1 L_\odot$) because of the anisotropy

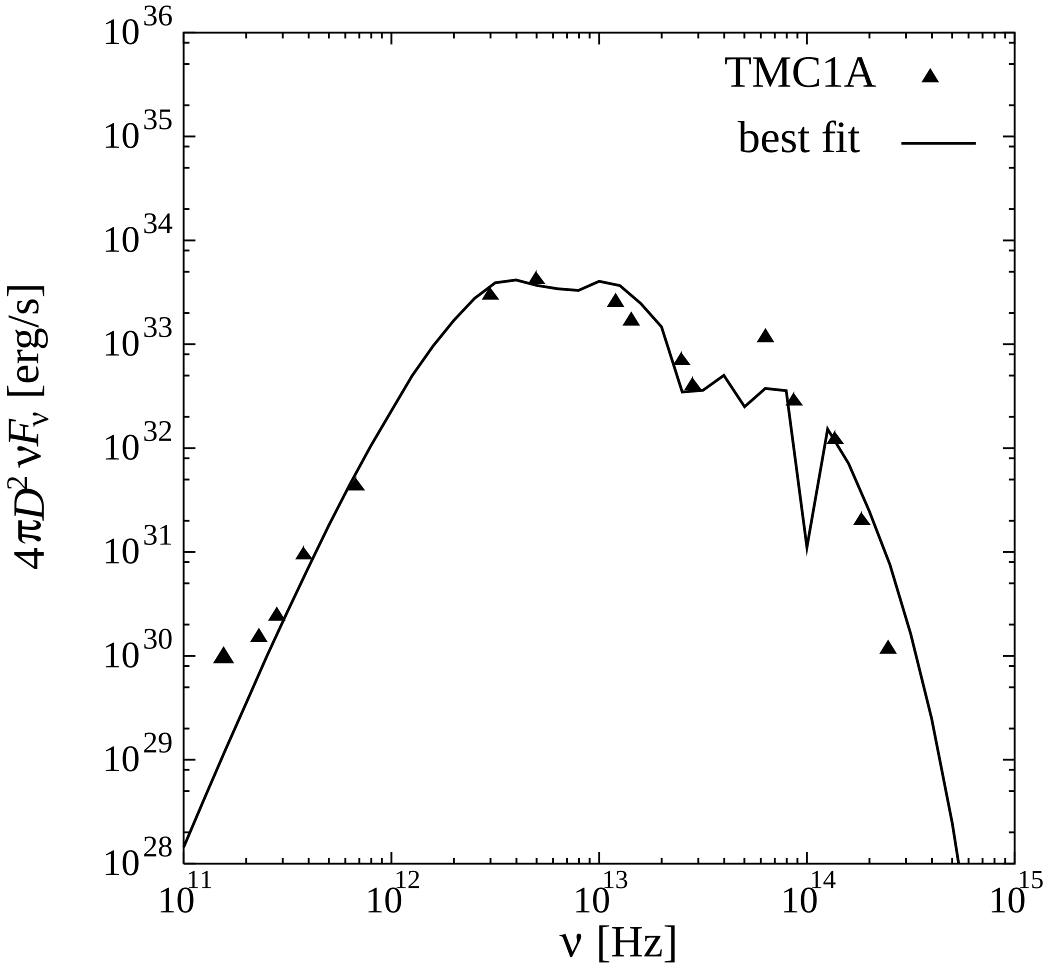

Figure 5.2: Best fitted SED of our protostar model for TMC1A (solid curve). The filled squares are data points same as Figure 5.1. Adopted parameters are $L_* = 1.0L_\odot$, $\rho_1 = 10^{-12.5}$ g cm^{-3}, $\Sigma_1 = 10000$ g cm^{-2}, $\theta_{\rm bp} = 20°$, and $i = 22°$.

of the density, which causes the anisotropy of the emergent flux. Second, the mass of the envelope, estimated by us is different from Chandler et al. by orders of magnitude. This result relates with the estimation of the luminosity of the central star. The luminosity L_* is equivalent with a total energy emitted from the system. Thus, L_* affects the SED over the whole frequency range (see Figure 4.4). Chandler et al. estimated the mass $M_{\rm env}$ assuming that the fluxes in sub-millimeter range is almost determined by the circumstellar mass. But, indeed, emergent fluxes are strongly dependent on the luminosity L_*, especially around the peak. Thus, it is necessary to estimate the circumstellar mass and the luminosity of the central star consistently with the observed flux in the whole frequency range since luminosity of the central star affects the whole structure of the emergent SED. Chandler et al. estimated the luminosity larger than the value estimated by us, and circumstellar mass to reproduce the flux at sub-millimeter range is small compared with our estimation. Third, the inclination angle i estimated from our model is different from that by Kenyon et al. Our result predicts relatively small inclination angle because the observed near-infrared flux cannot be reproduced as long as the system has a large inclination angle. On the other hand, Kenyon et al. failed to reproduce the near-infrared fluxes because of the absence of the cavity. From the viewpoint of the reproduction of the flux in the high frequency range, the small inclination is preferable for this object. Finally, we can separate the disk and the envelope from the spectral fitting of the SED. It is a remarkable result because direct estimation of the structure of the disk from the SED is very difficult. Note that the mass of the disk is relatively massive compared with the envelope. It indicates that a large fraction of the circumstellar matter is accreted in the central region.

5.2 VLA1623

VLA1623 is a prototype of Class 0 object proposed by André et al. (1993). This source is a compact radio source associated with the molecular outflow (e.g. Leous et al. 1991). Molecular outflow is observed by CO, H_2, and continuum emission at near-infrared wavelength. From the CO observation, outflow has an opening angle $10° - 15°$, and is viewed nearly edge-on ($i = 90°$) assuming a conical shape (André et al. 1990).

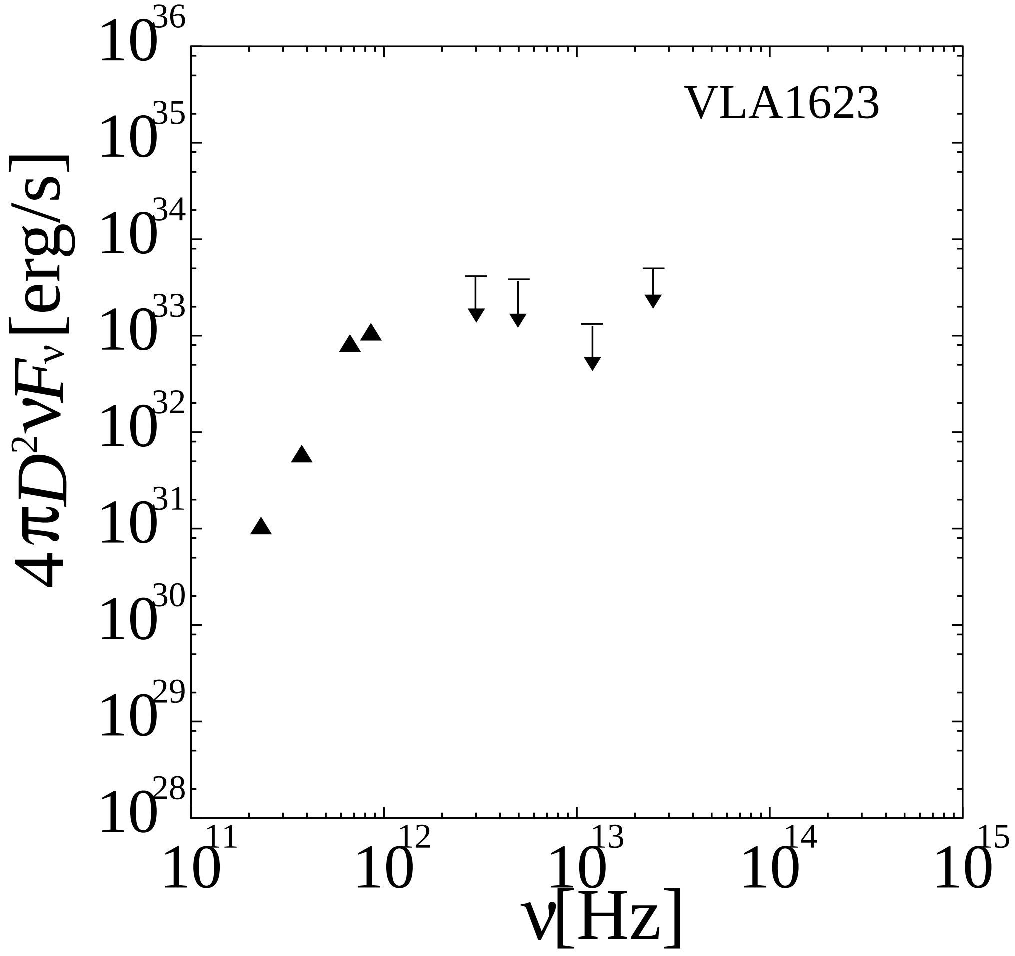

Figure 5.3: Emergent SED of a Class 0 object VLA1623. Plotted data were taken from André et al. (1993; filled square) and Ward-Thompson (1993; arrow). It is assumed that a distance to the object D is 160pc. The data taken from Ward-Thompson are upper limits.

Dynamical timescale of this outflow is estimated at $\sim 10^3$yr, that is comparable to the case of TMC1A (André et al. 1990). The outflow is also detected by the H_2 emission line and it has highly collimated structure (Dent et al. 1995). The imaging of the outflow using H_2 has revealed that there is brightest H_2 knot near the peak of the blueshifted CO emission (Davis & Eislöffel 1995). A line profile of HCO^+ line detected from this source indicates the existence of an infalling envelope (Gregersen et al. 1997). A circumstellar disk is considered to exist by the millimeter and sub-millimeter continuum mapping (Pudritz et al. 1996). Emergent SED of VLA1623 is shown in Figure 5.3. The flux data are taken from André et al. (1993) and Ward-Thompson (1993). André et al. (1993) observed this source using the sub-millimeter continuum emission and detected at 4 wavelength points. On the contrary, Ward-Thompson (1993) observed this by the infrared wavelength using IRAS, but did not detect at the IRAS band and only upper limits were obtained. It indicates that this source is surrounded by the massive envelope having very large optical depth. We constructed SED from these observational data assuming the distance to this source $D = 160$pc.

The emergent SED is very unknown, since there are only four data points in the sub-millimeter range. Thus, we do not use the method to infer the L_* and i, which is proposed in the section 4.4. The result of spectral fitting is shown in Figure 5.4. The physical properties obtained by spectral fitting using the present model agree very well with the results of André et al., except for the mass of the disk, which is only estimated by our model. The best fitted SED has slightly higher flux than the observation at wavelengths 850μm and 1.3mm. The fluxes in these wavelengths are almost determined by the circumstellar mass ($M_{\rm tot} = M_{\rm env} + M_{\rm disk}$). To fit these observational data, it is necessary to reduce either the mass of the disk or the envelope. But, reduction of the mass of the envelope leads to the increase of the scattered radiation from the cavity and the infrared fluxes are concerned for excess against upper limits by the IRAS, so we must reduce the mass of the disk. Thus, estimated mass of the disk should be regarded as an upper limit, and the mass of the envelope may be a lower limit.

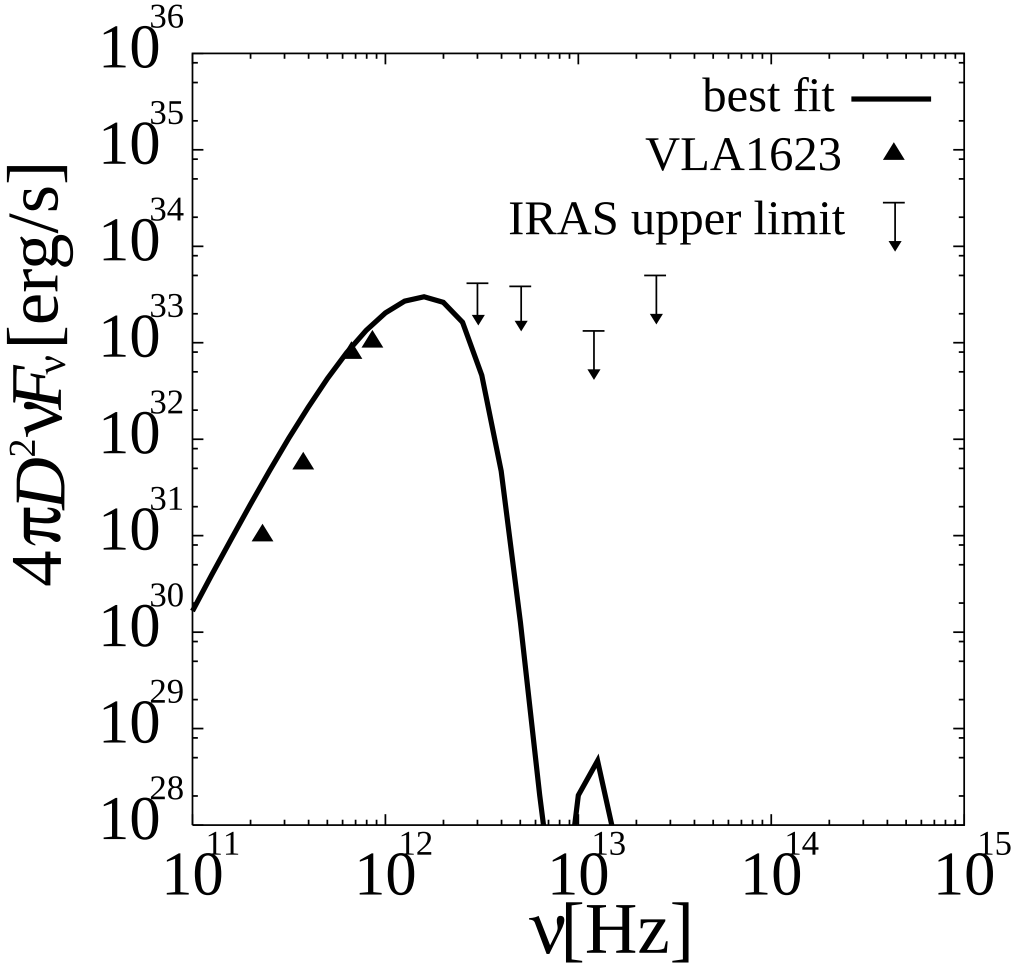

Figure 5.4: Best fitted SED of our protostar model for VLA1623 (solid curve). The filled squares are data points same as Figure 5.3. Adopted parameters are $L_* = 0.5L_\odot$, $\rho_1 = 10^{-12}$ g cm^{-3}, $\Sigma_1 = 2000$ g cm^{-2}, $\theta_{\rm bp} = 10^\circ$, and $i = 90^\circ$.

Physical Properties of VLA1623 Derived from SED

Ref.	L_* $[L_\odot]$	$M_{\rm env}$ $[M_\odot]$	$M_{\rm disk}$ $[M_\odot]$	$\theta_{\rm bp}$	i
This work	0.5	0.4	0.03	10°	90°
AWB etc.	$0.5 - 2.5$	0.6 ± 0.3	—	$10° - 15°$	$\sim 90°$

Table 5.2: Best fitted parameters for VLA1623. We omitted the value Σ_1 and ρ_1 for simplicity. The first row marked 'This work' is best fitted parameters of our protostar model. The second row marked 'AWB etc.' shows the results of André et al. (1993) and André et al. (1990).

5.3 Evolutionary States Inferred from the Spectral Modeling

From tables 5.1 and 5.2, it is clearly indicated that TMC1A is older than VLA1623 when we assume that these objects correspond to the pre-main-sequence stars having the similar final mass, because VLA1623 has a mass of the envelope roughly 4 times larger than that of TMC1A. The small mass of the disk also indicates that VLA1623 is younger than TMC1A. These results are consistent with the fact that VLA1623 belongs to Class 0, while TMC1A is classified to Class I. The bolometric luminosity of TMC1A is more luminous than VLA1623, although a mass accretion rate of VLA1623 appears to exceed that of TMC1A. This fact suggests that the mass of the central star M_*, which determines the gravitational potential around the central star, is small in the case of VLA1623 than that of TMC1A. This suggestion is also consistent with the youthfulness of VLA1623.

However, the dynamical timescales of the outflows are estimated at the same order, $\sim 10^3$yr for both objects. This estimation seems to be inconsistent with the mass estimation by our spectral fitting, because the outflow is driven either by a collapse of the envelope (Tomisaka 1998) or an accretion disk (e.g. Kudoh et al. 2002). In any case, it is expected from our spectral fitting that TMC1A has longer timescale than VLA1623. It may suggest a variability of the outflow activity.

We cannot directly estimate the effective temperature of the central star, corresponding to the horizontal axis of the H-R diagram. But, we can estimate the bolometric luminosity L_{bol} and the bolometric temperature T_{bol} from the spectral modeling of the sources TMC1A and VLA1623. Thus, we discuss the evolutionary state of these objects by using the BLT diagram. The bolometric luminosity is the luminosity of the central star L_* itself. The bolometric temperature T_{bol} is calculated from the equation (1.4) and the best fitted SED for each objects. For TMC1A, bolometric luminosity is $L_{\mathrm{bol}} = L_* = 1.0 L_\odot$, and bolometric temperature is estimated $T_{\mathrm{bol}} \sim 130\mathrm{K}$. These values for VLA1623 are $L_{\mathrm{bol}} = 0.5 L_\odot$ and $T_{\mathrm{bol}} \sim 19\mathrm{K}$, respectively. We plotted these two objects onto the evolutionary track in the BLT diagram (Myers et al. 1998; Figure 5.5). TMC1A is located in the Class I region, while VLA1623 is located in the Class 0 region, that are consistent with their observational classification. TMC1A is located on the evolutionary track near the mass $0.3 M_\odot$ and the age between 0.5Myr and 1Myr. This age is slightly older than the typical lifetime of Class I objects and extremely older than the dynamical timescale of the outflow. VLA1623 is located in a slightly massive ($\sim 0.5 M_\odot$) and younger (< 0.5Myr) region. As a result, TMC1A is interpreted to be in an intermediate phase of the Class I stage, since its envelope still has a mass comparable to the final mass, and it is expected that this object finally grows to the mass $\sim 0.3 M_\odot$ when it reaches the zero-age-main-sequence. On the other hand, VLA1623 can be regarded as an object in a very early phase of the Class 0 stage for final mass $0.5 M_\odot$, because of its massive envelope compared with final mass.

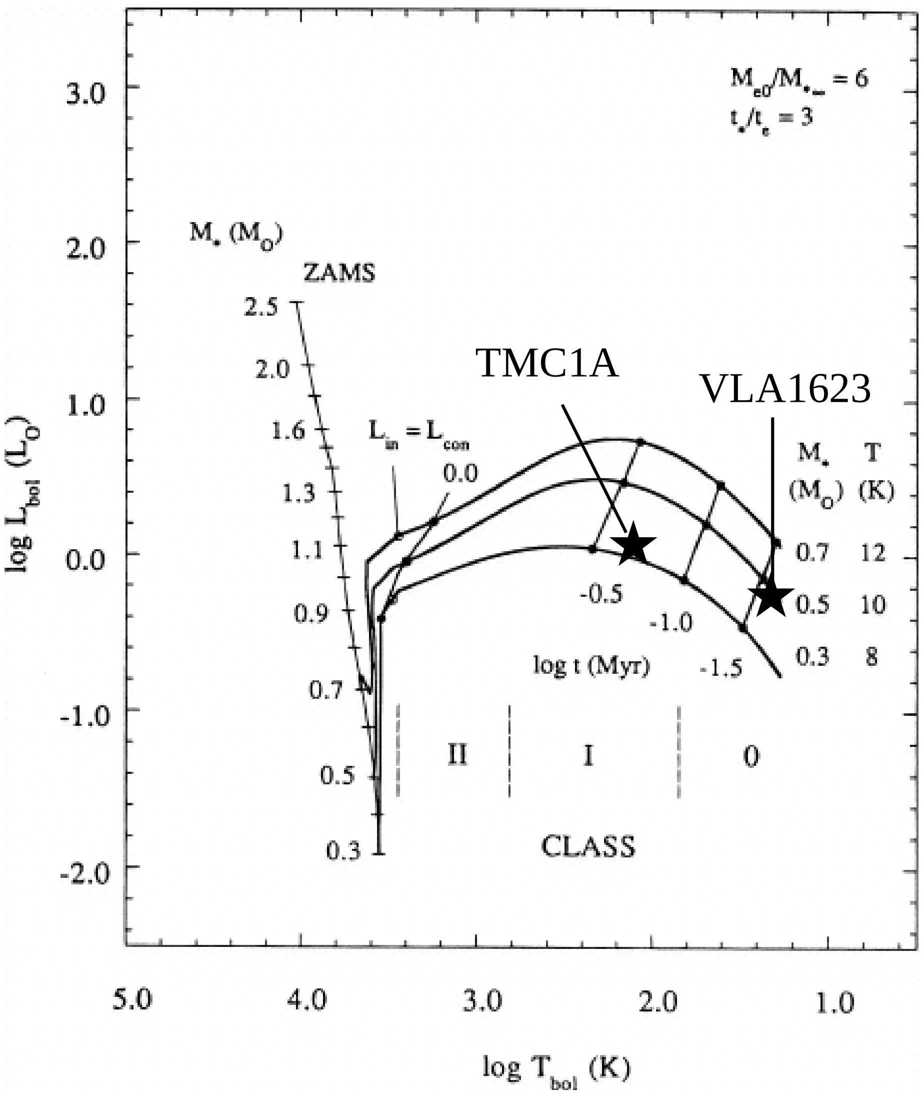

Figure 5.5: The bolometric luminosity-temperature diagram for low mass pre-main-sequence stars. The stars indicate the loci of TMC1A and VLA1623 from the results of our spectral fitting. The curve labeled by the mass and temperature is the evolutionary track of the stars given by the labeled initial condition. The vertical line at the left of the evolutionary track is the zero-age-main-sequence. This figure is created from the figure 9 in Myers et al. (1998) and our results.

Chapter 6

Conclusions

We constructed the two-dimensional radiative equilibrium protostar model. Our model determines the temperature distribution in the circumstellar matters consistently with the radiation field due to the central star. Emergent SED obtained by the present model reproduced well the observed feature of the Class I SED. We showed the importance of the accurate treatment of the radiative equilibrium comparing with the model approximately treating the radiative transfer. We investigated the dependence of the emergent SEDs on the physical parameters of the model, and clarified the dependence in detail. From the dependence of each parameter, we established the standard procedure of the spectral modeling. Finally, we applied the present method to the observed Class I and Class 0 SEDs.

The conclusions of this work are summarized as follows.

1. The calculated temperature distributions with the full- and semi- two dimensional calculations are different each other, especially in the disk, outflow, and the shaded region which is behind the disk with respect to the central star. The emergent SEDs are also different mainly due to the distinction of the temperature distribution and the radiation field of the diffuse component.

2. The procedure to infer the structure of the protostar is as follows: first, we restrict the opening angle of the outflow cavity θ_{bp} using the observation of the outflow associated with the target source. Second, we infer the inclination angle by using the indicator f_{L}, which is the ratio of the emergent luminosity L_{SED} and the peak

flux $(\nu L\nu)_{\rm max}$. Third, we infer the luminosity of the central star L_* from the value of $(\nu L\nu)_{\rm max}$ corrected by the inclination angle. Fourth, we infer the total mass of the envelope and the disk $M_{\rm tot}$ from the flux in a frequency range where the system is optically thin. Finally, we infer the ratio of the mass of the envelope and the disk, and determine the mass of each component, i.e. $M_{\rm env}$ and $M_{\rm disk}$, from the flux in near-infrared to optical wavelengths.

3. Applying our new method, we have estimated that the Class I object TMC1A (IRAS04365+2535) has the bolometric luminosity $L_{\rm bol} = 1L_\odot$, the mass of the envelope $M_{\rm env} = 0.13M_\odot$, the mass of the disk $M_{\rm disk} = 0.1M_\odot$, (half-)opening angle of the cavity $\theta_{\rm bp} = 20^\circ$, and the inclination angle $i = 22^\circ$. On the other hand, the Class 0 object VLA1623 has the bolometric luminosity $L_{\rm bol} = 0.5L_\odot$, the mass of the envelope $M_{\rm env} = 0.4M_\odot$, the mass of the disk $M_{\rm disk} = 0.03M_\odot$, (half-)opening angle of the cavity $\theta_{\rm bp} = 10^\circ$, and the inclination angle $i = 90^\circ$. We first estimated the mass of the disk for each object only from the emergent SED. These objects have a bolometric temperature $T_{\rm bol} \sim 130$K for TMC1A and ~ 19K for VLA1623. The plot on the BLT diagram is consistent with the observational classification for each object. From the locus of the BLT diagram, we can estimate the evolutionary state for TMC1A and VLA1623. As a result, TMC1A is in an intermediate phase of protostar stage for low-mass $(0.3M_\odot)$ pre-main-sequence star, and VLA1623 is in a very early phase of the protostar stage for low-mass ($0.5M_\odot$, slightly massive than TMC1A) pre-main-sequence star.

Acknowledgments

I would like to thank M. Umemura, T. Nakamoto, and N.Kikuchi for valuable discussion, useful comments, and providing a simulation code. I am also grateful to the members of astrophysics group in University of Tsukuba. I am very thankful to S. Nagakura for kindhearted encouragement. The numerical simulations related to this work were carried out at Center for Computational Physics, University of Tsukuba.

Bibliography

[1] Adams, F. C., Lada, C. J., & Shu, F. H. 1987a, ApJ, 213, 788

[2] ———. 1988, ApJ, 326, 865

[3] André, P., Martín-Pintado, J., & Montmerle, T. 1990, A&A, 236, 180

[4] André, P, Motte, F., & Bacmann, A. 1999, ApJ, 513, L57

[5] André, P., Ward-Thompson, D., & Barsony, M. 1993, ApJ, 406, 122

[6] ———. 2000, in Protostars and Planets IV, eds. Mannings, V., Boss, A. P., Russell, S. S., (Tucson: University of Arizona Press), p. 59

[7] Anglada, G., Rodríguez, L. F., Estalella, J., & Torrelles, J. M. 1992, ApJ, 395, 494

[8] Appenzeller, I. & Tscharnuter, W. 1975, A&A, 40, 397

[9] Bachiller, R., André, P., & Cabrit, S. 1991a, A&A, 241, L43

[10] Bachiller, R., Guilloteau, S., Dutrey, A., Planesas, P., & Martín-Pintado, J. 1995, A&A, 299, 857

[11] Beichman, C. A., Myers, P. C., Emerson, J. P., Harris, S., Mathieu, R., Benson, P. J., & Jennings, R. E. 1986, ApJ, 307, 337

[12] Benson, P. J. & Myers, P. C. 1989, ApJ, 71, 89

[13] Bontemps, S., André, P., Terebey, S., & Cabrit, S. 1996a, A&A, 311, 858

[14] Bontemps, S., Ward-Thompson, D., & André, P. 1996b, A&A, 314, 477

[15] Boss, A. P. & Myhill, E. 1992, ApJS, 83, 311

[16] Cabrit, S. & Bertout, C. 1986, ApJ, 307, 313

[17] Calvet, N., Hartmann, L., Kenyon, S. J., & Whitney, B. 1994, ApJ, 434, 330

[18] Chandler, C. J., Barsony, M., & Moore, T. J. T. 1998, MNRAS, 299, 789

[19] Chandler, C. J. & Richer, J. S. 2000, ApJ, 530, 851

[20] Chandler, C. J. & Sargent, A. I. 1993, ApJ, 414, L29

[21] Chandler, C. J., Terebey, S., Barsony, M., Moore, T. J. T., & Gautier, T. N. 1996, ApJ, 471, 308

[22] Chen, H., Myers, P. C., Ladd, E. F., & Wood, D. O. S. 1995, ApJ 445, 377

[23] Chiang, E. I. & Goldreich, P. 1997, ApJ, 490, 368

[24] ———. 1999, ApJ, 519, 279

[25] Chini, R., Reipurth, B., Sievers, A., Ward-Thompson, D., Haslam, C. G. T., Kreysa, E., & Lemke, R. 1997a, A&A 325, 542

[26] D'Alessio, P., Cantó, J., Calvet, N., & Lizano, S. 1998, ApJ, 500, 411

[27] Davis, C. J. & Eislöffel, J. 1995, A&A, 300, 851

[28] Dent, W. R. F., Matthews, H. E., & Walther, D. M. 1995, MNRAS, 277, 193

[29] Eiroa, C., Miranda, L. F., Anglada, G., Estalella, R., & Torrelles, J. M. 1994, A&A, 283, 973

[30] Furuya, R. S., Kitamura, Y., Saito, M., Kawabe, R., & Wootten, H. A. 1999, ApJ, 525, 821

[31] Furuya, R. S., Kitamura, Y., Wootten, H. A., Claussen, M. J., Saito, M., Marvel, K. B., & Kawabe, R. 2000, ApJ, 542, L135

[32] Gómez, J. F., Curiel, S., Torrelles, J. M., Rodríguez, L. F., Anglada, G., & Girart, J. M. 1994, ApJ, 436, 749

[33] Greaves, J. S., Holland, W. S., & Ward-Thompson, D. 1997, ApJ, 480, 255

[34] Gregersen, E. M., Evans II, N. J., Zhou, S., and Choi M. 1997, 484, 256

[35] Hayashi, C. 1961, PASJ, 13, 450

[36] Hayashi, C., Nakazawa, K., & Nakagawa, Y. 1985, in Protostars and Planets II (Tucson: Univ. of Arizona Press)

[37] Hirano, N., Kameya, O., Nakayama, M., & Takakubo, K. 1988 ApJ, 327, L69

[38] Hodapp, K.-W. & Ladd, E. F. 1995, ApJ 453, 715

[39] Hogerheijde, M. R. & Sandell, G. 2000, ApJ, 534, 880

[40] Imai, H., Iwata, T., & Miyoshi, M. 1999, PASJ, 51, 473

[41] Jayawardhana, R., Hartmann, L., & Calvet, N. 2001, ApJ, 548, 310

[42] Kenyon, S. J., Calvet, N. & Hartmann, L. 1993, ApJ, 414, 676

[43] Kenyon, S. J. & Hartmann, L. 1995, ApJS, 101, 117

[44] Kenyon, S. J., Hartmann, L., Strom, K. M., & Strom, S. E. 1990, AJ, 99, 869

[45] Kenyon, S. J., Whitney, B. A., Gomez, M., & Hartmann, L. 1993, ApJ, 414, 773

[46] Kikuchi, N., Nakamoto, T., & Ogochi, K. 2002, PASJ, 54, 589

[47] Kippenhahn, R. & Weigert, A. 1990, Stellar Structure and Evolution (Springer-Verlag, Astronomy and Astrophysics Library)

[48] Koyama, K., Hamaguchi, K., Ueno, S., Kobayashi, N., & Feigelson, E. 1996, PASJ, 48, L87

[49] Kudoh, T., Matsumoto, R., & Shibata, K. 1998, 508, 186

[50] ———. 2002, PASJ, 54, 267

[51] Lada, C. J. 1999 in The Origin of Stars and Planetary Systems, eds. Charles J. Lada and Nikolaos D. Kylafis (Kluwer Academic Publishers), pp. 143

[52] Lada, C. J. & Wilking, B. A. 1984, ApJ, 287, 610

[53] Ladd, E. F., Adams, F. C., Casey, S., Davidson, J. A., Fuller, G. A., Harper, D. A., Myers, P. C., & Padman, R. 1991a, ApJ, 366, 203

[54] ———. 1991b, ApJ, 382, 555

[55] Larson, R. B. 1969, MNRAS, 145, 271

[56] Leous, J. A., Feigelson, E. D., André, P., & Montmerle T. 1991, ApJ, 379, 683

[57] Loren, R. B., Sandqvist, A. & Wootten, A. 1983, ApJ, 270, 620

[58] Lynden-Bell, D. & Pringle, F. E. 1974, MNRAS, 168, 603

[59] Mardones, D., Myers, P. C., Tafalla, M. Wilner, D. J. Bachiller, R., & Garay G. 1997, ApJ, 489, 733

[60] Masunaga, H. & Inutsuka, S. 2000, ApJ, 531, 350

[61] Masunaga, H., Miyama, S. M., & Inutsuka, S. 1998, ApJ, 495, 346

[62] Matsumoto, T. & Hanawa, T. 1999, ApJ, 521, 659

[63] Men'shchikov, A. B. & Henning, T. 1997, A&A, 318, 879

[64] Miyake, K. & Nakagawa, Y. 1993, Icarus, 106, 20

[65] Motte, F. & André, P. 2001, A&A, 365, 440

[66] Myers, P. C., Adams, F. C., Chen, H., & Schaff, E. 1998, ApJ, 492, 703

[67] Myers, P. C. & Ladd, E. F. 1993, ApJ, 413, L47

[68] Nakazato, T., Nakamoto, T., & Umemura, M. 2003, ApJ, in press

[69] Ohashi, N., Hayashi, M., Ho, P. T. P., & Momose, M. 1997, ApJ, 475, 211

[70] Padgett, D. L., Brandner, W., Stapelfeldt, K. R., Strom, S. E., Terebey, S., & Koerner, D. 1999, ApJ, 117, 1490

[71] Palla, F. & Stahler, S. W. 1993, ApJ, 418, 414

[72] Pravdo, S. H., Rodríguez, L. F., Curiel, S., Cantó, J., Torrelles, J. M., Becker R. H., & Selgren, K. 1985, ApJ, 293, L35

[73] Pudritz, R. E., Wilson, C. D., Carlstrom, J. E., Lay, O. P., Hills, R. E., & Ward-Thompson, D. 1996, ApJ, 470, L123

[74] Saigo, K., Matsumoto, T., Hanawa, T. 2000, ApJ, 531, 971

[75] Saito, M., Kawabe, R., Kitamura, Y., & Sunada, K. 2001, ApJ, 547, 840

[76] Sandell, G., Avery, L. W., Coulson, I., Dent, W. R. F., Friberg, P., Gear, W. P. K., Greaves, J., Holland, W., Jenness, T., Jewell, P., Matthews, H. E., Moriarty-Schieven, G., Prestage, R., Robson, E. I., Stevens, J., Tilanus, R. P. J., & Watt, G. D. 1999, ApJ, 519, 236

[77] Shu, F. H. 1977, ApJ, 214, 488

[78] Snell R. L. & Bally, J. 1986, ApJ 303, 683

[79] Stone, J. M., Mihalas, D. & Norman, M. L. 1992, ApJS, 80, 819

[80] Tamura, M., Gatley, I., Waller, W., & Werner, M. W. 1991, ApJ, 374, L25

[81] Terebey, S. Padgett, D. L. 1997, IAU Symp. 182, eds. B. Reipurth and C. Bertout (Dordrecht: Kluwer), pp. 507

[82] Terebey, S., Shu, F. H., & Cassen, P. 1984, ApJ, 286, 529

[83] Terebey, S., Vogel, S. N., & Myers, P. C. 1989, ApJ, 340, 472

[84] Tomisaka, K. 1998, ApJ, 502, L163

[85] Tsuboi, Y., Koyama, K., Hamaguchi, K., Tatematsu, K., Sekimoto, Y., Bally, J., & Reipurth B. 2001, ApJ, 554, 734

[86] Tsujimoto, M., Koyama, K., Tsuboi, Y., Goto, M., & Kobayashi, N. 2002, ApJ, 566, 974

[87] Uchida, Y. & Shibata, K. 1985, PASJ, 37, 515

[88] Visser, A. E., Richer, J. S., & Chandler, C. J. 2002, AJ, 124, 2756

[89] Walker, C. K., Lada, C. J., Young, E. T., Moloney, P. R., & Wilking, B. A. 1986, 309, L47

[90] Walker, C. K., Narayanan, G., & Boss, A. P. 1994, 431, 767

[91] Ward-Thompson, D. 1993, MNRAS, 265, 493

[92] Ward-Thompson, D., Buckley, H. D., Greaves, J. S. Holland, W. S. & André, P. 1996, MNRAS, 281, L53

[93] Wolf-Chase, G. A., Barsony, M., Wootten, H. A., Ward-Thompson, D., Lowrance, P. J., Kastner, J. H., & McMullin, J. P. 1998, ApJ, 501, L193

[94] Zavagno, A., Molinari, S., Tommasi, E., Saraceno, P., & Griffin, M. 1997, A&A, 325, 685

[95] Zinnecker, H., Bastien, P., Arcoragi, J. P., Yorke, H. W. 1992, A&A, 265, 726